UNIVERSITÀ DEGLI STUDI DI PADOVA

FACOLTÀ DI INGEGNERIA

CORSO DI LAUREA SPECIALISTICA IN INGEGNERIA ELETTRONICA

TESI DI LAUREA

Characterization and reliability of blue and white GaN-based LEDs submitted to current and thermal stress

Relatore: Ch.mo Prof. Enrico Zanoni

Correlatore: Prof. Matteo Meneghini

Laureando: Paolo Bugno

DIPARTIMENTO DI INGEGNERIA DELL'INFORMAZIONE

Anno Accademico 2009/2010

Contents

Abstract

The aim of this thesis work is to analyze reliability of blue and white GaN-based commercial LEDs. Reliability is indeed one of the key factors for devices success in the market of lighting solutions.

Temperature and driving current are the main causes of degradation of LEDs. In order to understand the degradation mechanisms of these devices two types of stresses have been carried out, current and thermal stress and pure thermal stress, and electrical, optical and thermal measurements have been performed.

The results obtained at the end of this work show several types of degradation mechanisms which influence LEDs both electrical and optical properties.

Introduction

In 1879 Thomas Alva Edison invented the incandescent lamp. This invention has been a breakthrough in human progress since it permitted people not to be strictly tied up to sunrise and sunset. The success of this device is due to its simplicity and to the quality of the light produced, very similar to sunlight. Unfortunately, incandescent lamps have a very low efficiency, 95 % of the absorbed power is dissipated in heat, also their average lifetime is very short, just over 1000 hours.

Later technologies regard the fluorescent lamp. These lamps are capable of higher efficiencies (approximately of 25 %) and of a longer lifetime (approximately of 10000 hours) compared to incandescent lamps. Furthermore, their characteristics make their ratio quality/price more convenient. The main drawback of these lamps compared to incandescent lamps is that the white light they emit is perceived by the human eye as "colder".

In the last few years research on illumination devices has focused on semiconductor-based solid state devices, and particularly Light-Emitting Diodes (LEDs).

The year that marks the beginning of illumination through semiconductors is 1907, when H. J. Round noticed that a sample of silicon carbide emitted a weak yellow light when exposed to a voltage of 10 V. This first experience was completely random and only in 1950s research started with some knowledge. Research gave good results: in 1962 the first red LED was built in AsGaP by N. Holonyak from General Electric. This LED had a luminous efficiency of 0.1 lm/W. He had the idea to take a diode in GaAs and expand its bandgap with some phosphor to have emission in the visible range of the electromagnetic spectrum. Research continued on compound semiconduct-

ors of groups III-V and II-VI. Soon it had been possible to cover most of the visible spectrum, but only with indicator LEDs (for red and IR LEDs the material used was AlGaAs, for green LEDs the materials used were GaP and GaP:N). In the 1980s construction techniques improved, so it started to be possible to produce high efficiency LEDs. In 1995 S. Nakamura produced the first blue LED in InGaN/GaN. The following step has been to produce high efficiency LEDs emitting white light.

The main advantage of today LEDs is their high efficiency, which can be even very near to 100 %. Since the 21 % of the world's electrical energy is used for illumination, replacing even only half of the light sources with LEDs we would have a global saving of electricity of more than 10 %. That would involve substantial economic benefits, but also a significant reducing of the environmental pollution.

Research on LEDs is giving always better results, thus LEDs are considered the main investment in the lighting field for the future.

Besides their high efficiency LEDs have also got many other advantages such as:

- a minimum production of heat compared to traditional illumination devices
- an average lifetime of 100000 hours, which is 100 times longer than that one of an incandescent lamp, and 10 times longer than that one of a fluorescent lamp
- the capability to generate light of any color and with a very accentuated selectivity
- they are very small
- they are very strong and resistent

However LEDs have also disadvantages such as:

- the lack of compatibility of the lattice constants and the thermal coefficient of gallium nitride with those of the materials used to produce

substrates and charge confinement layers, which can lead to the generation of crystal defects

- a technology growth which is not yet refined and reliable
- gallium nitride grows unintentionally n-doped, the unintentional n-doping makes difficult to create p-doped layers
- the difficult realization of ohmic contacts
- the presence of the piezoelectric effect, which reduces the efficiency of the active zone
- the generation of deep levels in the energy gap that can reduce the efficiency of radiative recombination and vary the fixed charge distribution

Nowdays LEDs have got many applications, among which we can mention the following:

- large displays for stadiums, airports, stations and dynamic decorative displays
- traffic lights, emergency exits, emergency lights and brake and position lights on vehicles
- billboards
- illumination with white LEDs
- architectural decorations for buildings
- backlight of LCD TV

The aim of this thesis work is to analyze the reliability characteristics of four models of commercial LEDs manufactured by three protagonists of the lighting market, Cree, Philips Lumileds and Osram Opto Semiconductors. The commerical LEDs worked on are Cree XR-E blue, Cree XR-E white, Philips Lumileds Luxeon K2 and Osram Opto Semiconductors Golden Dragon Plus. In order to understand the degradation mechanisms of these

devices different current and thermal stresses and different pure thermal stresses have been carried out. The electrical and optical properties of analyzed devices during stress have been examined through the following measurements:

- current versus voltage (I-V)
- optical power versus current (L-I)
- electroluminescence (EL)
- thermal resistance (R_{th})

This thesis work is devided in the following chapters:

- Chapter 1 describes the semiconductor material gallium nitride. This is one of the most interesting and promising materials in the optoelectronic field. It is also the material on which LEDs analyzed in this work are based.
- Chapter 2 presents theory of light-emitting diodes. In this chapter recombination mechanisms, LED structures and LEDs optical properties are examined.
- Chapter 3 describes solid state lighting. It first talks about human perception of light, then describes in more detail white light sources, both based on LEDs and based on wavelength converters.
- Chapter 4 presents the characterization techinques that have been used in this work, instruments and measurement setups.
- Chapter 5 describes the results obtained at the end of the different stresses performed.

Chapter 1

Gallium nitride

Gallium nitride is a binary group III/group V direct bandgap semiconductor material. Since the growth and doping problems have been resolved it has become the most widely used semiconductor for optoelectronic devices. In optoelectronic devices, in fact the arrival of GaN has been necessary in order to develop blue and green light emitting diodes and Deep UltraViolet LEDs. Gallium nitride is a very hard and mechanically stable material and has a large heat capacity.

1.1 Gallium nitride chemical and physical properties

Gallium nitride, thanks to its chemical and physical properties, is, together with GaAs, one of the most attractive and used semiconductor materials for producing electronic and especially optoelectronics devices.

Gallium nitride can crystallize both in the wurtzite and the zincblend structure. As far as crystallography is concerned the two different structures present many analogies, but they are strongly different form the electrical and doping point of view. Wurtzite crystalline structure is characterized by a lattice which has an hexagonal structure with equal constants a and b. The c axis is orthogonal to the hexagonal plane. The lattice is in fact a sequence of gallium and nitride atom surfaces which are placed along c axis. Thus, the

wurtzite crystallographic structure is characterized by two hexagonal lattice structures compenetrated. Zincblend lattice is formed with nitride atoms which are placed in a cubic structure and bonded to a thetraedric structure formed by gallium atoms. Thus, the zincblend lattice is formed by two cubic lattice structures compenetrated.

The definition of the crystalline structure of GaN is given by three lattice constants (a, b, c) and three angles α, β and γ. Wurtzite has constants $a = b \neq c$, $\alpha = \beta = 90°$, $\gamma = 120°$, instead zincblend has constants $a = b = c$ and $\alpha = \beta = \gamma = 90°$ typical of a cubic structure. The two crystalline structures are shown in Figs. 1.1 and 1.2.

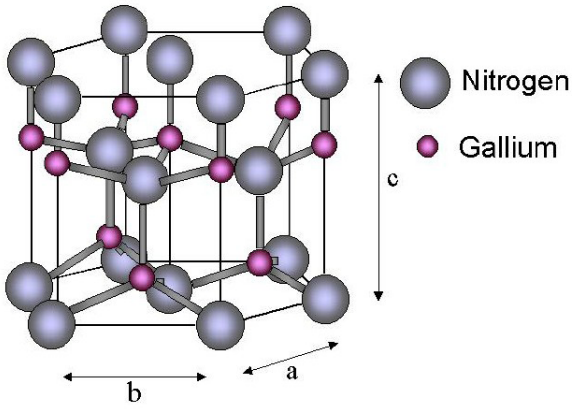

Figure 1.1: Wurzite crystalline structure

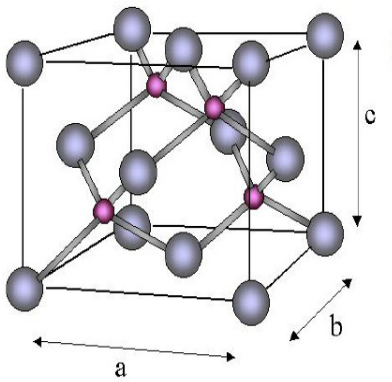

Figure 1.2: Zincoblend crystalline structure

The lattice constants of the crystal have a strong relation with the electrical properties of the semiconductor. For example smaller is the lattice structure, greater is the energy gap. This phenomenon coincides also with the relation between temperature and energy gap, in fact a higher temperature produces a widening of the crystal structure, and thus a lower energy gap. Fig. 1.3 presents differences between wurzite GaN, zincoblend GaN and other semiconductors.

Properties (300K)	Simbol	Ge	Si	GaAs	GaP	GaN
Lattice structure (D=Diamond, Z=Zinc blend, W=Wurtzite)		D	D	Z	Z	W Z
Gap (D=direct, I=indirect)		I	I	D	I	D
Lattice constant	$a_0 = b_0$[Å]	5.64	5.43	5.65	5.45	3.19 4.52
	c_0 [Å]					5.19 4.52
Band-gap Energy	$E_g[eV]$	0.66	1.12	1.42	2.26	3.44 3.3
Intrinsic carrier density	$n_i[cm^{-3}]$	2×10^{13}	1×10^{10}	2×10^{16}	1.6×10^{10}	1.9×10^{10}
Electron mobility	$\mu_n[cm^2/Vs]$	3900	1500	8500	110	1500
Hole mobility	$\mu_p[cm^2/Vs]$	1900	450	400	75	30
Electronic Diffusion constant	$D_n[cm^2/s]$	101	39	220	2.9	39
Hole Costante Diffusion constant	$D_p[cm^2/s]$	49	12	10	2	0.75
Electronic affinity	$\chi[V]$	4.0	4.05	4.07		4.1
Refraction index	n_{opt}	4.0	3.3	3.4		2.67 2.5
Breakdown field	$\varepsilon_1[\times10^5$ V/cm]	0.8	3	3.5		33
Thermal conductivity	$k[W(cm\ k)^{-1}]$	0.606	1.412	0.455	0.97	1.5

Figure 1.3: Semiconductor parameter comparison

Gallium nitride crystal has a light probability of dislocations and lattice defect formation due to the strong bonding energy between the GaN atoms. For this reason GaN is very stable and used for high power applications.

The use of GaN in the optoelectronic field is basically related to its elec-

tronic band structure, which has a direct energy gap. The electronic band structure of wurzite GaN is presented in Fig. 1.4.

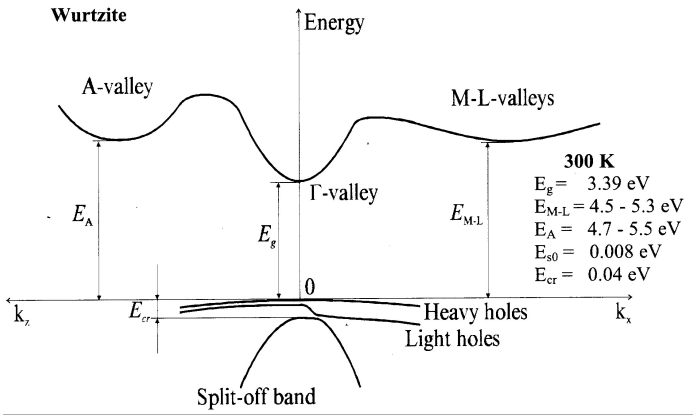

Figure 1.4: Wurzite GaN

Differently from other composite semiconductors, gallium nitride has a sensible degeneration of the valence band. This phenomenon is related to the high electric field due to the crystalline structure. Thus wurtzite GaN may be considered as an intrinsic deformation structure, and so, less influenceable by external deformation forces. In optoelectronic applications the most important transition is the fundamental one, from the maximum of the valence band to the minimum of the conduction band. The energy related to this transition is 3.504 eV, corresponding to a wavelength of 355 nm in void. The wide energy gap and good thermal stability of GaN is also advantageous for high-temperature (HT) and high power electronics.

Gallium nitride forms solid solutions with AlN and InN, making a wide range (1.9 - 6.2 eV) of energy gap possible. This ability to form alloys is essential for producing specific wavelengths for LEDs. Alloys are also very useful in creating heterojunctions with potential barriers into the device structures.

Heat dissipation in GaN-based devices is facilitated by GaN's high thermal conductivity compared to that one of silicon and gallium arsenide. Both n- and p-type conductivities are possible in GaN.

1.2 Brief history of GaN technology

The first growth of GaN is attributed to Johnson, who describes how to obtain gallium nitride with a chemical reaction involving gallium and ammonia:

$$2\,\mathrm{Ga} + 2\,\mathrm{NH_3} \longrightarrow 2\,\mathrm{GaN} + 3\,\mathrm{H_2} \quad . \tag{1.1}$$

Later on, in 1969, the first quite efficient epitaxial growth technique is settled up by Maruska and Tietjen. From metallic gallium and chloridric acid, they established a reaction between gallium and ammonia:

$$\mathrm{GaCl} + \mathrm{NH_3} \longrightarrow \mathrm{GaN} + \mathrm{HCl} + \mathrm{H_2} \quad . \tag{1.2}$$

This technique grants a high growing rate, so thick layers of GaN could be obtained with the advantage of a little lattice mismatch from the bulk. Unfortunately electrical characteristics of devices grown with Maruska and Tietjen techniques are very poor.

1.3 Substrates

Gallium nitride, unlike other semiconductors, needs a substrate to grow on. Gallium nitride devices are generally created with a thin GaN film deposited on a different substrate (a material which is not GaN); that is an heteroepitaxial thin film. As a consequence of heteroepitaxy, the quality of the GaN film is very dependent on the properties of the substrate. In order to grow a GaN crystal virtually free of dislocations and defects, the two materials must have lattice constants and thermal expansion coefficients as close as possible. Defects such as threading dislocations, inversion domains, and the unintentional incorporation of impurities into the epitaxial GaN layer resulting from heteroepitaxy are strongly dependent with the type of substrate used. Finding a substrate with these characteristics has been a real youth problem. There are priorly few materials that match the characteristics needed for producing good quality GaN films:

- Sapphire
- Silicon carbide
- Silicon
- Gallium nitride

1.3.1 Sapphire

Single crystal sapphire, i.e. single crystal dialuminum trioxide, Al_2O_3, was the original substrate used in Maruska and Tietjen's pioneering studies of GaN epitaxy by hydride vapour phase epitaxy (HVPE) in 1969, and it remains the most commonly employed substrate for GaN epitaxy.

The large lattice constant mismatch ($\sim$ 15 %) between sapphire (Al_2O_3) and GaN leads to high dislocation density (10^{10} cm^2) in the GaN epitaxial film. This high defect density in the GaN epitaxial film reduces the charge carrier mobility, the minority carrier lifetime, and decreases the thermal conductivity, all of which degrade performances of devices made of GaN. Sapphire's coefficient of thermal expansion is greater than GaN's one. This produces biaxial compressive stress in the GaN layer as it cools down from the deposition temperature. Fig. 1.5 shows GaN on sapphire.

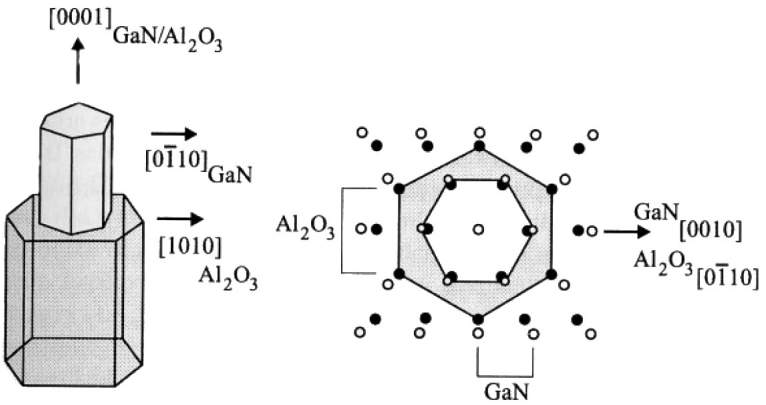

Figure 1.5: GaN on sapphire crystal structure and lattice mismatch

One of the reasons why sapphire has been so successful as a substrate for GaN epitaxy is simply that much more research has gone into developing

procedures for producing good quality GaN films on it compared to other substrates.

The large lattice constant mismatch between sapphire and GaN causes the GaN film to be completely relaxed (not strained) essentially from the beginning of growth. Consequently, the defect density at the sapphire substrate/GaN film interface is very high. Fig. 1.6 shows GaN defects and dislocations on sapphire substrate with buffer layer.

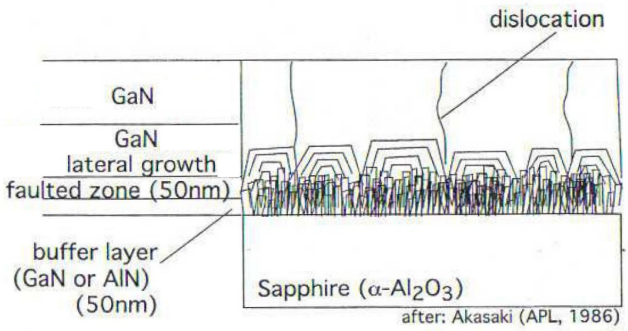

Figure 1.6: GaN defects and dislocations on sapphire substrate with buffer layer

The detrimental effect of the large lattice constant mismatch between sapphire and GaN must be improved by a sophisticated processing scheme.

1. the sapphire substrate surface is treated to remove contaminants, remnant polishing damages, and to produce a step and terrace surface structure

2. the sapphire substrate is nitridated to alter the wetting characteristics of the deposited layer

3. a thin buffer layer of either GaN or AlN (usually 10 - 100 nm thick) is deposited at a low temperature and annealed to produce a surface ready for the final epitaxial growth

The advantage of sapphire for optoelectronic devices consists in its transparency to visible light. Unfortunately sapphire is an electrical insulator, thus, all devices electrical contacts must be made on the front side of the devices,

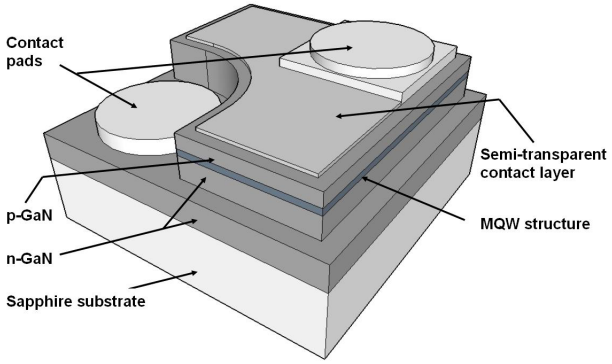

Figure 1.7: Example of a LED with a sapphire substrate

reducing the available area for devices and complicating devices fabrication. An example of a LED with a sapphire substrate is presented in Fig. 1.7.

The main characteristic is that both contacts have to be placed on the same surface, obviously reducing the emitted light flux.

This drawback can be minimized with flip-chip mounting, a particular technique consisting in mounting the device reversed with light flowing out from the substrate. The processing of a flip chip mounting is similar to conventional IC fabrication with the addition of a few steps. Near the end of the process, the attachment pads are "metalized" to make them more suitable for being soldered onto. A small dot of solder is then deposited on each of the pads. The chips are then cut out of the wafer as normal. No additional processing is required, and there is no mechanical carrier at all. To attach the flip chip into a circuit, it is inverted to bring the solder dots down onto connectors on the underlying electronics or circuit board. The solder is then re-melted to produce an electrical connection, typically using an ultrasonic process.

1.3.2 Silicon carbide

Single crystal silicon carbide (6H-SiC) is another substrate available for GaN epitaxy. The two materials have a reduced lattice constant mismatch, about 3.5 %, so due to this reduced mismatch, a good quality GaN film can be

grown on a SiC substrate. Consequently, the defect density at the SiC substrate/GaN film interface is lower than one at the sapphire substrate/GaN film. Conductive SiC substrates are available, making electrical contacts to the backside of the SiC substrate possible, therefore simplifying the device structure compared to sapphire substrates.

However, SiC does have its disadvantages. Gallium nitride epitaxy directly on SiC is problematic, due to poor wetting between these materials. This can be remedied by using an AlN or $Al_xGa_{1-x}N$ buffer layer, but such layers increase the resistance between the SiC substrate and the GaN film. Even though the lattice constant mismatch between SiC and GaN is smaller than that one between sapphire and GaN, it is still sufficiently large to cause a large density of defects to form in the GaN layer. Preparing smooth silicon carbide surfaces is difficult, thus, its surface roughness is an order of magnitude (1 nm RMS) higher than that one of sapphire (0.1 nm RMS). This roughness and also remnant subsurface polishing damages are sources of defects in the GaN epitaxial layer. The dislocation density in SiC goes from 103 to 104 cm^2, and these defects may propagate into the GaN epitaxial layer and degrade devices performances. Silicon carbide's thermal expansion coefficient is less than that one of AlN or GaN, thus, the epitaxial grown films are typically under biaxial tension at room temperature. Last, the cost of silicon carbide substrates is high, and currently single crystal SiC is produced by relatively few manufacturers.

Fig. 1.8 shows some physical properties of sapphire and silicon carbide.

1.3.3 Silicon

Silicon (111) with an AlN buffer layer can be another substrate for GaN epitaxy. Silicon's chemical and physical properties, high quality, and low cost make it indeed a very attractive substrate for GaN films. The crystal perfection of silicon is better than any other substrate material used for GaN epitaxy and its surfaces can be made extremely smooth. Silicon wafers are very low in price and are available in very large size due to its mature development and large-scale production. Silicon has also good thermal stability

Parameters	Sapphire (Al_2O_3)	Silicon Carbide (6H-SiC)
Symmetry	Hexagonal	Hexagonal
"'a"' lattice constant	4.758 Å	3.08 Å
"'c"' lattice constant	12.99 Å	15.12 Å
Density	3.98 g/mm^3	3.21 g/mm^3
Melting Point	2050 °C	2850 °C
Specific heat (20 °C)	10.16 cal/g	0.16 cal/g
Thermal capacitance	16.32 cal/mol K	6.4 cal/mol K
Thermal conductivity	0.412 W/cm K	4.9 W/cm K
"'a"' Thermal expansion coefficient	7.5×10^{-6} K^{-1}	4.68×10^{-6} K^{-1}
"'c"' Thermal expansion coefficient	8.5×10^{-6} K^{-1}	4.2×10^{-6} K^{-1}

Figure 1.8: Physical properties of sapphire and silicon carbide

under GaN epitaxial growth conditions.

However, the quality of GaN epitaxial layers on silicon is much poorer than that one on sapphire or silicon carbide, due to the large lattice constant and thermal expansion coefficient mismatch, and the tendency of silicon to form an amorphous silicon nitride layer when exposed to reactive nitrogen sources. Gallium nitride and AlN grown on Si (111) are highly defective and not radiative carrier recombination channels reduce the luminescence efficiency of many optoelectronic devices. For these reason silicon is not used as a substrate for GaN epitaxy.

1.3.4 Gallium nitride

The best substrate for GaN epitaxy is of course gallium nitride itself. The use of GaN as the substrate for GaN epitaxy, that is homoepitaxy, eliminates all the problem of heteroepitaxy, but only in the last few years it has been possible to grow epitaxial GaN on a GaN substrate. Homoepitaxy offers better control compared to heteroepitaxy over the crystal polarity and strained layer thickness. Gallium nitride homoepitaxy of smooth films does not require nitridation or buffer layers, as required instead for GaN heteroepitaxy,

for example with sapphire and silicon carbide.

Although there are several techniques under development for producing single crystal GaN bulks including growth by vapour phase transport, growth from supercritical fluids, and growth from sodium fluxes, only high pressure growth from solutions and hydride vapour phase epitaxy have produced large area crystals. The production of a thick GaN bulk layer is generally obtained with HVPE (Hydrogen Vapour Phase Epitaxy) over a layer of sapphire, and then the GaN layer is removed and used for homoepitaxy. This kind of growth is quite fast and for a thick GaN layer the dislocation density at the surface is small. Up to this date GaN optoelectronic devices built on a GaN substrate are entering the market solving critical problems of efficiency, maximum output power and stability.

1.4 GaN growth

Fabrication of high-brightness LEDs involves the growth of multilayer semiconductor films over appropriate substrates. Then the wafers are diced, the chips are equipped with contacts, and the LEDs are encapsulated into transparent plastic domes or other types of packages. Development of heterostructure/epitaxy growth techniques has required many efforts by semiconductor physicists and materials engineers. These techniques must facilitate precise and reproducible control of the composition and thickness of the grown layers. Also, the growth methods used in mass production must be cost-efficient.

The main epitaxial GaN growth techniques are the following:

- HVPE (Hydrogen Vapour Phase Epitaxy)
- MBE (Molecular Beam Epitaxy)
- MOCVD (Metal-Organic Chemical Vapour Deposition)
- MEMOCVD (Migration Enhanced Metal-Organic Chemical Vapour Deposition)
- ELO (Epitaxial Lateral Overgrowth)

1.4.1 HVPE

This technique is based on the reaction between ammonia (NH_3) as a source of Nitrogen and vapour gallium Chloride (GaCl) as a gallium source to obtain gallium nitride. The reaction is performed in a Hydrogen or Nitrogen rich ambient:

$$GaCl(g) + NH_3(g) \longrightarrow GaN(s) + HCl(g) + H_2(g) \quad . \tag{1.3}$$

The HVPE growth rate is quite high (30 - 130 μm/h), but the GaN obtained with this technique has the drawback to be rich of dislocation and lattice defect. For this reason HVPE is now only used to build thick layers of GaN on sapphire, GaN layers used as a bulk substrate for GaN homoepitaxy.

1.4.2 MBE

This technique is an Ultra-High-Vacuum (UHV) technique based on a simple reaction and it has been used, since 1958, for nitride, II-VI compounds and silicon growth. MBE is performed at lower temperature than HVPE.

In the last few years, it has been possible to use N_2 as a source of Nitrogen by means of a plasma source (PMBE, Plasma-Assisted MBE). This could not be done in the past decades due to N_2 strong bonding energy so the source of N was ammonia (NH_3), but this had the strong drawback to be Hydrogen rich. Fig. 1.9 shows the structure of a PMBE reactor.

The reaction chamber conditions, a constant pressure of 10^{-10} torr, and a lower temperature than HVPE permit the use of volatile elements like indium and Magnesium. The gallium atoms are extracted with thermal evaporation from effusion cells connected to the main chamber and regulated with a shutter. During operation, RHEED (Reflection High Energy Electron Diffraction) is often used for monitoring the growth of the crystal layer. Controlling shutters in front of each effusion cell, allow precise control of the thickness of each layer, down to a single layer of atoms. Intricate layers of different materials may be fabricated this way allowing the building up of heterostructures and MQW structures.

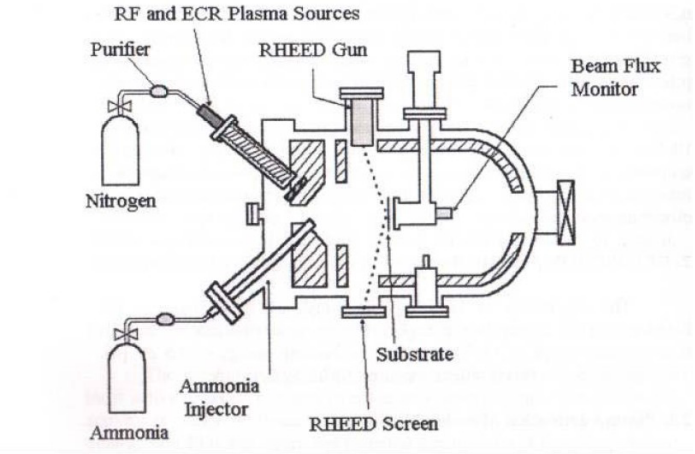

Figure 1.9: Structure of a PMBE reactor with RHEED gun

1.4.3 MOCVD

Metal-Organic Chemical Vapour Deposition is the most used process for producing epitaxial films for optoelectronic devices and has been first studied in 1990. Vapour phase group III elements and group V elements react in an MOCVD chamber at atmospheric pressure over a heated substrate. The technique consists of transport of vapour source materials, i.e. precursors, subsequent reaction of these source materials in the heated zone, and deposition of the final crystalline product on a substrate. Precursors of group III elements are metal-organic compounds, either trimethyl or triethyl based. The most extensively used precursors of group III elements are trimethylaluminium $Al(CH_3)_2$ (TMAl), trimethylgallium $Ga(CH_3)_2$ (TMGa), and trimethylindium $In(CH_3)_2$ (TMln) respectively for aluminium, indium and gallium growth. Precursors of group V elements are the hydrides phosphine (PH_3) and ammonia (NH_3) respectively for phosphide and nitride growth. Typical dopant precursors are the metal-organic compounds diethylzinc (DEZn), dimethylzinc (DMZn), bis(cyclopentadienyl)magnesium (Cp_2Mg), and diethyltellurium (DETe), as well as hydrides: silane (SiH_4) and disilane (Si_2H_6). Although reactions involved in MOCVD contain intermediate stages which are not completely understood, by MOCVD high quality epitaxial layers are obtained. Fig. 1.10 shows the structure of a MOCVD

reactor.

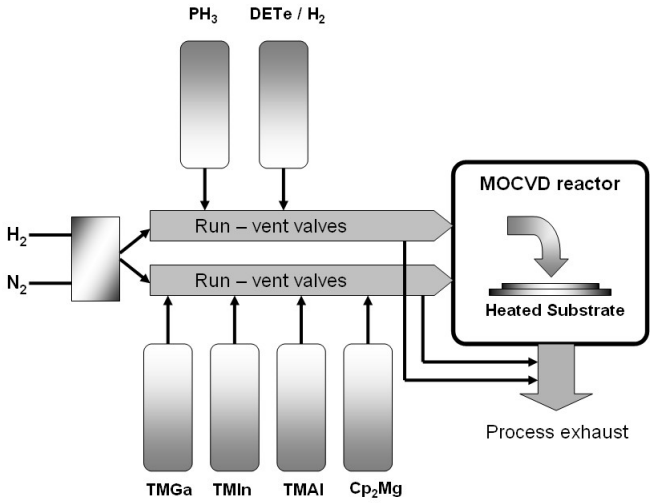

Figure 1.10: Structure and elements of a MOCVD reactor

At the beginning of the growth process the substrate is placed over a rotating graphite plate initially at 1150 ℃, then temperature is lowered to 450 ℃ allowing the building up of a low temporary buffer layer, then for the real GaN growth the temperature is raised to approximately 1075 ℃.

To increase the efficiency of the process, Nakamura in 1997 has developed a new system of MOCVD with the aim to increase the rate of metal-organic compounds that reach the heated substrate and perform a complete reaction. In Nakamura's system, also called two flow MOCVD, a gas flows parallel and another one flows perpendicular to the surface. The precursors are delivered by the horizontal flow through a quartz nozzle, flowing parallel to the substrate. The vertical flow transports inactive gases (N_2 + H_2) and is needed to bring the precursors into contact with the substrate. This configuration suppresses thermal convection currents on the substrate and cools the reactant gases just before they react. This lower temperature leads to more stable reactions and higher-quality grown films. A typical growth rate is 4 μm/h. Growth takes place at atmospheric or lower pressure. With TF-MOCVD it's possible to achieve a high speed growth with an acceptable dislocation density at the surface of the grown layer. With this technique it is possible to obtain GaN and several type of GaN alloys with enough accuracy to realize

layers with the desired energy gaps. A problem is still present with InGaN alloy with high indium levels: indium fragmentation occurs and thin layers present a heterogeneous structure. The high hydrogen level during reactions is the weak point of the process and several studies have accused hydrogen to be the principal responsible for GaN degradation phenomena

1.4.4 MEMOCVD

The technique Migration Enhanced Metal-Organic Chemical Vapour Deposition (MEMOCVD) has been developed by SETI (Sensor Electronic Technology Inc.). MEMOCVD is an epitaxial technique for growing AlN/GaN/InN epitaxial films and heterostructure layers using precursors controlled pulsed flow to achieve accurate control of the thickness of the grown films over large area substrates. It grants for example lower temperature than MOCVD. Trimethyl Aluminium (TMAl), Trimethyl Gallium (TMGa), Trimethyl Indium (TMIn) and ammonia (NH_3) are used as precursors of Al, Ga, In and N, respectively. MEMOCVD is an improved version of Pulsed Atomic Layer Epitaxy (PALE), which deposits quaternary $Al_xIn_yGa_{1-x-y}N$ layers by repeats of a unit cell grown by sequential (metal-organic) pulses of Al, In, Ga precursors and of NH_3 While in PALE the duration of each pulse is fixed, and the NH_3 pulse always follows each (metal-organic) pulse, the duration of precursor pulses in MEMOCVD are optimized, and pulses might overlap.

This technique bridges the gap between Molecular Beam Epitaxy (MBE) and Metal-Organic Chemical Vapour Deposition (MOCVD). MEMOCVD combines a fairly high growth rate with reduced growth temperature (by more than 150 °C compared to MOCVD) and improved quality for grown layers.

1.4.5 ELO

Epitaxial Lateral Overgrowth (ELO) is a technique consisting in growing GaN on a GaN bulk substrate generally obtained with HVPE on an initial sacrificial sapphire substrate. The sapphire substrate is then removed by means of laser-induced lift off (LLO), or thermal delamination due to thermal

strain of the interface. Both are damage-free separation techniques of GaN from sapphire. Overgrowth starts from a GaN seed and proceeds laterally generating a structure called wing. Several GaN seeds are present so that two wings starting from two adjacent seeds will meet in a coalescence boundary as presented in Fig. 1.11.

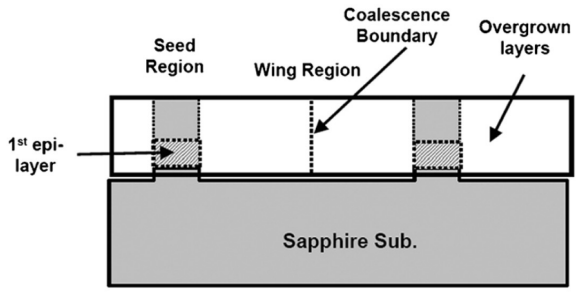

Figure 1.11: Schematic illustration of ELO GaN layers section

A technique of ELO GaN growth is now presented. A 2 μm-thick GaN layer is grown on a sapphire substrate, after which silicon dioxide (SiO_2) is deposited and patterned, forming stripe masks. The GaN region is then etched out by reactive ion etching (RIE) and the SiO_2 mask is subsequently removed by wet etching. Gallium nitride is then laterally overgrown using the rectangular GaN stripes as seed regions. A schematic illustration of the cross section of the ELO growth is shown in Fig. 1.11. Dislocations and defects are present both in the seed and the coalescence regions. Notice that most of the defects start from the GaN-sapphire interface and have a vertical propagation direction. Wing regions are instead clear of dislocations. Since dislocations act as non-radiative centres, reducing the dislocation density is also very effective in increasing efficiency of devices.

1.5 GaN alloys

In order to obtain heterostructures with a particular energy gap sequence it is necessary togrow GaN alloys. The properties of an alloy are different from the properties of the constituent materials. By following a law, called

Vegard's law, one can obtain desired properties for an alloy, like lattice constant and energy gap. In fact, Vegard's law is an approximate empirical rule, which holds that a linear relation exists, at constant temperature, between the properties of an alloy and the concentrations and the properties of the constituent materials. For example Vegard's law asserts that a ternary alloy property $P(A_xB_{1-x}C)$ may be obtained with a linear interpolation of the constituent materials concentration (x and y) and correspondent properties $P(AC)$ and $P(BC)$: $P(A_xB_{1-x}C) = xP(AC) + (1-x)P(BC)$. Following Vegard's law it is possible to create heterostructure with determined energy gap sequences and thus MQW structures.

Gallium nitride has a energy gap of 3.4 eV, thus to obtain alloys with a greater and lower energy gap at least two different binary compounds are needed. Indium Nitride (InN) and Aluminium Nitride (AlN) have a reduced lattice mismatch with GaN and are the main binary compounds used for GaN alloys. Fig. 1.12 shows a comparison between GaN, AlN and InN main parameters.

Proprietá	GaN	AlN	InN
Bandgap (300K)	$3.44eV$	$6.23eV$	$1.89eV$
Thermal coefficient dE_g/dT	$-6 \cdot 10^{-4}$eV/K	$-5.55 \cdot 10^{-4}$eV/K	$1.8 \cdot 10^{-4}$eV/K
"'a"' lattice constant (@ 300K)	0.3189 nm	0.3122 nm	0.3548 nm

Figure 1.12: Comparison between GaN, AlN and InN main parameters

1.5.1 Aluminium nitride

Aluminium Nitride (AlN) is a semiconductor with 6.2 eV energy gap, thus it can be used to generate Aluminium Gallium Nitride (AlGaN) with an energy gap bounded from 3.4 eV up to 6.2 eV. AlGaN is used in GaN devices to obtain confinement layers or to generate high energy photons. AlN is also compatible with GaN process and grants a good quality interface. AlN lattice constant mismatch with GaN is limited to 2.4 % and its fusion temperature is quite high, approximately 2200 °C. Hardness, high thermal conducibility and chemical reaction stability are the main properties of AlN compound.

1.5.2 Indium nitride

Indium Nitride (InN) has a low energy gap of 0.7 - 0.8 eV, thus it can be used to generate Indium Gallium Nitride (InGaN) with an energy gap bounded from x up to y eV. InGaN is used to realize blue and green LEDs. InN has the drawback of a low temperature dissociation, approximately (600 ℃) and, although indium nitride has a wurtzite crystal structure, the lattice constant mismatch with GaN is approximately 11 %, thus growing high quality InGaN layers presents many difficulties. Fortunately, presence of dislocations and defects on InGaN layers has lower impact on devices efficiency than in GaN layers. InGaN grows with a non intentional n doping, but with the use of magnesium it can be simply doped with acceptor atoms.

1.6 GaN doping

Gallium nitride is a promising candidate for fabricating visible and UV light emitting diodes (LEDs) and in general optoelectronic devices. In order to realize the production of these emitting devices, a method for obtaining high-quality GaN films and highly doped GaN films must be developed. For a long time it has been very difficult to obtain high-quality GaN films because of the lack of high-quality lattice-matched substrates. Also, for a long time it has been impossible to obtain a p-type GaN film due to the presence of high concentrations (typically above 10^{18} cm^{-3}) of donors in the undoped GaN film, generally attributed to N vacancies. So the key to obtain good p-type conductivity control is to grow high quality GaN films. Nakamura succeeded in this task for the first time using the TF - MOCVD technique with a buffer layer on sapphire substrate. With the use of this buffer layer technique, GaN p-n junction blue LEDs suitable for practical use were fabricated for the first time in 1991.

1.6.1 n-type doping

Silicon and Germanium are the commonly used n-type GaN dopants. In order to obtain from a LED high emission efficiency, the n-type layer requires

a high carrier concentration because many electrons must be injected into the p-type layer. Therefore, studies on n-type doping of GaN films are required in order to fabricate high-efficiency emission devices. The carrier concentration and Hall mobility of undoped GaN films grown with buffer layers are 4×10^{16} cm^{-3} and 600 $cm^2/(V\ s)$, respectively. Therefore, by using these high-quality GaN films, the doping efficiency of Si and Ge can be studied accurately in a wide doping range compared to studies that could be done when the carrier concentration of undoped GaN films was as high as 2×10^{19} cm^{-3}.

1.6.2 *p*-type doping

Since research on GaN began in the 1960s, the biggest unsolved problem has been the production of p-type GaN. For a long time it has been impossible to obtain p-type GaN films. Unavailability of p-type GaN films has prevented III-V nitrides from yielding visible light emitting devices, such as LEDs.

In 1989, it has been discovered how to obtain p-type GaN films using MOCVD, Mg doping and post low-energy electron-beam irradiation (LEEBI) treatment. After MOCVD growth, LEEBI (Low Energy Electron Beam Irradiation) treatment was performed on Mg-doped GaN films to obtain a low-resistivity p-type GaN film. The effect of the LEEBI treatment was argued to be Mg-displacement due to the energy transfer from the electron beam: when the undoped GaN film was doped with Mg the Mg atoms occupied sites different from Ga sites, where the Mg atoms would be acceptors. Under the LEEBI treatment, the Mg atoms moved to occupy exactly Ga sites. The hole concentration and lowest resistivity were 10^{17} cm^{-3} and 12 Ω cm, respectively. These values were still insufficient for fabricating high-power LEDs.

In 1992 Nakamura et al. found that p-type GaN with low resistivity could be obtained by thermal annealing. This thermal annealing technique representd a breakthrough in obtaining low resistivity p-type III-V nitride films because it is an easy, reliable, and mass-production technique. Thus, the thermal annealing technique is now commonly used to obtain MOCVD-grown low resistivity p-type GaN layers.

LEEBI treatment has the problem that only a very thin surface region of the Mg-doped GaN epitaxial wafer can have low resistivity. This is because the low-resistivity region of the Mg-doped GaN film depends on the penetration depth of the incident electrons in the LEEBI treatment. Consequently the LEEBI technique imposes severe restrictions on the fabrication of light emitting devices. Therefore a different method is necessary for flexible fabrication of optical devices. In Nakamura experiments, low-resistivity p-type GaN films were obtained by N_2-ambient or vacuum-ambient thermal annealing above 700 °C. Before thermal annealing, the resistivity of the Mg-doped GaN films was approximately 1×10^6 Ω cm. After thermal annealing at temperatures above 700 °C in an N_2 atmosphere, the resistivity, hole carrier concentration, and hole mobility became 2 Ω cm, 3×10^{17} cm^{-3}, and 10 $cm^2/(V\ s)$, respectively. The process was also reversible: if the same p-GaN sample was annealed in an NH_3 atmosphere, the resistivity went back to 10^6 Ω cm as it is shown in Figs. 1.13 and 1.14.

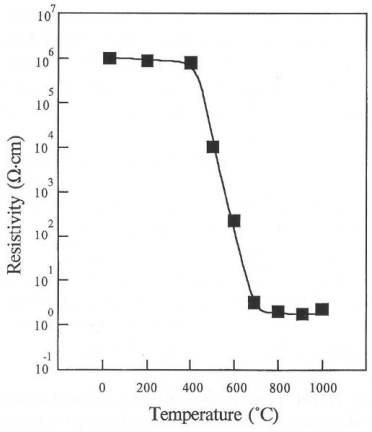

Figure 1.13: Resistivity versus annealing temperature in a Mg p-GaN sample

1.6.3 Effect of hydrogen in GaN

Due to the use of H_2 as a flow gas in MOCVD reaction, hydrogen is the most present impurity in GaN layers. H_2 itself is chemical inactive, but ionic forms of the element: H+ and H- are very reactive with Magnesium atoms.

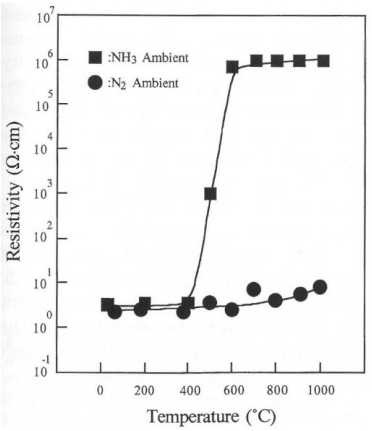

Figure 1.14: Resistivity versus annealing temperature in a Mg p-GaN sample

So the main effect of hydrogen is passivation (electrical deactivation) of Mg acceptors in p-GaN through the formation of neutral Mg-H complexes even at low temperatures $(25 \div 250)$°C. This reduces the acceptor percentage in GaN and raises resistivity. A thermal annealing in N_2 ambient at temperatures above 700 °C can remove hydrogen atoms from the neutral Mg-H complexes, thus lowering the p-type GaN films resistivity. Other treatments that activate magnesium at lower temperature but do not remove H from the material are LEEBI and minority carrier injection.

However even during the operating life of the final device, hydrogen affects the p-type semiconductor properties. As a matter of fact, the dopant behaviour results heavily influenced by the presence of this hydrogen which contaminates the semiconductor material.

1.7 Ohmic contacts on GaN

Achieving low resistance high stability ohmic contacts on GaN has been a challenge for scientists in the last few years, and is still an open discussion topic. The need of low resistance contacts is related, especially in high power LEDs, to narrowing heating effect and thus metal migration from contact to material. Building up an ohmic contact on high energy gap semiconductors like GaN is particularly challenging, thus the problem has been solved using

both tunnelling and Shottky ohmic contacts.

1.7.1 Ohmic contact on *n*-GaN

Fan et al. have developed a multilayer technology to create ohmic contacts on n-GaN with low resistance, 10^{-7} Ω cm. The n-GaN layer is GaN doped with silicon with carrier density equal to 10^{17} - 5×10^{17} cm^{-3}. A first Cl_2 etching is performed in order to remove surface oxides, then a multi metal layer Ti/Al/Ni/Au is deposited with thickness of 150/2200/400/500 $\dot{A}$ respectively. A following rapid thermal annealing at 900 ℃ for 30 s establishes a reaction between multilayer elements and generates TiAl AuNi, which give robustness and stability even at high temperature, avoiding electromigration. The ohmic contacts created are based on tunnelling transport. Fig. 1.15 shows the band diagram of a metal-semiconductor contact where tunneling takes place. Due

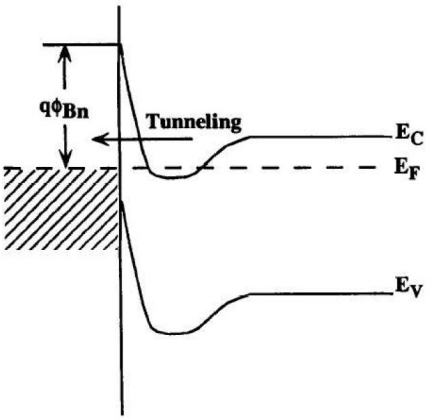

Figure 1.15: Band diagram of a metal-semiconductor contact where tunneling takes place

to the high efficiency of these contacts, most ohmic contacts on n-GaN are based on Titanium/Aluminium multilayer metallization.

1.7.2 Ohmic contact on *p*-GaN

Unfortunately, conventional produced p-GaN ohmic contacts have a high resistivity value of 10^{-2} Ω cm œ 10^{-4} Ω cm. The problem consists in the high

GaN energy gap and electron affinity ($\chi = 4.1$ eV), which require high work function (Φ_m) metals in order to achieve a low barrier $\Phi_B = \Phi_M - (E_G + \chi)$. Several expedient have been developed in order to build up low resistivity contacts: particularly the use of a moderate-high doping concentration of GaN and an accurate surface treatment to remove possible oxide formations. Most used metallization are multi metal layers of Nichel/Gold, Platinum and Tungsten.

1.8 GaN defect analysis

Main causes of reliability fault on solid state devices are creation of new defects or modification of existing defects in the crystal structure of the devices theirself. There are many types of defects with different effects on devices, the most relevant are

- Strain effects
- Point defects
- Stacking faults
- Dislocations

1.8.1 Strain Effects

When GaN is grown on a substrate with a different lattice constant, the difference between the two lattices establishes a strain on both crystal structures. For a particularly hard material like GaN, strain can induce cracks in the crystal structure. Fig. 1.16 shows an image of a GaN-sapphire interface.

1.8.2 Point defects

Point defects are defects which are not extended in space in any dimension. A point defect may be related to impurities trapped in the semiconductor or to vacancies in the crystal structure or to interstitial atoms.

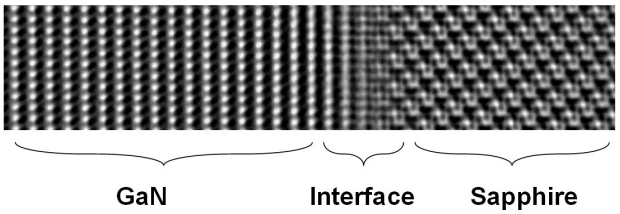

Figure 1.16: TEM image of a GaN-sapphire interface

Vacancies are sites which are usually occupied by an atom but which are unoccupied. If a neighbouring atom moves to occupy the vacant site, the vacancy may move in the opposite direction to the site which used to be occupied by the moving atom. Gallium nitride may be affected by Nitrogen vacancies (VN). Recent experimental results indicate that the N vacancies may play a role in passivating Mg, thus reducing doping in p-type GaN.

Interstitial atoms are atoms which occupy a site in the crystal structure where usually there is no atom. They are generally high energy configurations. However in some crystals like GaN small atoms such as hydrogen can occupy interstitial spaces without high energy. H is highly present in GaN interstitial spaces due to the growth procedure and can react with Mg.

Impurities In the case of an impurity, the atom is often incorporated in a regular atomic site in the crystal structure. Gallium nitride main impurities are:

- Oxygen: it acts like a donor, enhancing non-intentional n-doping
- Hydrogen: it is the most common and establishes MgH bonding passivating Magnesium, main source for H are precursor gases in MOCVD
- Carbon: it is present in MOCVD precursor gases and acts like an acceptor atom

1.8.3 Stacking faults

When the lattice is subjected to strain, a crystal plane interruption may occur, thus decreasing the mechanical tension of the crystal structure itself.

This phenomenon is called stacking fault. Gallium nitride is particularly affected by stacking faults, especially if grown on sapphire.

There are several kinds of stacking faults:

- those close to the GaN/substrate interface on the c plane that cause vertical propagating defects
- prismatic faults, generated by planar stacking faults on the c plane which propagate in [0001] direction
- stacking mismatch boundaries
- inversion domain boundaries

Considering the lower thermal coefficient mismatch, GaN grown on 6H-SiC has a reduced density of stacking faults. Local energy gap variation is the main effect of stacking faults.

1.8.4 Dislocations

The strain induced by the epitaxial layer can provoke a dislocation in order to reduce the mechanical tension. Fig. 1.17 shows an example of a dislocation caused by strain relaxation.

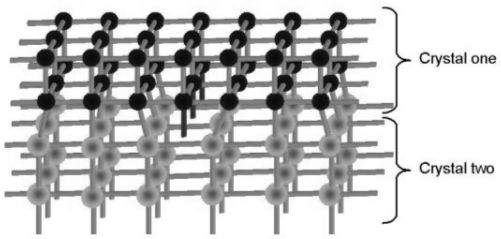

Figure 1.17: Example of a dislocation caused by strain relaxation

Many types of dislocations have been observed and are generally divided in: perfect, partial, V dislocations. V dislocations are those of main interest, they assume a flipped up pyramidal form with a size varying from 10 to 250 nm, and are common in MQW structures (multi layer nitride alloys interface). Dislocation mobility in GaN is quite lower than that in GaAs and

GaP due to the strong GaN bonding energy. In fact dislocation mobility is 10^{-10} - 10^{-16} times lower than in GaAs at room temperature and 10^{-19} in biasing conditions. Dislocations act like non-radiative recombination centres, therefore a high dislocation density has as consequence a lower efficiency of the devices and can provoke dark spots on the surface of the devices. Using epitaxial lateral overgrowth the problem of high dislocation density on GaN has been reduced by several orders of magnitude.

Chapter 2

Light-Emitting Diodes (LEDs)

2.1 Radiative and non-radiative recombination

In all semiconductors two opposite phenomena take place, electron-hole generation and electron-hole recombination. Electron-hole generation consists in the excitation of an electron from the valence band to the conduction band. Electron-hole recombination consists in the falling back of an electron from the conduction band to the valence band.

There are two basic electron-hole recombination mechanisms, radiative recombination and non-radiative recombination. In a radiative recombination event, one photon with energy equal to the energy gap of the semiconductor is emitted. In a non-radiative recombination event instead, no photon is emitted.

Two different types of non-radiative recombinations are possible, non-radiative recombination in the bulk and non-radiative recombination at surfaces.

We now summarize the possible recombinations that can take place in a semiconductor.

- Radiative recombination
- Non-radiative recombination in the bulk

- Non-radiative recombination at surfaces

In light-emitting devices, radiative recombination is clearly the preferred process. However, non-radiative recombination can, under practical conditions, never be reduced to zero. Thus, there is competition between radiative and non-radiative recombination.

2.1.1 Radiative recombination

Any undoped or doped semiconductor has two types of free carriers, electrons and holes.

Under equilibrium conditions, i.e. without external stimuli such as light or current, the law of mass action says that the product of the electron and hole concentrations is, at a given temperature, a constant, i.e.

$$n_0 p_0 = n_i^2 = p_i^2 \tag{2.1}$$

where n_0 and p_0 are the equilibrium electron and hole concentrations and n_i is the intrinsic carrier concentration.

Excess carriers in semiconductors can be generated either by absorption of light or by an injection current. The total carrier concentration is then given by the sum of equilibrium and excess carrier concentrations, i.e.

$$n = n_0 + \Delta n \quad \text{and} \quad p = p_0 + \Delta p \tag{2.2}$$

where Δn and Δp are the excess electron and hole concentrations, respectively.

Now we consider recombination of carriers. The band diagram of a semiconductor with electrons and holes is shown in Fig. 2.1. We are interested in the rate at which the carrier concentration decreases and denote the carrier recombination rate per unit time per unit volume as R. Let us consider a free electron in the conduction band. The probability that the electron recombines with a hole is proportional to the hole concentration, that is, $R \propto p$. The number of recombination events will also be proportional to the concentration of electrons. Thus, the carrier recombination rate is proportional

to the product of electron and hole concentrations, that is, $R \propto np$. Using a proportionality constant, the recombination rate per unit time per unit volume can be written as

$$R = Bnp \quad . \tag{2.3}$$

The proportionality constant B is called the bimolecular recombination coefficient. It has typical values of 10^{-11} - 10^{-9} cm^3/s for direct gap III-V semiconductors.

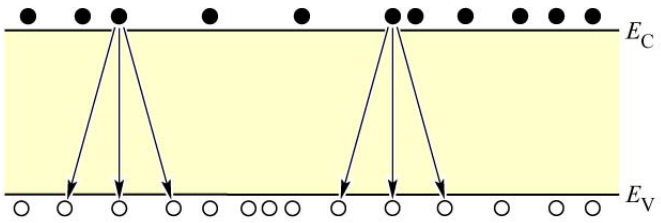

Figure 2.1: Radiative electron-hole recombination

Let us consider a semiconductor under non-equilibrium conditions. The equilibrium and excess electron and hole concentrations are n_0, p_0, Δn, and Δp, respectively. Since electrons and holes are generated and annihilated (by recombination) in pairs, the electron and hole excess concentrations Δn and Δp are equal,

$$\Delta n(t) = \Delta p(t) \quad . \tag{2.4}$$

Using the carrier recombination rate equation, the carrier recombination rate per unit time per unit volume is given by

$$R = Bnp = B[n_0 + \Delta n(t)][p_0 + \Delta p(t)] \quad . \tag{2.5}$$

Radiative recombination for low-level excitation

For the case of low-level excitation, the excess carrier concentration Δn and Δp with $\Delta n = \Delta p$ is much smaller than the majority carrier concentration, i.e. $\Delta n << (n_0 + p_0)$ and $\Delta p << (n_0 + p_0)$. Using $\Delta n(t) = \Delta p(t)$ one obtains from Eq. 2.5

$$R = Bn_i^2 + B(n_0 + p_0)\Delta n(t) = R_0 + R_{excess} \quad . \tag{2.6}$$

The first summand on the right-hand side of the equation can be identified as the equilibrium carrier recombination rate per unit time per unit volume (R_0) and the second term as the excess carrier recombination rate per unit time per unit volume (R_{excess}).

Radiative recombination for high-level excitation

For the case of high-level excitation, the excess carrier concentration Δn and Δp with $\Delta n = \Delta p$ is larger than the equilibrium carrier concentration, i.e. $\Delta n >> (n_0 + p_0)$ and $\Delta p >> (n_0 + p_0)$. Using $\Delta n(t) = \Delta p(t)$ one obtains from Eq. 2.5

$$R = Bn_i^2 + B[\Delta n(t)]^2 = Bp_i^2 + B[\Delta p(t)]^2 = R_0 + R_{excess} \quad . \tag{2.7}$$

The first summand on the right-hand side of the equation can be identified as the equilibrium carrier recombination rate per unit time per unit volume (R_0) and the second term as the excess carrier recombination rate per unit time per unit volume (R_{excess}).

2.1.2 Non-radiative recombination in the bulk

There are several physical mechanisms by which non-radiative recombination in the bulk can occur. The most important types of non-radiative recombination in the bulk are:

- Via deep levels recombination
- Auger recombination

Non-radiative recombination via deep level, non-radiative recombination via Auger process and radiative recombination are shown in Fig. 2.2.

Via deep levels recombination

Defects in the crystal structure are the most common cause for non-radiative recombination in the bulk. These defects include unwanted foreign atoms,

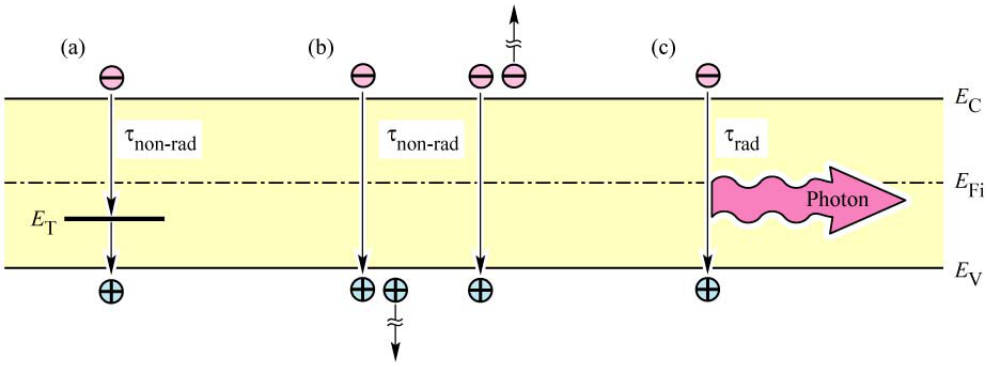

Figure 2.2: Band diagram illustrating recombination: (a) non-radiative via deep level, (b) non-radiative via Auger process and (c) radiative

native defects, dislocations and any complexes of defects, foreign atoms, or dislocations. It is quite common for such defects to form one or several energy levels within the forbidden energy gap of the semiconductor.

Energy levels within the energy gap of the semiconductor, called deep levels, are recombination centres; in particular if the energy level is close to the middle of the energy gap.

The recombination of free carriers via deep levels was first analyzed by Shockley, Read, and Hall. The non-radiative recombination rate through a deep level with energy E_T and concentration N_T is given by

$$R_{SRH} = \frac{p_0\Delta n + n_0\Delta p + \Delta n\Delta p}{(N_T v_p \sigma_p)^{-1}(n_0 + n_1 + \Delta n) + (N_T v_n \sigma_n)^{-1}(p_0 + p_1 + \Delta p)} \tag{2.8}$$

where $\Delta n = \Delta p$; v_n and v_p are the electron and hole thermal velocities, and σ_n and σ_p are the capture cross sections of the recombination centres. The quantities n_1 and p_1 are the electron and hole concentrations if the Fermi energy is located at the recombination centre energy. These quantities are given by

$$n_1 = n_i \exp\left(\frac{E_T - E_{Fi}}{kT}\right) \quad \text{and} \quad p_1 = p_i \exp\left(\frac{E_{Fi} - E_T}{kT}\right) \tag{2.9}$$

where E_{Fi} is the Fermi energy in the intrinsic semiconductor.

The lifetime of excess electrons can be deduced from the equation $R_{SRH} =$

$\Delta n/\tau$. Consequently, the lifetime is given by

$$\tau = \frac{(N_T v_p \sigma_p)^{-1}(n_0 + n_1 + \Delta n) + (N_T v_n \sigma_n)^{-1}(p_0 + p_1 + \Delta p)}{p_0 + n_0 + \Delta n} \quad . \tag{2.10}$$

We now assume that the semiconductor is p-type. Then holes are the majority carriers, i.e. $p_0 >> n_0$ and $p_0 >> p_1$. If we further assume a small deviation from equilibrium, i.e. $\Delta p = \Delta n << p_0$, then the excess carrier lifetime is given by

$$\tau = \tau_{n_0} = N_T v_n \sigma_n \quad . \tag{2.11}$$

Let us now assume that the semiconductor is n-type. Then electrons are the majority carriers i.e. $n_0 >> p_0$ and $n_0 >> n_1$. If we further assume a small deviation from equilibrium, i.e. $\Delta n = \Delta p << n_0$, then the excess carrier lifetime is given by

$$\tau = \tau_{p_0} = N_T v_p \sigma_p \quad . \tag{2.12}$$

The results show that the Shockley-Read-Hall recombination rate is limited by the rate of capture of minority carriers. This result suggests itself since the capture of majority carriers is a much more likely event than the capture of minority carriers. Eq. 2.10 can then be written as

$$\tau = \frac{\tau_{p_0}(n_0 + n_1 + \Delta n) + \tau_{n_0}(p_0 + p_1 + \Delta p)}{p_0 + n_0 + \Delta n} \quad . \tag{2.13}$$

As far as the temperature dependence of the Shockley-Read-Hall recombination is concerned it can be seen that as T increases the non-radiative recombination lifetime decreases. As a result, the radiative recombination efficiency decreases at high temperatures. The highest radiative efficiencies of direct-gap semiconductors can be obtained at cryogenic temperatures.

Auger recombination

Another important non-radiative recombination mechanism in the bulk is Auger recombination.

In this process, the energy becoming available through electron-hole recombination (approximately E_g), is dissipated by the excitation of a free

electron high into the conduction band, or by the excitation of a hole deep into the valence band. The processes are shown schematically in Fig. 2.2. The highly excited carriers will subsequently lose energy by multiple phonon emission until they are close to the band edge.

The recombination rates due to the two Auger processes shown in Fig. 2.2 are given by

$$R_{Auger} = C_p n p^2 \tag{2.14}$$

and

$$R_{Auger} = C_n n^2 p \quad . \tag{2.15}$$

Auger recombination is proportional to the square of the carrier concentration (either p^2 or n^2)since two carriers of the same type (either two holes or two electrons) are required for the recombination process. The first process (see Eq. 2.14) is more likely to happen in p-type semiconductors due to the abundance of holes. The second process (see Eq. 2.15) is more likely to happen in n-type semiconductors due to the abundance of electrons. The two Auger coefficients C_p and C_n are generally different.

In the high-excitation limit in which the non-equilibrium carriers have a higher concentration than equilibrium carriers, the Auger rate equations reduce to

$$R_{Auger} = \big(C_p + C_n\big) n^3 = C n^3 \tag{2.16}$$

where C is the Auger coefficient. The numerical values of Auger coefficients can be determined by a quantum mechanical calculation. Typical values for the Auger coefficient are 10^{-28} - 10^{-29} cm^6/s for III-V semiconductors.

Auger recombination reduces the luminescence efficiency in semiconductors only at very high excitation intensities. This is due to the cubic carrier concentration dependence. At lower carrier concentrations, the Auger recombination rate is very small and can be neglected for practical purposes.

2.1.3 Non-radiative recombination at surfaces

Substantial non-radiative recombination can occur at the semiconductor surfaces. Surfaces are a strong perturbation of the periodicity of a crystal lattice.

Recall that the band diagram model is based on the strict periodicity of the lattice. Since this periodicity ends at surfaces, the band diagram will need to be modified at the semiconductor surfaces. This modification includes the addition of electronic states within the forbidden energy gap of the semiconductor.

We consider now a semiconductor surface from a chemical point of view. Atoms at the surface cannot have the same bonding structure as bulk atoms due to the lack of neighboring atoms. Thus, some of the valence orbitals do not form a chemical bond. These partially filled electron orbitals, or dangling bonds, are electronic states that can be located in the forbidden energy gap of the semiconductor where they act as recombination centres. Depending on the charge state of these valence orbitals, these states can be acceptor-like or donor-like.

The dangling bonds may rearrange themselves and form bonds between neighboring atoms in the same surface plane. This surface reconstruction can lead to a locally new atomic structure with state energies different from those of the atomic structure in the bulk. The surface bonding structure depends on the specific nature of the semiconductor surfaces. The energetic location of surface electronic states is very difficult to predict, even with powerful theoretical models. Thus, phenomenological models of surface recombination are commonly used.

Surface recombination can occur only when both types of carriers are present. It is important in the design of LEDs that the carrier injected active region, in which naturally both types of carriers are present, is far from any surface. This can be achieved, for example, by carrier injection under a contact that is much smaller than the semiconductor die. Furthermore, the contact must be sufficiently far away from the side surfaces of the die. If the current flow is confined to the region below the contact, carriers will not "see" any semiconductor surfaces. Note that unipolar regions of a semiconductor device, e.g. the confinement regions, are not affected by surface recombination due to the lack of minority carriers.

Several passivation techniques have been developed to reduce the surface recombination in semiconductors, including treatments with sulfur, and other

chemicals.

2.1.4 Competition between radiative and non-radiative recombination

In light-emitting devices between radiative and non-radiative recombination the first one is the preferred process. However, non-radiative recombination can, under practical conditions, never be reduced to zero. Thus, there is competition between radiative and non-radiative recombination.

So far we have seen that several mechanisms for non-radiative recombination exist, including Shockley-Read-Hall, Auger, and surface recombination. All three mechanisms can be reduced, but none of the three can be totally eliminated.

For example, surface recombination can be drastically reduced by device designs that spatially separate the active region from all surfaces. However even if the separation is large, a few carriers will still diffuse to the surface and recombine there.

Just as for surface recombination, even non-radiative Shockley and Auger recombinations can never be totally avoided. For example any semiconductor crystal will have some native defects. Even though the concentration of these native defects can be low, it is never zero.

Another issue is the chemical purity of semiconductors. It is difficult to fabricate materials with impurity levels lower than the parts per billion (ppb) range. Thus, even the purest semiconductors contain impurities in the 10^{12} cm^{-3} range.

We calculate the internal quantum efficiency in a semiconductor with non-radiative recombination centres. If the radiative lifetime is denoted as τ_r and the non-radiative lifetime is denoted as τ_{nr}, then the total probability of recombination $1/\tau$ is given by the sum of the radiative and non-radiative recombination probabilities $1/\tau_r$ and $1/\tau_{nr}$:

$$\tau^{-1} = \tau_r^{-1} + \tau_{nr}^{-1} \quad . \tag{2.17}$$

The relative probability of radiative recombination is given by the radiative recombination probability over the total probability of recombination. Thus, the probability of radiative recombination or internal quantum efficiency is given by

$$\eta_{int} = \frac{\tau_r^{-1}}{\tau_r^{-1} + \tau_{nr}^{-1}} \quad . \tag{2.18}$$

The internal quantum efficiency gives the ratio of the number of light quanta emitted inside the semiconductor to the number of charge quanta undergoing recombination. Note that not all photons emitted internally may escape from the semiconductor due to the light-escape problem, reabsorption in the substrate, or other reabsorption mechanisms.

2.2 LED structures

In this section different LED structures will be analyzed, from the older ones, which gave low effciencies, to the new ones, which give higher efficiencies.

2.2.1 *p*-*n* homojunction

The basic structure of a LED is the p-n homojunction. The p-n homojunction is the structure obtained by joining two parts of the same material, one doped n and one doped p. To build a model for the p-n homojunction, we begin by considering initially separate n-type and p-type crystals of the same semiconductor material. When these are brought into intimate contact, the large difference in electron and hole concentrations between the two crystals causes electrons to diffuse from the n-type semiconductor into the p-type semiconductor and holes to diffuse from the p-type semiconductor into the n-type semiconductor. As electrons move from the n-type region into the p-type region, they leave behind uncompensated donor atoms near the junction, at the same time as holes move from the p-type region into the n-type region they leave behind uncompensated acceptor atoms near the junction. This flowing of electrons and holes causes the formation near the junction of a region which we can consider completely depleted of mobile carriers, called

depletion region. In the depletion region, due to the charge associated with the uncompensated dopant atoms, an electric field is created. The electric field lines extend from the donor ions on the n-type side of the junction to the acceptor ions on the p-type side of the junction. Thus this electric field tends to stop the diffusion of mobile carriers. As diffusion of mobile carriers goes on the depletion region becomes wider and the electric field increases. In the end equilibrium is reached, that is the magnitude of the electric field is such that the tendency of electrons to diffuse from the n-type region into the p-type region is exactly balanced by the tendency of electrons to drift in the opposite direction under the influence of the built-in electric field, at the same time the tendency of holes to diffuse from the p-type region into the n-type region is exactly balanced by the tendency of holes to drift in the opposite direction under the influence of the built-in electric field. The electric field creates a potential barrier between the two types of material. Fig. 2.3 shows the energy band diagram for a generic p-n homojunction under zero bias and under forward bias.

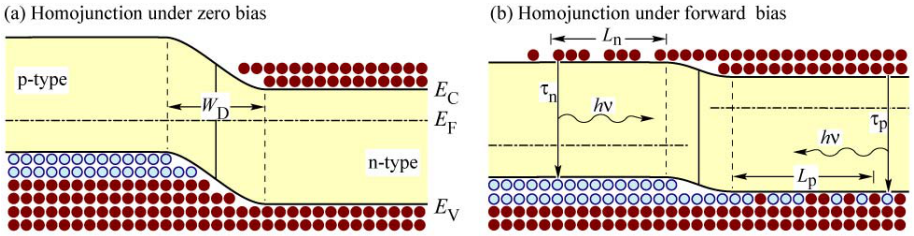

Figure 2.3: Energy band diagram of a p-n homojunction under zero bias and forward bias

The magnitude of the built-in potential barrier associated with the built-in electric field can be found by considering the difference in the Fermi energies of the initially separate materials. When the combined semiconductor regions are at equilibrium, the Fermi energy must be constant throughout the entire system. Consequently, the energy barrier that forms between the two materials must equal the difference between the Fermi energies in the separate pieces of semiconductor. This difference is equivalent to the difference in work functions of the separate semiconductor regions because the work function of a semiconductor is defined as $q\Phi_S \equiv qX + (E_c + E_f)$ where

qX is the electron affinity. If a reverse bias is applied the potential barrier is increased and the depletion region becomes wider. If a forward bias is applied the potential barrier is reduced, mobile carriers can flow from the region where they are majority to the opposite region where they recombine and the depletion region becomes narrower.

Since recombination occurs over a large region, p-n homojunction has very low efficiency. Thus it is not used for LED devices.

2.2.2 p-n heterojunction

The heterojunction is the structure obtained by joining two different semiconductor materials. In general in a heterojunction both energy gaps and electron affinities can be different. We consider only the band alignment shown in which the conduction band edge of the wider energy gap material is at a higher energy than that one of the narrower energy gap material and the valence band edge of the wider energy gap material is at a lower energy than that one of the narrower energy gap material. In particular, we consider the heterojunction formed between a wide energy gap n-type material and a narrower energy gap p-type material.

When we bring the two materials into intimate contact charge flows to establish equilibrium, an electrical field is created that opposes the diffusion of carriers to regions of lower concentrations and in the end equilibrium is reached. Fig. 2.4 shows the energy band diagram for a generic p-n heterojunction. The conduction and valence band edges, E_c and E_v, are not continuos at the boundary between the two materials. The relative positions of the band edges across the boundary depend on the magnitude of the energy gaps and of the electron affinities. The conduction band has a discontinuity equal to $\Delta E_c = qX_2 - qX_1$, the valence band has instead a discontinuity $\Delta E_v = E_{g1} - E_{g2} - \Delta E_c$. For the case we are considering, a "spike" and a "notch" appear in the conduction band.

If a forward bias is applied the energy barrier that electrons see reduces and electrons can flow into the p-type region where they recombine.

Even the p-n heterojunction's efficiency can be improved. The main

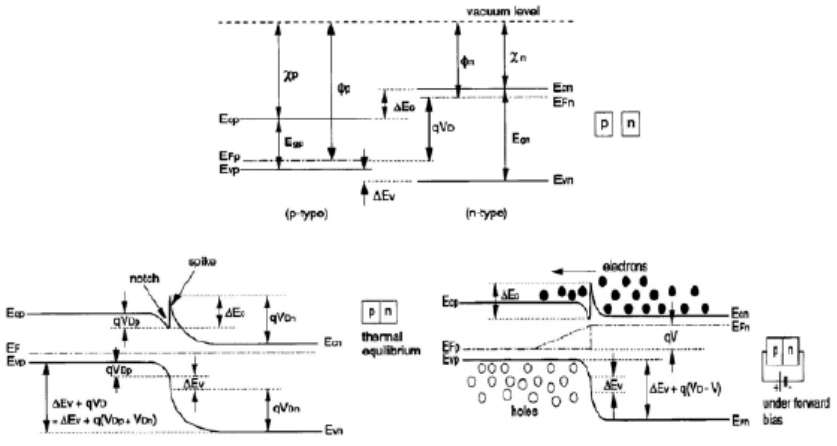

Figure 2.4: Energy band diagram of a p-n heterojunction under zero bias and forward bias

solution to increase efficiency of optoelectronic devices is to increase the confinement of injected carriers. This is achieved with heterostructures and quantum well structures.

2.2.3 Double heterostructures

A double heterostrucuture consists of two heterojunction, that is a sequence of three different semiconductors, a p-type wide energy gap semiconductor, a p-type small energy gap semiconductor, and a n-doped wide energy gap semiconductor. When a forward bias is applied electrons and holes drift from the wide energy gap regions to the central region. Due to the difference between the energy gaps of the three semiconductors both electrons and holes remain blocked in the central region. The high carrier confinement situation achieved by this structure grants fast recombination of the carriers. Fig. 2.5 shows the energy band diagram of a p-p-n double heterojunction.

The growth of heterostructures with desired energy gaps is not easy, the lattice and thermal coefficient mismatch between the layers must be minimum in order to minimize dislocation density and thus non radiative recombination.

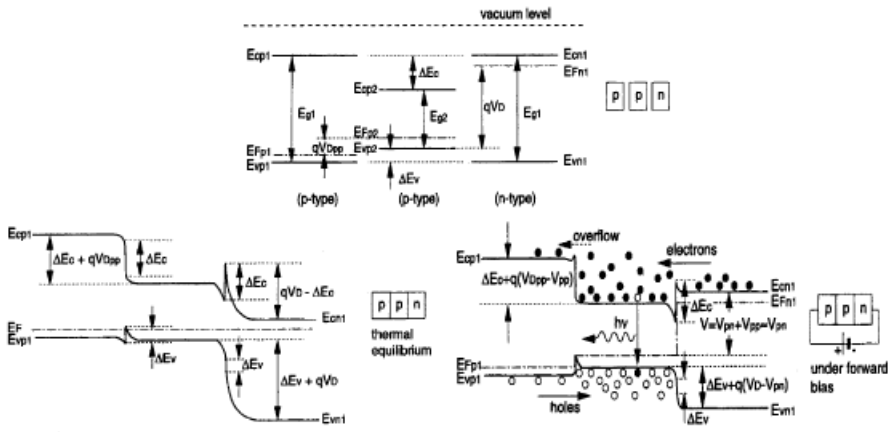

Figure 2.5: Energy band diagram of a *p-p-n* double heterojunction

2.2.4 Quantum well structures

The narrowing of the thickness of the middle (low energy gap) semiconductor layer of the double heterostructure would have a pejorative effect. The leakage current would increase as the structure would lose the ability to contain carriers. However, when the thickness of the active layer becomes comparable or smaller than the de Broglie wavelength of the electrons in the crystal, the active layer is called quantum well (QW) and quantum phenomena take place. A property of the QW is that carrier free motion along the perpendicular direction to the heterointerface is not possible, discrete energy levels, E_n, occur instead. In the y-z plane, which is parallel to the heterointerface, the carrier motion is not quantized. For a finite symmetrical potential quantum well, the electron energy is given by

$$E = \frac{\eta^2 k^2}{2m_e} + \frac{\eta^2 q_n^2}{2m_e} \tag{2.19}$$

where the value of q_n is found from solution of the following equation:

$$\frac{q_n a}{2} = \frac{n\pi}{2} - \arcsin\left(\frac{q_n \eta}{\sqrt{2m_e U_0}}\right) \quad . \tag{2.20}$$

The carrier state density is then quantized as presented in Fig. 2.6.

This means that electrons and holes must have a finite number of possible

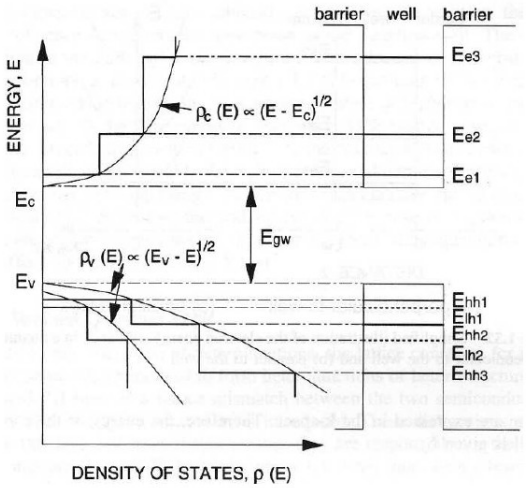

Figure 2.6: State density and quantized energies of a SQW structure

energy state inside the well. If more quantum wells are placed one close to another (at less than 5 nm), in a regular structure, a Multi Quantum Well (MQW) is obtained. In a MQW structure a tunnel transport phenomenon sets up between quantum wells. This leads to the creation of a continuity of quantized energy levels through the entire structure.

2.2.5 Blocking layers

A further increase in device efficiency may be obtained by a maximization of the electron confinement in active region. Carriers tend to escape from the active region, in particular if the QW region or the MQW regions present a little gap difference and thus offer poor carrier confinement. To reduce carrier leakage out of the active region, carrier-blocking layers are used. They are high energy gap layers located at active region borders.

2.3 LED optical properties

2.3.1 Internal, extraction, external and power efficiencies

The active region of an ideal LED emits one photon for every electron injected. Thus the active region of an ideal LED has a parameter called internal quantum efficiency of unity. The internal quantum efficiency is defined as

$$\begin{aligned}\eta_{int} &= \frac{number\,of\,photons\,emitted\,from\,active\,region\,per\,second}{number\,of\,electrons\,injected\,into\,LED\,per\,second} \\ &= \frac{P_{int}/(h\nu)}{I/e}\end{aligned} \tag{2.21}$$

where P_{int} is the optical power emitted from the active region and I is the injection current.

Photons emitted by the active region should escape from the LED die. In an ideal LED, all photons emitted by the active region are emitted into free space. Thus an ideal LED has unity a parameter called extraction efficiency. The extraction efficiency is defined as

$$\begin{aligned}\eta_{extraction} &= \frac{number\,of\,photons\,emitted\,into\,free\,space\,per\,second}{number\,of\,photons\,emitted\,from\,active\,region\,per\,second} \\ &= \frac{P/(h\nu)}{P_{int}/(h\nu)}\end{aligned} \tag{2.22}$$

where P is the optical power emitted into free space. However, in a real LED, not all the power emitted from the active region is emitted into free space. Some photons may never leave the semiconductor die. This is due to several possible loss mechanisms. For example light emitted by the active region can be reabsorbed in the substrate of the LED, assuming that the LED substrate is absorbing at the emission wavelength. Light may be incident on a metallic contact surface and be absorbed by the metal. In addition the phenomenon of total internal reflection, also referred to as the trapped light phenomenon, reduces the ability of the light to escape from the semiconductor.

The extraction efficiency can be a severe limitation for high-performance LEDs. It is quite difficult to increase the extraction efficiency beyond 50 % without resorting to highly sophisticated and costly device processes.

Another parameter that is defined is the external quantum efficiency. The external quantum efficiency is defined as

$$\begin{aligned}\eta_{ext} &= \frac{number\,of\,photons\,emitted\,into\,free\,space\,per\,second}{number\,of\,electrons\,injected\,into\,LED\,per\,second} \\ &= \frac{P/(h\nu)}{I/e} = \eta_{int}\eta_{extraction} \quad .\end{aligned} \tag{2.23}$$

The external quantum efficiency gives the ratio of the number of photons emitted into free space per second to the number of injected charge particles per second.

Another parameter that is defined is the power efficiency. The power efficiency is defined as

$$\eta_{power} = \frac{P}{IV} \tag{2.24}$$

where IV is the electrical power provided to the LED.

2.3.2 Emission spectrum

The physical mechanism by which semiconductor LEDs emit light is radiative recombination of electron-hole pairs, therefore with the simultaneous emission of photons. Recombination has certain characteristics that determine the optical properties of LEDs. The properties of emission in LEDs will be discussed in this section.

An electron-hole recombination process is illustrated schematically in Fig. 2.7. Electrons in the conduction band and holes in the valence band are assumed to have the parabolic dispersion relations

$$E_e = E_C + \frac{k^2}{2m_e^*} \quad (for\,electrons) \tag{2.25}$$

and

$$E_h = E_V - \frac{k^2}{2m_h^*} \quad (for\,holes) \tag{2.26}$$

where m_e^* and m_e^* are the electron and hole effective masses, $\hbar$ is Planck's constant divided by 2π, k is the wave number, and E_V and E_C are the valence and conduction band edges, respectively.

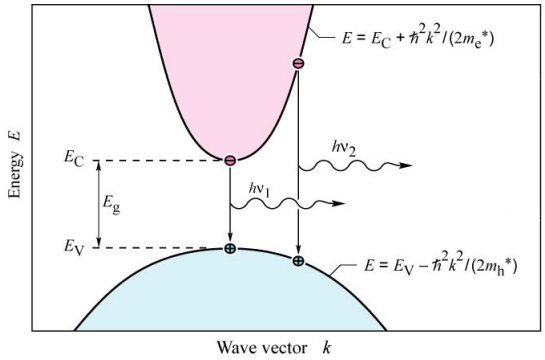

Figure 2.7: Parabolic electron and hole dispersion relations

We know from the Boltzmann distribution that electrons and holes have an average kinetic energy of kT. We also know that the photon energy is given by the difference between the electron energy, E_e, and the hole energy, E_h, i.e.

$$h\nu = E_e - E_h \approx E_g \quad . \tag{2.27}$$

The photon energy is approximately equal to the bandgap energy, E_g, if the thermal energy is small compared with the bandgap energy $kT \ll E_g$. Thus the desired emission wavelength of a LED can be attained by choosing a semiconductor material with an appropriate energy bandgap.

Precisely the photon energy can be written as the joint dispersion relation

$$\begin{aligned} h\nu = E_e - E_h &= E_C + \frac{\hbar^2k^2}{2m_e^*} - E_V + \frac{\hbar^2k^2}{2m_h^*} = E_g + \frac{\hbar^2k^2}{2}\left(\frac{1}{m_e^*} + \frac{1}{m_h^*}\right) \\ &= E_g + \frac{\hbar^2k^2}{2m_r^*} \end{aligned} \tag{2.28}$$

where m_r^* is the reduced mass given by

$$\frac{1}{m_r^*} = \frac{1}{m_e^*} + \frac{1}{m_h^*} \quad . \tag{2.29}$$

Using the joint dispersion relation, the joint density of states can be calculated and one obtains

$$\rho(E) = \frac{1}{2\pi^2}\left(\frac{2m_r^*}{\hbar^2}\right)^{3/2}\sqrt{E - E_g} \quad . \tag{2.30}$$

The distribution of carriers in the allowed bands is given by the Boltzmann distribution, i.e.

$$f_B(E) = e^{-E/(kT)} \quad . \tag{2.31}$$

The emission intensity as a function of energy is proportional to the product of Eqs. 2.30 and 2.31,

$$I(E) \propto \sqrt{E - E_g}e^{-E/(kT)} \quad . \tag{2.32}$$

The lineshape of a LED, as given by Eq. 2.32, is shown in Fig. 2.8. The maximum emission intensity occurs at

$$E = E_g + \frac{1}{2}kT \quad . \tag{2.33}$$

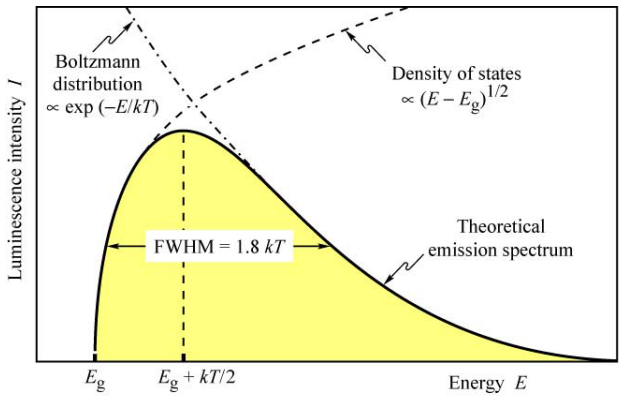

Figure 2.8: Theoretical emission spectrum of a LED

The full-width at half-maximum of the emission is

$$\Delta E = 1.8kT \quad \text{or} \quad \Delta\lambda = \frac{1.8kT\lambda^2}{hc} \quad . \tag{2.34}$$

The spectral linewidth of LED emission is important in several respects. Firstly, the linewidth of a LED emitting in the visible range is relatively narrow compared with the range of the entire visible spectrum. The LED emission is even narrower than the spectral width of a single colour as perceived by the human eye. For example, red colours range in wavelength from 625 to 730 nm, which is much wider than the typical emission spectrum of a LED. Therefore, LED emission is perceived by the human eye as monochromatic.

2.3.3 The light escape cone

Light generated inside a semiconductor cannot escape from the semiconductor if it is totally internally reflected at the semiconductor-air interface. If the angle of incidence of a light ray is close to normal incidence total internal reflection does not occur and the light ray can escape from the semiconductor. Total internal reflection occurs for light rays with oblique and grazing-angle incidence. Total internal reflection significantly reduces the external quantum efficiency, in particular for LEDs consisting of high-refractive-index materials.

Let us assume that the angle of incidence in the semiconductor at the semiconductor-air interface is given by ϕ. Then the angle of incidence of the refractive ray, Φ, can be inferred from Snell's law

$$n_s \sin\phi = n_{air} \sin\Phi \tag{2.35}$$

where n_s and n_{air} are the refractive indices of the semiconductor and the air, respectively. The critical angle ϕ_c for total internal reflection is obtained using $\Phi = 90°$, as illustrated in Fig. 2.9. Using Snell's law, one obtains

$$\sin\phi_c = \frac{n_{air}}{n_s} \sin 90° = \frac{n_{air}}{n_s} \tag{2.36}$$

and

$$\phi_c = \arcsin\frac{n_{air}}{n_s} \quad . \tag{2.37}$$

The refractive indices of semiconductors are usually quite high. Thus,

according to Eq. 2.37, the critical angle for total internal reflection is quite small. In this case, we can use the approximation $\sin\phi_c \approx \phi_c$. The critical angle for total internal reflection is then given by

$$\phi_c \approx \frac{n_{air}}{n_s} \quad . \tag{2.38}$$

The angle of total internal reflection defines the light escape cone. Light emitted into the cone can escape from the semiconductor, whereas light emitted outside the cone is subjected to total internal reflection.

Next, we calculate the surface area of the spherical cone with radius r in order to determine the total fraction of light that is emitted into the light escape cone. The surface area of the calotte-shaped surface shown in Fig. 2.9 is given by the integral

$$A = \int dA = \int_{\phi=0}^{\phi_c} 2\pi r \sin\phi r d\phi = 2\pi r^2(1 - cos\phi_c) \quad . \tag{2.39}$$

Let us assume that light is emitted from a point-like source in the semiconductor with a total power of P_{source}. Then the power that can escape from the semiconductor is given by

$$P_{escape} = P_{source}\frac{2\pi r^2(1-\cos\phi_c)}{4\pi r^2} \tag{2.40}$$

where $4\pi r^2$ is the entire surface area of the sphere with radius r.

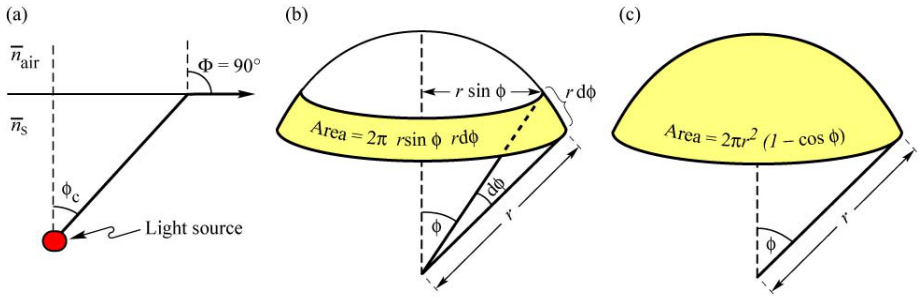

Figure 2.9: (a) Definition of the light escape cone (b) Area element dA (c) Area of calotte-shaped section of the sphere defined by radius r and angle ϕ_c

The calculations indicate that only a fraction of the light emitted inside a semiconductor can escape from the semiconductor. This fraction is given by

$$\frac{P_{escape}}{P_{source}} = \frac{1}{2}(1 - \cos\phi_c) \quad . \tag{2.41}$$

Because the critical angle of total internal reflection for high-index materials is relatively small, the cosine term can be expanded into a power series. Neglecting higher-than-second-order terms yields

$$\frac{P_{escape}}{P_{source}} \approx \frac{1}{2}\left[1 - \left(1 - \frac{\phi_c^2}{2}\right)\right] = \frac{1}{4}\phi_c^2 \quad . \tag{2.42}$$

Using the approximation of Eq. 2.38, one obtains

$$\frac{P_{escape}}{P_{source}} \approx \frac{1}{4}\frac{n_{air}^2}{n_s^2} \quad . \tag{2.43}$$

The escape problem is a significant problem for high-efficiency LEDs. In most semiconductors, the refractive index is quite high (more than 2.5) and thus only a small percentage of the light generated in the semiconductor can escape from the LED. The problem is less significant in semiconductors with a small refractive index, which have refractive indices of the order of 1.5.

The light escape cone can be enhanced by using encapsulants with a large refractive index. As a result of the incapsulation, the angle of total internal reflection through the top surface of the semiconductor is increased. Fig. 2.10 shows schematically a LED without encapsulant and one with encapsulant.

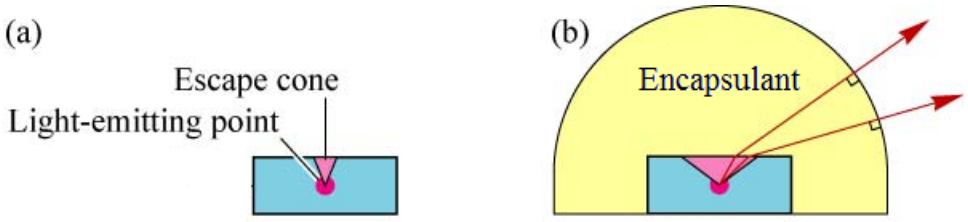

Figure 2.10: LED (a) without and (b) with encapsulant

2.4 Packaging

Virtually all LEDs are mounted in a package that provides two electrical leads, a transparent optical window for the light to escape, and, in power packages, a thermal path for heat dissipation. The chip-encapsulating material advantageously possesses high optical transparency, a high refractive index, chemical inertness, high-temperature stability, and hermeticity.

Power packages have a direct, thermally conductive path from the LED chip, through the package, to a heat sink, e.g. a printed circuit board. A power package is shown in Fig. 2.11. The power package shown in the figure

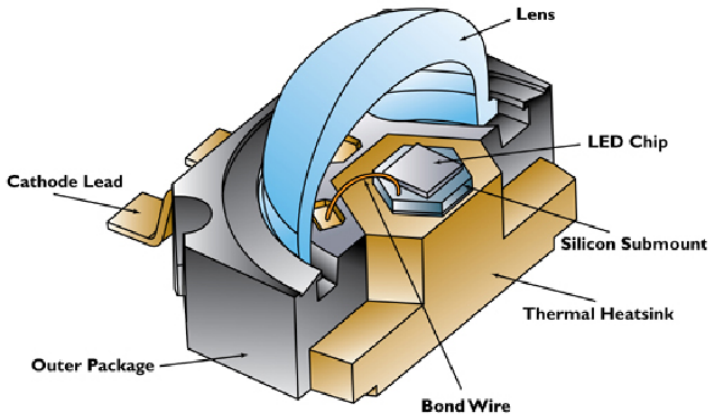

Figure 2.11: Cross section of a high power package

has several advanced features. Firstly, the package contains an Al or Cu heatsink slug with low thermal resistivity to which the LED submount is soldered by a metal-based solder. Secondly, the chip is directly mounted on a Si submount that includes electrostatic discharge protection (ESD).

Chapter 3

Solid state lighting

The field of solid state lighting (SSL) is concerned with the development of solid state sources for illumination applications. As the trend of higher efficiencies in LEDs continues, the number of possible applications increases a well. A highly interesting application with a very large potential market size is general illumination in homes and offices. The problem is that LEDs are inherently monochromatic emitters. However, there are several ways to generate white light using LEDs. Approaches to white light generation based only on LEDs will be only mentioned, whereas approaches based on LEDs and wavelength-converting materials will be discussed in more detail.

In the field of general illumination, devices should have the following properties:

- high efficiency
- high power capability
- good colour-rendering capabilities
- high reliability
- low-cost manufacturability
- environmental benignity

Such properties would allow LEDs to compete with conventional illumination sources, in particular incandescent and fluorescent lamps.

Before considering white light sources we will examine human vision mechanisms.

3.1 The human eye

The recipient of the light emitted by most visible spectrum LEDs is the human eye. In this section the main characteristics related to human eye and human vision are summarized.

Fig. 3.1 shows a schematic illustration of the human eye. The inside of

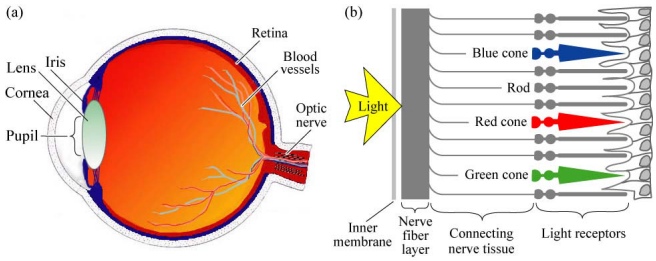

Figure 3.1: (a) Cross section through a human eye. (b) Schematic view of the retina including rod and cone light receptors

the eyeball is clad by the retina, which is the light sensitive part of the eye. Fig. 3.1 shows the cell structure of the retina including the light sensitive rod cells and cone cells. Also shown are the ganglion cells and nerve fibres that transmit the visual information to the brain. Rod cells are more abundant than cone cells and more light sensitive than cone cells. There are three types of cone cells, namely cone cells sensitive in the red, green and blue spectral range. The cone cells are therefore denoted as the red sensitive, green sensitive and blue sensitive cones, or simply as the red, green and blue cones. The illustration also shows the fovea, a cone rich central region of the retina which affords the high acuteness of central vision.

Three different vision regimes are shown in Fig. 3.2 along with the receptors relevant to each of the regimes. Photopic vision relates to human vision at high ambient light levels (e.g. during daylight conditions) when

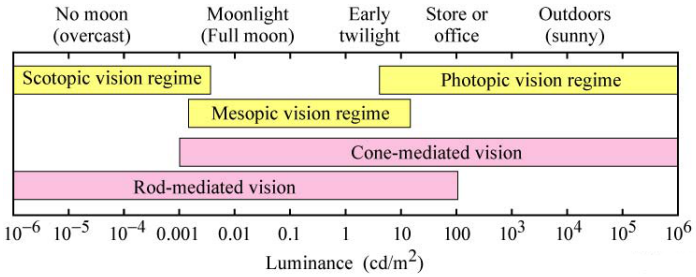

Figure 3.2: Approximate ranges of vision regimes and receptor regimes

vision is mediated by the cones. The photopic vision regime applies to luminance levels higher than 3 cd/m^2. Scotopic vision relates to human vision at low ambient light levels (e.g. at night) when vision is mediated by rods. Rods are much more abundant and have a much higher sensitivity than the cones. The scotopic vision regime applies to luminance levels lower than 0.003 cd/m^2. Mesopic vision relates to light levels between the photopic vision and scotopic vision regime (luminance levels between 0.003 cd/m^2 and 3 cd/m^2).

3.2 Radiometric and photometric units

The physical properties of electromagnetic radiation are characterized by radiometric units. Using radiometric units, we can characterize light in terms of physical quantities; for example, the number of photons, the photon energy, the optical power (in the lighting community frequently called the radiant flux), the radiant intensity, the optical power density (in the lighting community frequently called the irradiance) and the radiance. However, the radiometric units are irrelevant when it comes to light perception by a human being. For example, infrared radiation causes no luminous sensation in the eye. To characterize the light and colour sensation by the human eye, different types of units are needed. These units are called photometric units.

The luminous flux, which is a photometric quantity, represents the optical power of a source as perceived by the human eye. The unit of luminous flux is the lumen (lm). The lumen is an SI unit. It is defined as follows: a

monochromatic light source emitting an optical power of (1/683) watt at 555 nm has a luminous flux of 1 lumen (lm). The luminous intensity, which is also a photometric quantity, represents the radiant intensity of an optical source, as perceived by the human eye.

The luminous intensity is measured in units of candela (cd), which is a base unit of the International System of Units (SI unit). The present definition of luminous intensity is as follows: a monochromatic light source emitting an optical power of (1/683) watt at 555 nm into the solid angle of 1 steradian (sr) has a luminous intensity of 1 candela (cd).

A comparison of the definitions for the candela and the lumen reveals that 1 candela equals 1 lumen per steradian or cd = lm/sr. Thus, an isotropically emitting light source with luminous intensity of 1 cd has a luminous flux of 4πlm = 12.57 lm.

The illuminance is the luminous flux incident per unit area. The illuminance is measured in lux (lux = lm/m^2). It is an SI unit and is used when characterizing illumination conditions.

The luminance of a surface source (i.e. a source with a non-zero light emitting surface area such as a display or a LED) is the ratio of the luminous intensity emitted in a certain direction (measured in cd) divided by the projected surface area in that direction (measured in m^2). The luminance is measured in units of cd/m^2. The projected surface area mentioned above follows a cosine law, i.e. the projected area is given by $A_{projected} = A_{surface} cos\Theta$, where Θ is the angle between the direction considered and the surface normal. The light-emitting surface area and the projected area are shown in Fig. 3.3. In most cases, the direction of interest is normal to the chip surface. In this

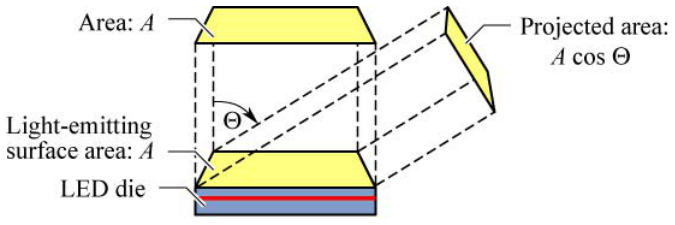

Figure 3.3: Area of LED, A, and projected area, $Acos\phi$

case, the luminance is the luminous intensity emitted along the chip-normal direction divided by the chip area.

For LEDs it is desirable to maximize luminous flux and luminous intensity while keeping the LED chip area minimal. Thus the luminance is a measure of how efficiently the valuable semiconductor wafer area is used to attain, at a given injection current, a certain luminous intensity.

Photometric units and corresponding radiometric units are summarized in Fig. 3.4.

Photometric unit	Dimension	Radiometric unit	Dimension
Luminous flux	lm	Radiant flux (optical power)	W
Luminous intensity	lm / sr = cd	Radiant intensity	W / sr
Illuminance	$lm / m^2 = lux$	Irradiance (power density)	W / m^2
Luminance	$lm / (sr\,m^2) = cd / m^2$	Radiance	$W / (sr\,m^2)$

Figure 3.4: Photometric and corresponding radiometric units

3.3 Eye sensitivity function

The conversion between radiometric and photometric units is provided by the eye sensitivity function (or luminous efficiency function).

In 1924, the CIE introduced a photopic eye sensitivity function for point-like light sources where the viewer angle is 2° (CIE, 1931). This function is referred to as the CIE 1931 $V(\lambda)$ function.

A modified photopic eye sensitivity function was introduced by Judd and Vos in 1978. The modification was motivated by the underestimation of the human eye sensitivity in the blue and violet spectral region by the CIE 1931 $V(\lambda)$ function. The modified eye sensitivity function has higher values in the spectral region below 460 nm. The CIE has endorsed the modified eye sensitivity function by stating "the spectral luminous efficiency function for a point source may be adequately represented by the Judd modified $V(\lambda)$ function" (CIE, 1988) and "the Judd modified $V(\lambda)$ function would be the preferred function in those conditions where luminance measurements of short

wavelengths consistent with colour normal observers is desired" (CIE, 1990). This modified function is here referred to as the CIE 1978 $V(\lambda)$ function.

The CIE 1931 $V(\lambda)$ function and the CIE 1978 $V(\lambda)$ function are shown in Fig. 3.5. The photopic eye sensitivity function has maximum sensitivity

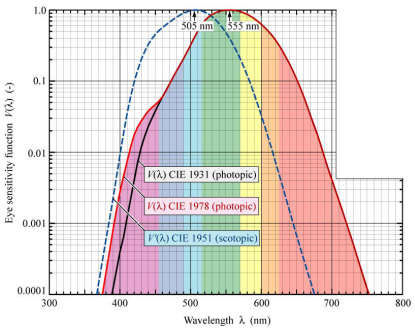

Figure 3.5: CIE 1931 and CIE 1978 eye sensitivity functions $V(\lambda)$ for the photopic vision regime. Also shown is the eye sensitivity function $V(\lambda)$ for the scotopic vision regime.

in the green spectral range at 555 nm, where both CIE 1931 and CIE 1978 $V(\lambda)$ have a value of unity, i.e. V(555 nm) = 1. Inspection of the figure also reveals that the CIE 1931 $V(\lambda)$ function underestimated the eye sensitivity in the blue spectral range (λ lower than 460 nm).

Also shown in Fig. 3.5 is the scotopic eye sensitivity function $V'(\lambda)$. The peak sensitivity in the scotopic vision regime occurs at 507 nm. This value is markedly shorter than the peak sensitivity in the photopic vision regime.

The CIE 1978 $V(\lambda)$ function, which can be considered the most accurate description of the eye sensitivity in the photopic vision regime, is shown in Fig. 3.6. The eye sensitivity function has been determined by the minimum flicker method, which is the classic method for luminance comparison and for the determination of eye sensitivity function. The stimulus is a small circular area, alternatingly illuminated (with a frequency of 15 Hz) with standard colour and the comparison colour. Since the hue-fusion frequency is lower than 15 Hz, the hues fuse. However, the brightness-fusion frequency is higher than 15 Hz and thus if the two colours differ in brightness then there will be visible flicker. The human subject's task is to adjust the target colour until the flicker is minimal.

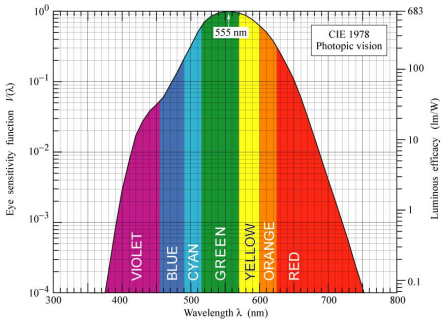

Figure 3.6: Eye sensitivity function $V(\lambda)$

Let us consider the CIE 1978 $V(\lambda)$ function.

For wavelengths ranging from 390 to 720 nm, $V(\lambda)$ is greater than 10^{-3}. Although the human eye is sensitive to light with wavelengths lower than 390 nm and higher than 720 nm, the eye sensitivity at these wavelengths is extremely low. Therefore, the wavelength range 390 nm $\leq \lambda \leq$ 720 nm can be considered the visible wavelength range. The relationship between colour and wavelength within the visible wavelength range is given in Fig. 3.7. This

Color	Wavelength
Ultraviolet	< 390 nm
Violet	390–455 nm
Blue	455–490 nm
Cyan	490–515 nm
Green	515–570 nm

Color	Wavelength
Yellow	570–600 nm
Amber	590–600 nm
Orange	600–625 nm
Red	625–720 nm
Infrared	> 720 nm

Figure 3.7: Colours and associated peak wavelength ranges

relationship is valid for monochromatic or near-monochromatic light sources such as LEDs. Note that colour is, to some extent, a subjective quantity. Also note that the transition between different colours is continuos.

3.4 Luminous efficacy and luminous efficiency

The luminous flux, Φ_{lum}, is obtained from the optical power using the equation

$$\Phi_{lum} = 683 \frac{lm}{W} \int_{\lambda} V(\lambda) P(\lambda) d\lambda \tag{3.1}$$

where $P(\lambda)$ is the spectral power, i.e. the optical power emitted per unit wavelength, and the prefactor 683 lm/W is a normalization factor. The optical power emitted by a light source is then given by

$$P = \int_{\lambda} P(\lambda) d\lambda \quad . \tag{3.2}$$

High-performance single-chip visible-spectrum LEDs can have a luminous flux of about 10 - 100 lm at an injection current of 100 - 1000 mA.

The luminous efficacy of optical radiation (also called the luminosity function) is the conversion efficiency from optical power to luminous flux and is measured in units of lumen per watt. The luminous efficacy is defined as

$$Luminous\,efficacy = \frac{\Phi_{lum}}{P} = \left[683 \frac{lm}{W} \int_{\lambda} V(\lambda) P(\lambda) d\lambda\right] / \left[\int_{\lambda} P(\lambda) d\lambda\right] \quad . \tag{3.3}$$

For strictly monochromatic light sources ($\Delta\lambda \rightarrow 0$), the luminous efficacy is equal to the eye sensitivity function $V(\lambda)$ multiplied by 683 lm/W. However, for multicolour light sources and especially for white light sources, the luminous efficacy needs to be calculated by integration over all wavelengths.

The luminous efficiency of a light source, also measured in units of lm/W, is the luminous flux of the light source divided by the electrical input power.

$$Luminous\,efficiency = \Phi_{lum}/(IV) \tag{3.4}$$

where the product (IV) is the electrical input power of the device. Note that in the lighting community, luminous efficiency is often referred to as luminous efficacy of the source.

Inspection of Eqs. 3.3 and 3.4 reveals that the luminous efficiency is the product of the luminous efficacy and the power efficiency.

The luminous efficiency is a highly relevant figure of merit for visible-spectrum LEDs. It is a measure of the perceived optical power normalized to the electrical power expended to operate the LED. For light sources with a perfect power conversion, the luminous efficiency is equal to the luminous efficacy of radiation.

Some LED structures attain excellent power efficiency by using small light-emitting areas (current injection in a small area of chip) and advanced light-output-coupling structures.

3.5 Science of colour

The assessment and quantification of colour is referred to as colorimetry or the "science of colour". Colorimetry is closely associated with human colour vision. Both colorimetry and human vision have attracted a great deal of interest that spans many centuries.

The human sense of vision is very different from the human sense of hearing. If we hear two frequencies simultaneously, e.g. two frequencies generated by a musical instrument, we will be able to recognize the musical tone as having two distinct frequencies. This is not the case for optical signals and the sense of vision. Mixing two monochromatic optical signals will appear to us as one colour and we are unable to recognize the original dichromatic composition of that colour.

Light causes different levels of excitation of the red, green, and blue cones. However, the sensation of colour caused by a particular light source varies slightly among different individuals. In fact, the sensation of colour is, to some extent, a subjective quantity. For these reasons, The International Commission for Illumination (Commission Internationale de l'Eclairage, CIE) has standardized the measurement of colour by means of colour-matching functions and chromaticity diagram (CIE, 1931).

Let us consider how to obtain colour-matching functions. Consider two lights lying side by side: One being monochromatic and the other one being a mixture of the three primary lights red, green, and blue. A human subject will be able to make the two lights appear identical (i.e. "match" them) by adjusting the relative intensities of the red, green, and blue light. The three colour-matching functions are obtained from a series of such matches, in which the subject sets the intensities of the three primary lights to match a series of monochromatic lights across the visible spectrum.

Subsequently, the measured set of colour-matching functions is mathem-

atically transformed into a new set of colour-matching functions for which the green colour-matching function $\overline{y}(\lambda)$, is chosen to be identical to the eye sensitivity function, $V(\lambda)$, i.e.

$$\overline{y}(\lambda) = V(\lambda) \quad . \tag{3.5}$$

The CIE 1931 and CIE 1978 colour-matching function $\overline{x}(\lambda)$, $\overline{y}(\lambda)$ and $\overline{z}(\lambda)$ are shown in Fig. 3.8. The three colour-matching functions reflect the fact

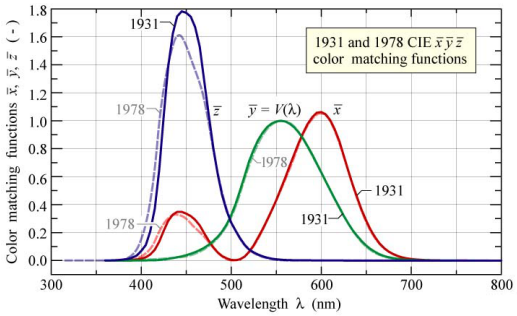

Figure 3.8: CIE 1931 and CIE 1978 colour-matching functions

that human colour vision possesses trichromacy, that is, the colour of any light source can be described by just three variables. Note that $\overline{x}(\lambda)$, $\overline{y}(\lambda)$ and $\overline{z}(\lambda)$ are dimensionless quantities.

For a given spectral power distribution $P(\lambda)$, the degree of stimulation of the three primary lights required to match the colour of $P(\lambda)$ is given by

$$X = \int_{\lambda} \overline{x}(\lambda) P(\lambda) d\lambda \tag{3.6}$$

$$Y = \int_{\lambda} \overline{y}(\lambda) P(\lambda) d\lambda \tag{3.7}$$

$$Z = \int_{\lambda} \overline{z}(\lambda) P(\lambda) d\lambda \tag{3.8}$$

where X, Y, and Z are tristimulus values that give the stimulation (i.e. power) of each of the three primary red, green, and blue lights needed to match the colour of $P(\lambda)$. Large values of X, Y, and Z indicate red, green, and blue colours of the spectrum $P(\lambda)$, respectively.

Because of the distinct similarity of the colour-matching functions on one hand, and the three retinal-cones-sensitivity functions on the other hand (both groups of functions have three peaks), each tristimulus value represents the approximate (but not exact) degree of stimulation that each type of retinal cone experiences when illuminated by a light source with spectral power distribution $P(\lambda)$.

The chromaticity coordinates x and y are calculated from the tristimulus values according to

$$x = \frac{X}{X+Y+Z} \tag{3.9}$$

$$y = \frac{Y}{X+Y+Z} \quad . \tag{3.10}$$

Thus, the value of a chromaticity coordinate is the stimulation of each primary light (or approximately of each type of retinal cone) divided by the entire stimulation $(X + Y + Z)$. The value of the z chromaticity coordinate is calculated analogously, that is

$$z = \frac{Z}{X+Y+Z} = 1 - x - y \quad . \tag{3.11}$$

Note that the z chromaticity coordinate can be obtained from x and y, so that there is no new information provided by the z chromaticity coordinate. Therefore, the z chromaticity coordinate is redundant and, for this reason does not need to be used.

The (x, y) chromaticity diagram is shown in Fig. 3.9. Reddish and greenish colours are found for large values of x and y, respectively. Bluish colours are found for large values of z, which is, according to Eq. 3.11, for low values of x and y, or near the origin of the chromaticity diagram.

The chromaticity diagram of Fig. 3.10 shows a detailed attribution of colours to the locations in the chromaticity diagram. An assignment of common colours in the chromaticity diagram is given in Fig. 3.11. All colours can be characterized in terms of their location in the chromaticity diagram. Monochromatic colours are found on the perimeter of the chromaticity diagram. White light is found in the centre of the chromaticity diagram. The figure

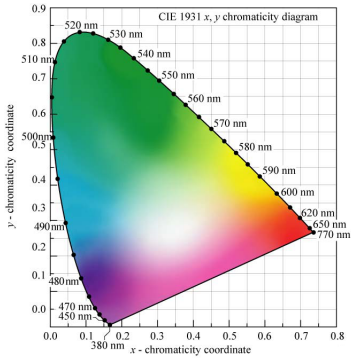

Figure 3.9: CIE 1931 (x, y) chromaticity diagram

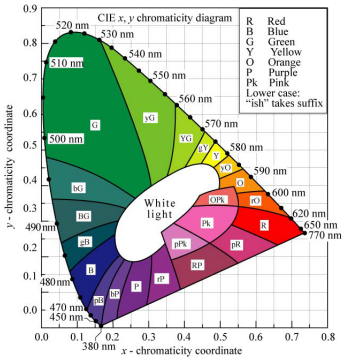

Figure 3.10: CIE 1931 chromaticity diagram with areas attributed to distinct colours

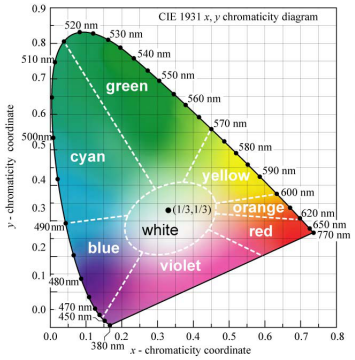

Figure 3.11: CIE 1931 (x, y) chromaticity diagram with areas attributed to common colours

also shows the equal energy point located in the centre of the chromaticity diagram at $(x, y) = (1/3, 1/3)$. The optical spectrum correspondent to the equal energy point has a constant spectral power distribution, i.e. the optical power per wavelength interval $\mathrm{d}\lambda$ is constant across the visible spectrum.

An important characteristic of a white light source is its ability to show (i.e. render) the true colours of physical objects, e.g. fruit, plants or toys, that are being illuminated by the white light source. The ability of the white light source to render the colours of an object is measured in terms of the colour-rendering index or CRI. It is a measure of the ability of the white illumination source to faithfully render the colours of physical objects illuminated by the source.

The ideal white light source that perfectly renders the true colours of objects has colour-rendering index equal to 100. All real white light sources have colour-rendering indices lower than 100.

3.6 White light sources based on LEDs

Light is perceived as white light if the three types of cones located on the retina of the human eye are excited in a certain ratio, namely with similar intensity. For the case of white light, the tristimulus values are such that the location of the chromaticity point is near the centre of the chromaticity diagram.

The generation of white light can be accomplished with a huge number of possible spectra. The creation of white light out of monochromatic visible spectrum emitters can be based on dichromatic, trichromatic, or tetrachromatic approaches, as shown in Fig. 3.12 or on approaches of higher chromaticity.

The optical sources can be classified in terms of their luminous efficiency and colour-rendering properties. Whereas high luminous efficiency is always a desirable property of light sources, the importance of colour rendering depends strongly on the application. Generally, high quality illumination applications, e.g. illumination in museums, homes, offices, and stores, require a high colour-rendering capability. However, there are numerous applications

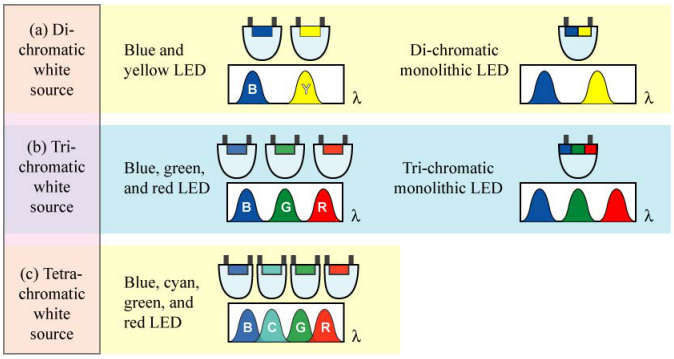

Figure 3.12: LED-based approaches for white light sources

where the colour rendering capability is of lower priority, for example in the illumination of streets, parking garages, and stairwells. Finally, in signage applications, colour rendering is irrelevant. Such signage applications include white pedestrian traffic lights, displays, and indicator lights.

There is a fundamental trade-off between the luminous efficiency and the colour rendering capability of a light source. Generally, dichromatic white light has the highest luminous efficiency and the poorest colour-rendering capabilities. A trichromatic white light source can have very acceptable colour-rendering properties (CRI higher than 80) and luminous efficiencies greater than 300 lm/W. Tetrachromatic white light sources can have colour-rendering indices greater than 90.

3.7 White light sources based on wavelength converters

The generation of white light by a semiconductor LED whose emitted light is partially or fully used to optically excite a wavelength converter material, is a viable and common method to generate white light for general illumination applications.

3.7.1 Efficiency of wavelength converter materials

The conversion efficiency of short wavelength light to long wavelength light by a wavelength converter(λ-converter) material is determined by two distinct factors, namely:

- the external quantum efficiency of the λ-converter
- the inherent energy loss incurred in wavelength conversion

The external quantum efficiency of the wavelength converter material, η_{ext}, is given by

$$\eta_{ext} = \frac{number\,of\,photons\,emitted\,into\,free\,space\,by\,\lambda\text{-}converter\,per\,second}{number\,of\,photons\,absorbed\,by\,\lambda\text{-}converter\,per\,second} \quad . \tag{3.12}$$

The external quantum efficiency originates from the internal quantum efficiency η_{int} and the extraction efficiency $\eta_{extraction}$ of the wavelength converter material. Between these three quantities the relation $\eta_{ext} = \eta_{int}\eta_{extraction}$ holds. Note that the internal quantum efficiency depends on the inherent efficiency of the material whereas the extraction efficiency depends on the spatial distribution of the λ-converter material. Generally, thin films have high extraction efficiencies whereas lumpy aggregations of wavelength converter materials have lower extraction efficiency due to reabsorption. It is therefore desirable to employ λ-converter materials in the form of thin layers.

The inherent wavelength conversion energy loss (sometimes called quantum deficit or Stokes shift)incurred when converting a photon with wavelength λ_1 to a photon with wavelength λ_2 (λ_1 lower than λ_2) is given by

$$\Delta E = h\nu_1 - h\nu_2 = \frac{hc}{\lambda_1} - \frac{hc}{\lambda_2} \quad . \tag{3.13}$$

Thus the wavelength conversion efficiency of the wavelength converter material is given by

$$\eta_{\lambda-conversion} = \frac{h\nu_2}{h\nu_1} = \frac{\lambda_1}{\lambda_2} \tag{3.14}$$

where λ_1 is the wavelength of the photon absorbed by the wavelength converter material and λ_2 is the wavelength of the photon emitted by the wavelength

converter material.

The overall conversion efficiency of a wavelength converter is the product of Eqs. 3.12 and 3.14

$$\eta = \eta_{ext}\eta_{\lambda-conversion} \tag{3.15}$$

The inherent wavelength conversion energy loss is the main reason that λ-converter-based white light sources have a fundamentally lower efficiency limit than white-light sources based on LEDs.

Most white light emitters use a LED emitting at short wavelength (e.g. blue) and a wavelength converter material. Some of the light emitted by the blue LED is absorbed in the wavelength converter material and then re-emitted as light with a longer wavelength. The types and characteristics of wavelength converter materials will be discussed below.

The possibility that white light can be generated in different ways raises the question as to which is the optimum way to generate white light. There are two parameters that need to be considered: firstly, the luminous efficiency and, secondly, the colour-rendering index. For signage applications, the luminous efficiency is of primary importance and the colour-rendering index is irrelevant. For illumination applications, both the luminous efficiency and the colour rendering index are important.

3.7.2 Wavelength converter materials

There are several types of wavelength converter materials including phosphors, semiconductors, and dyes. Wavelength converter materials have several parameters of interest, including the absorption wavelength, the emission wavelength, and the external quantum efficiency. A good converter has near 100 % external quantum efficiency. The overall conversion efficiency of a wavelength converter is given by

$$\eta = \eta_{ext}\frac{\lambda_1}{\lambda_2} \tag{3.16}$$

where η_{ext} is the external quantum efficiency of the converter, λ_1 is the wavelength of photons absorbed by the wavelength converter, and λ_2 is the

wavelength of photons emitted by the wavelength converter. Even if the external quantum efficiency is unity, there is always lost energy associated with the wavelength conversion process, so that the overall conversion efficiency of a wavelength converter is always less than unity.

The most common wavelength converter materials are phosphors and they will be discussed in greater detail in the following subsection. The optical absorption and emission spectrum of a commercial phosphor is shown in Fig. 3.13. The phosphor displays a higher energy absorption band and a

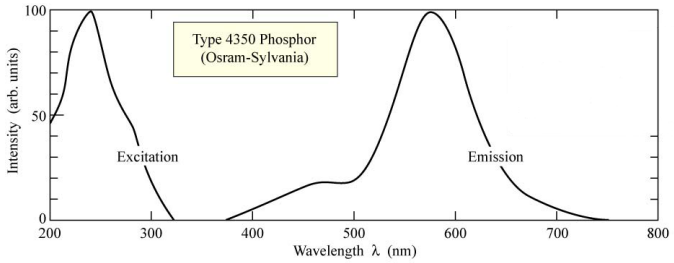

Figure 3.13: Absorption and emission spectrum of a commercial phosphor

lower energy emission band. The emission band is rather broad, making this particular phosphor suitable for white light emission. Phosphors are very stable materials and can have external quantum efficiencies close to 100 %. A common phosphor used for white LEDs is cerium-doped (Ce-doped) YAG phosphor. For Ce-doped phosphors, external quantum efficiencies of 75 % have been reported.

Dyes are another type of wavelength converter. Many different dyes are commercially available. An example of a dye optical absorption and emission spectrum is shown in Fig. 3.14. Dyes can have external quantum efficiencies close to 100 %. However, dyes, as organic molecules, lack the long term stability afforded by phosphors and semiconductors.

Finally, semiconductors are another type of wavelength converter. Semiconductors are characterized by narrow emission lines with linewidths of the order of $2kT$. The emission spectrum linewidth of semiconductors is narrower than the linewidth of many phosphors and dyes. As for phosphors and dyes, semiconductors can have external quantum efficiencies near 100 %. The light escape problem in semiconductor converters is less severe than it is in LEDs

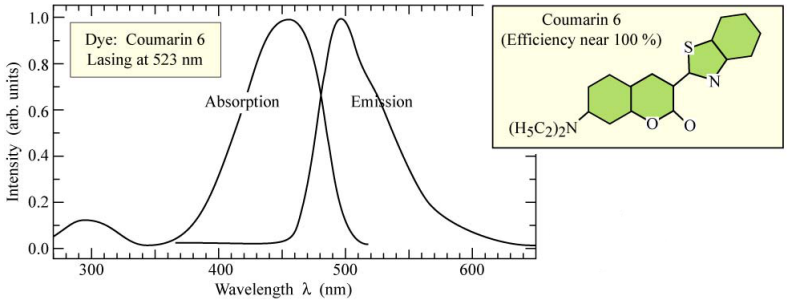

Figure 3.14: Absoorption and emission spectrum of a commercial dye

due to the fact that semiconductor converters do not need electrical contacts that could block the light. Similar to phosphors and dyes, a great variety of semiconductors is available. Using ternary or quaternary alloys, wavelength converters operating at virtually any visible wavelength can be fabricated.

3.7.3 Phosphors

Phosphors consist of an inorganic host material doped with an optically active element. Common hosts are garnets, which have the chemical formula $A_3B_5O_{12}$ where A and B are chemical elements and O is oxygen. Among the large group of garnets, yttrium aluminium garnet (YAG), $Y_3Al_5O_{12}$, is a particularly common host material. Phosphors having as host material YAG are called YAG phosphors. The optically active dopant is a rare earth element, a rare earth oxide, or another rare earth compound. Most rare earth elements are optically active. The rare earth element cerium (Ce) is the optically active element used in white light YAG phosphors.

The optical characteristics of YAG phosphors can be modified by partially substituting Gd for Y and Ga for Al so that the phosphor host has the composition $(Y_{1-x}Gd_x)_3(Al_{1-y}Ga_y)_5O_{12}$. The emission spectra for a Ce-doped $(Y_{1-x}Gd_x)_3(Al_{1-y}Ga_y)_5O_{12}$ phosphor with different compositions are shown in Fig. 3.15. The figure reveals that the addition of Gd shifts the emission spectrum to longer wavelengths whereas the addition of Ga shifts the emission spectrum to shorter wavelengths.

The chromaticity points of the YAG:Ce phosphors are shown in Fig. 3.16.

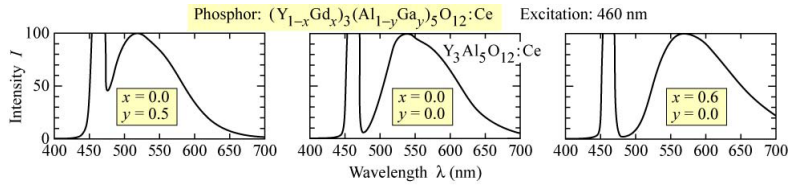

Figure 3.15: Emission spectrum of Ce-doped yttrium aluminium garnet (YAG:Ce) phosphor for different chemical compositions

The shaded region reveals the chromaticities that can be attained by mixing

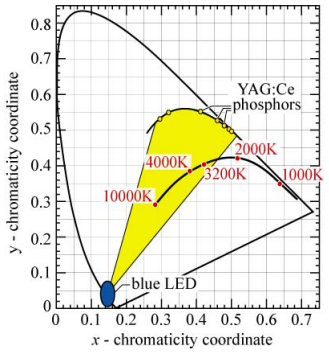

Figure 3.16: Chromaticity points of YAG:Ce phosphor and the general area accessible to white emitters consisting of a blue LED and YAG:Ce phosphor

light from a blue LED source with the light of YAG:Ce phosphors.

3.7.4 White LEDs based on phosphor converters

A white LED lamp using a phosphor wavelength converter and a blue InGaN/GaN LED was first reported in 1996 and reviewed in 1997. The InGaN/GaN LED used for optical excitation ("optical pumping") was a device reported in 1995. The phosphor used as a wavelength converter was Ce-doped YAG with chemical formula $(Y_{1-a}Gd_a)_3(Al_{1-b}Ga_b)_5O_{12}$:Ce. The exact chemical composition of the host (YAG) and the dopants (e.g. Ce) is usually proprietary and not publicly available.

The cross sectional structure of a white LED lamp is shown in Fig. 3.17. The figure shows the LED die emitting blue light and the YAG phosphor surrounding the die. The YAG phosphor can be made as a powder and

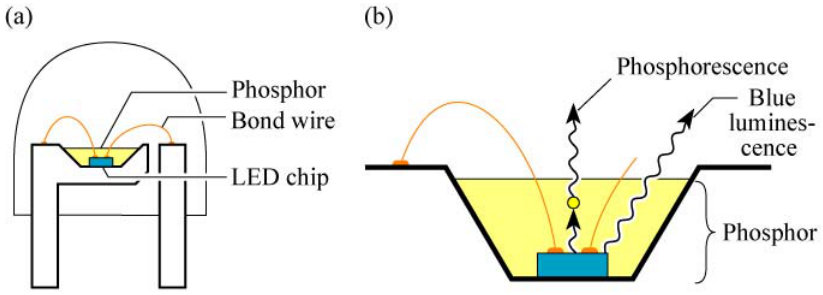

Figure 3.17: Structure of white LED lamp consisting of a InGaN blue LED chip and a phosphor

suspended in epoxy resin. During the manufacturing process, a droplet of the YAG phosphor suspended in the epoxy resin is deposited on the LED die, so that the resin fills the cup shaped depression in which the LED die is located as shown in Fig. 3.17. As indicated in the figure, of the blue light absorbed by the phosphor a fraction is re-emitted as longer wavelength light.

The emission spectrum of the phosphor-based white lamp thus consists of the blue emission band originated from the LED and of the emission band originated from the phosphor, as shown in Fig. 3.18. The thickness of the

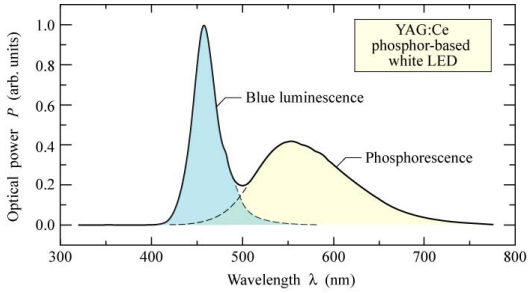

Figure 3.18: Emission spectrum of a phosphor-based white LED

phosphor containing epoxy and the concentration of the phosphor suspended in the epoxy determine the relative strengths of the two emission bands. The two bands can thus be adjusted to optimize the desired parameters.

The location of the white lamp in the chromaticity diagram is shown in Fig. 3.19. The location suggests that the emission colour is white with a bluish tint. A bluish white is indeed confirmed when looking at the lamp.

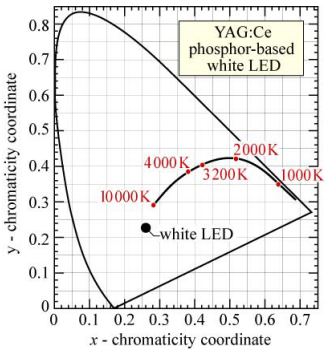

Figure 3.19: Chromaticity coordinates of a phosphor based white LED

First generation white LEDs from Nichia Corporation were improved in terms of their colour rendering capability by adding an additional phosphor that, when excited by 460 nm blue light, has a peak emission wavelength of 655 nm and a full-width at half maximum of 110 nm. As a result, the emission can be enhanced in the red range. Furthermore, by using an optimized phosphor mix, the pronounced notch in the first generation white LED is reduced. These second generation white LED lamps from Nichia Corporation render red colours better than the first generation.

Note that the downside of adding red phosphors is a reduced luminous efficiency. Thus, although colour-rendering capabilities are improved, they are improved at the expense of luminous efficiency.

Now days there are several different approaches to generate white light based on phosphors excited by semiconductor LEDs, which are shown in Fig. 3.20. They can be classified in dichromatic, trichromatic and tetra-

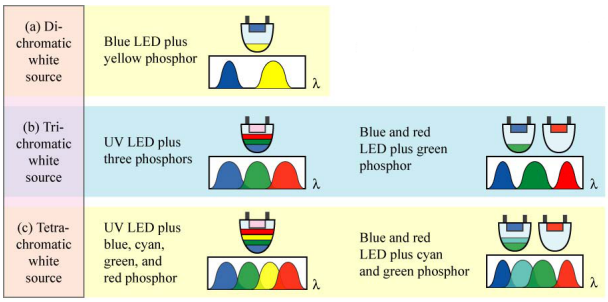

Figure 3.20: White sources using phosphors

chromatic approaches. Each of these approaches use either UV excitation

sources or visible spectrum excitation sources (mostly blue semiconductor LEDs).

Generally, the luminous efficiency of a light source decreases with increasing multi chromaticity of the source. Thus, dichromatic light sources have the highest luminous efficiency. On the other hand, the colour-rendering capability is lowest for dichromatic light sources and it increases with the multi chromaticity of the source. The colour-rendering index can reach values very close to CRI = 100 for tetrachromatic sources.

A concern with white sources is spatial colour uniformity. The chromaticity of the white light emitted by the source should not depend on the emission direction.

Spatial colour uniformity can be attained by a phosphor distribution that provides an equal optical path length in the phosphor material independent of the emission direction. Spatial uniformity can also be attained by adding mineral diffusers to the encapsulant. Such mineral diffusers are optically transparent substances, such as TiO_2, CaF_2, SiO_2, $CaCO_3$ and $BaSO_4$, with a refractive index different from the encapsulant. The diffuser will cause light to reflect, refract, and scatter, thereby randomizing the propagation direction and uniformizing the far field distribution in terms of chromaticity (i.e. spectral composition).

Chapter 4

Characterization techniques

4.1 Configuration

In this work we stressed a total of 54 LEDs, 48 LEDs have been subjected to current and thermal stress, 6 LEDs have been subjected only to thermal stress.

As far as the 48 LEDs subjected to current and thermal stress are concerned we have stressed them at three different temperature and biasing conditions. For each temperature and biasing condition we have stressed 16 LEDs and precisely

- 4 Cree XR-E blue
- 4 Cree XR-E white
- 4 Luxeon K2
- 4 Osram golden dragon plus

Fig. 4.1 shows the four different types of LEDs worked on.

We fitted these 16 LEDs in two aluminium blocks, Cree blue and Cree white LEDs in one block and Luxeon and Osram in the other block. Therefore each LED has been named through the following parameters:

- block name: CREE or LXOS ("LX" = Luxeon, "OS" = Osram)

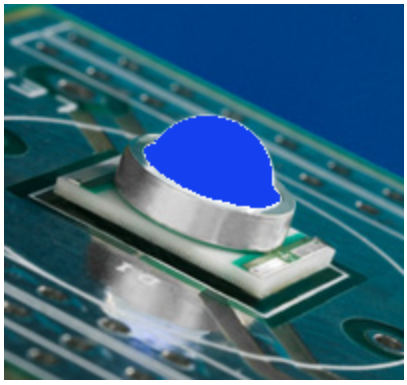

(a) *Cree XR-E blue*

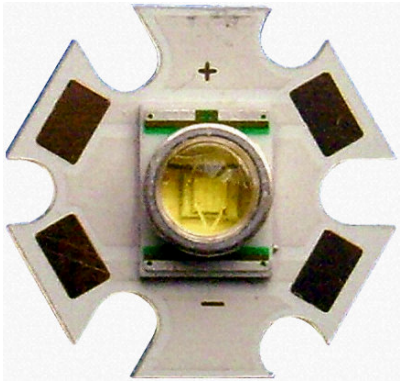

(b) *Cree XR-E white*

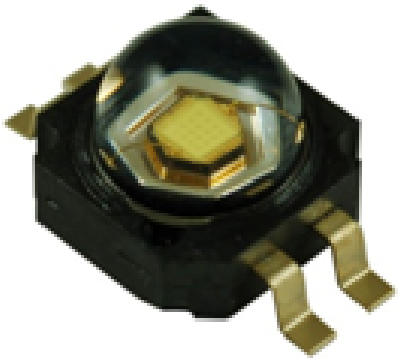

(c) *Luxeon K2*

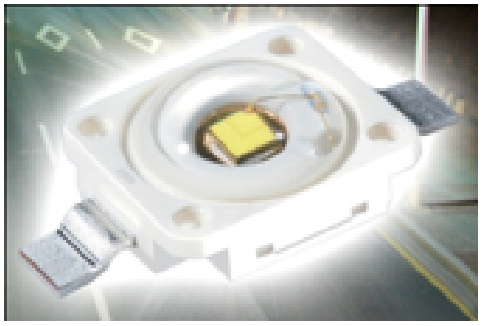

(d) *Osram Golden Dragon Plus*

Figure 4.1: The four different types of LEDs

- stress junction temperature: 120 ℃, 150 ℃, 150 ℃
- stress forward current: 1.5 A, 500 mA, 700 mA
- positional index on the block: from 0 to 7

For example: “CREE_120_1500_5” and “LXOS_150_500_0”.

In order to understand if the degradation mechanisms are caused only by temperature or by the combination of temperature and current injection pure thermal stress was carried out on other 6 LEDs.

As far as the 6 LEDs subjected to thermal stress are concerned we have stressed them at three different temperature conditions. For each temperature conditions we have stressed 2 LEDs, precisely 2 Osram golden dragon plus and we fitted these 2 LEDs in an aluminium block. Therefore each LED has been named through the following parameters:

- block name: OS
- stress temperature: 110 ℃, 130 ℃, 150 ℃
- positional index on the block: 0, 1

All these blocks consist of an aluminium base which works as a heat sink, where LEDs are glued through thermal adhesive, and of masks which fix the devices permanently and permit a repeatable positioning of the optical measurement setup.

Fig. 4.2 shows two eight aluminium blocks under stress in oven.

4.2 4-wire Kelvin configuration

The four wire Kelvin configuration is a particular connection between measurement instrumentation and device under test. In a normal measurement connection two Sense-Monitor Units (SMUs) are used to connect the instrumentation to the device, one SMU for the device anode and another one for the device cathode. Through these two SMUs both polarization and measurement are performed. The problem of this kind of measurement is that it

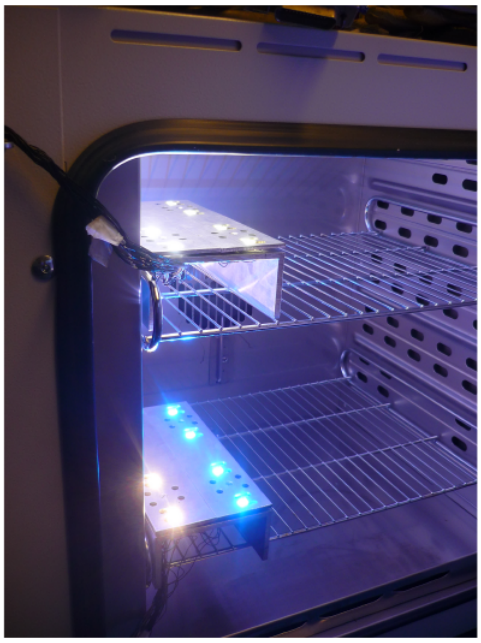

Figure 4.2: Two eight LED aluminium blocks under stress in oven

does not take into account the cables parasitic resistances. Thus, especially at high current levels, the measurement performed is not perfectly correct. In a 4-wire Kelvin configuration four SMUs are used to connect the instrumentation to the device, two for the device anode and two for the device cathode. This allows one to polarize the device with a pair of SMUs, the force SMUs, and perform the measurement with the other pair of SMUs, the sense SMUs. In this way it is possible to keep the current flowing through the sensing cables as low as possible, $I_{sense} \rightarrow 0$, thus eliminating voltage drop across the measurement cables. In Fig. 4.3 it is possible to see a simplified scheme of both 2-wire and 4-wire configurations for the measurement of a diode voltage V_d, at a bias current I_d.

It is important to note that the sense cables should be connected as close as possible to the device.

Therefore all our measurement setups require four different wires connected to each device: two for the forcing circuit (high and low) and two for the sensing circuit (high and low).

As far as the 8 LED fixtures are concerned in each fixture the wires

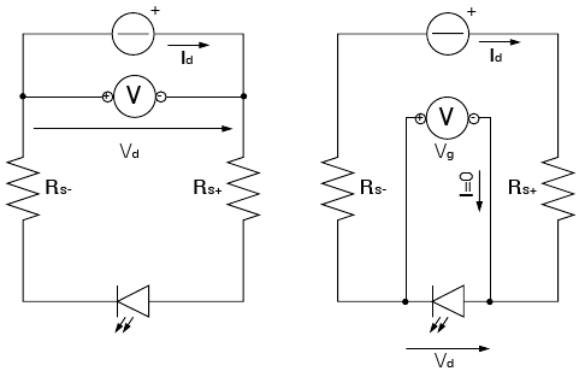

Figure 4.3: (a) 2-wire configuration and (b) 4-wire Kelvin configuration

connected to the anodes of the eight LEDs are divided in two groups. In each group every wire is connected to a different LED anode. Also the wires connected to the cathodes of the eight LEDs are divided in two groups. In each group every wire is connected to a different LED cathode. In total we have four groups of wires, each of eight wires. Each set of wires is soldered to a 15-way rectangular connector. Thus we have four 15-way connectors for each aluminium block. Through an instrument called HP 3488A switch/control unit we connect all the devices of the fixture to an instrument using the 4-wire Kelvin configuration. The switch matrix also allows us to select a specific desired LED and effectively connect this desired LED to the measurement instrumentation.

Figure 4.4: HP 3488A switch/control unit

HP 3488A swith/control unit The instrument HP 3488A switch/control unit, equipped with two 44470A 10-channel general purpose relay allowed to perform all kind of measurements with low or none human interaction, on groups of eight LEDs speeding up characterization. The great number of devices we could measure gave us the possibility to verify statistically the

coherence of results.

The switch matrix is remotely controlled through a GPIB connection and some LabVIEW Virtual Instruments. The task of the switch matrix is to internally connect the four wires of a selected device to four specific coaxial cables.

The use of the switch matrix has obvious drawbacks: an increase in the noise that affects measure and also an increase in the series resistance of the cables, thus the use of a 4-wire Kelvin connection was due.

An electrical scheme of the switch matrix can be found in Fig. 4.5

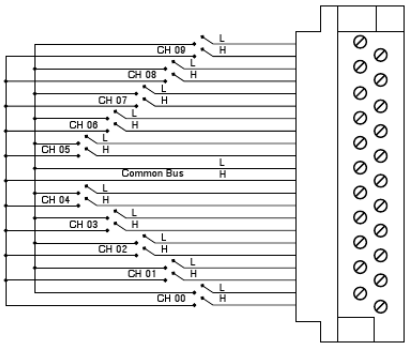

Figure 4.5: Electrical scheme of the switch/control unit

As far as the two LED fixtures are concerned all the eight wires are left dangling. We then connect manually each device to an instrument using the 4-wire Kelvin configuration.

4.3 Electrical characterization

4.3.1 Instrumentation and measurement setup

In this work the electrical characterization was performed twice, a first time using the Keithley 2612A System SourceMeter and for the eight LED fixtures also the HP 3488A switch/control unit and a second time using the HP 4155A Semiconductor Parameter Analyzer and for the eight LED fixtures also the HP 3488A switch/control unit.

I-V measurement with Keithley 2612A System SourceMeter

The Keithley 2612A System SourceMeter is a high power instrument that can drive the measured device at high current levels, up to 1 A, and high voltages, 20 V. It is capable to use the 4-wire Kelvin connection and can be controlled via GPIB. This instrument can generate pulses short as 500 μs measuring after about 100 μs since the rising edge start. Fig. 4.6 shows the front panel of this instrument.

Figure 4.6: Keithley 2612 System SourceMeter

During the electrical I-V measurement the instrument generates eight voltage pulses, all of the same duration, 500 μs, and of the same amplitude and measures the current intensity. Each of these voltage pulses is addressed by the switch matrix to a different LED. After each burst of pulses we wait three more seconds before repeating the burst with a new voltage value. This is repeated for all the voltage values at which the current flowing through the device needs to be known. Every device is turned on for 500 μs every 5 s. This should keep unaltered the LEDs junction temperature during the measurement. A sketch of the signal generated by the instrument can be found in Fig. 4.7.

Thanks to the instrument high power characteristics we can make it impose voltages from 0 to 5 V and then measure the current flowing through the LEDs up to relatively high values of forward current. In order to prevent that an excess current injection degrades the device during the measurement we set a current limit of 700 mA.

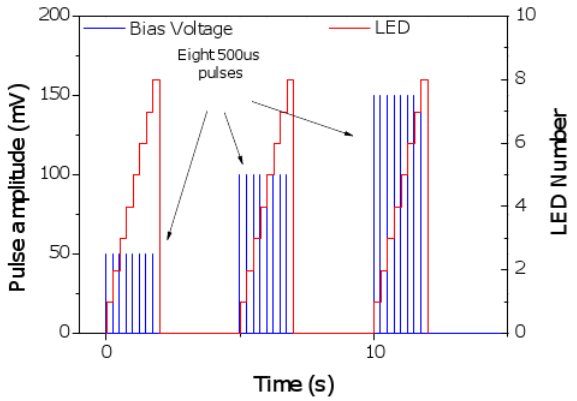

Figure 4.7: Voltage pulses generated by the Keithley 2612 during an I-V measurement

I-V measurement with HP 4155A semiconductor parameter analyzer

The HP 4155A semiconductor parameter analyzer is an instrument that allows to impose a voltage between two terminals and measure the corresponding current. It can also apply to the device a variable voltage according to a given ramp, and measure the current flowing through the device at each voltage value: in this way the I-V curves are obtained. The characteristics of the I-V curves depend on two parameters: voltage step and integration time. The choice of the voltage step has consequences on both the number of points of the I-V curves and the measurement time. A low voltage step gives I-V curves with many points, but makes measurement time longer. On the other hand a high voltage step gives I-V curves with few points, but makes measurement time shorter. Integration time determines the precision with which the measurement is performed and its duration. Integration time can be chosen among three values: short, medium and long. What changes is the number of current measurements the instrument does at each voltage value and of which the instrument makes the average to obtain each output current value.

The sensitivity of the instrument is 100 fA. This high sensitivity allows to analyze some device characteristics not visible with other instruments. How-

ever current values below the instrument's sensitivity cannot be considered significant.
Fig. 4.8 shows the front panel of this instrument.

Figure 4.8: HP 4155A semiconductor parameter analyzer

Comparison between HP 4155A and Keithley 2612A shows that the HP 4155A is more sensitive than the Keithley 2612A and can impose a reverse bias, but it does not allow the high voltages and currents that Keithley 2612A allows.

The HP 4155A has been used, controlled via GPIB, to measure the current flowing through the devices in reverse bias conditions, i.e. from -8 V to 0 V, and in forward bias conditions, i.e. from 0 V to 4 V. In this measurement we fixed a compliance of 1 mA in reverse bias and of 100 mA in forward bias. The high precision of this instrument allowed us to analyze some characteristics of the devices visible only at very low current levels. At these low current levels the noise generated by a high power instrument, such as Keithley 2612A, would have prevented us to get reliable measurements.

4.4 Optical power-current characterization

The optical power-current characterization is one of the two optical measurements that have to be performed in order to examine LEDs optical properties.

4.4.1 Theoretical aspects

Optical power characterization consists in the measure of emitted optical power versus driving current. Radiative and non-radiative recombinations are concurrent phenomena that occur in the device and whose rates depend mainly on carrier concentration. Varying the injected current and

observing the emitted optical power for each current level allows us to determine whether radiative or non-radiative recombination dominates or if carrier overflow occurs. A way to carry out the optical power versus current measurement is to inject into the device different current values, for each current value collect the emitted light with an integrating sphere and measure the optical power with a wide-band photodiode.

Let us consider the continuity equation for the injected electrons:

$$\frac{dn}{dt} = \frac{J}{ed} - An - Bn^2 \tag{4.1}$$

where J is the current density, e the unit charge, d the thickness of the active layer, A and B are the non-radiative and radiative recombination coefficients respectively.

Let us also assume steady-state conditions ($dn/dt = 0$).
At low currents, as long as $An \gg Bn^2$, we obtain for the emitted light L

$$L = Bn^2 \simeq \frac{B}{A^2}\left(\frac{J}{ed}\right)^2 \tag{4.2}$$

where we can note a quadratic dependence of L with J.
As current increases the Bn^2 term starts to dominate so that the emitted light dependence with J becomes linear.
When current reaches values that induce heating and other saturation phenomena, the emitted light dependence with J becomes sub-linear.

4.4.2 Instrumentation and measurement setup

The instruments used to perform the optical power-current characterization are Keithley 2612A, Newport 1830-C and Newport 818-UV and for the eight LED fixtures also the HP 3488A switch/control unit.

As mentioned before the Keithley 2612A System SourceMeter is a high power instrument that can drive the measured device at high current levels, up to 1 A, and at high voltages, up to 20 V. It is capable to use the 4-wire Kelvin connection and can be controlled via GPIB. This instrument can

generate pulses short as 500 μs measuring after about 100 μs since the rising edge start.

Newport 1830-C is an auto ranging digital optical power meter that can perform through a photodetector dc power measurements in 10 pW - 2 W range. Newport 1830-C is an instrument with a good measuring range and sensitivity and can be controlled via GPIB. Newport 1830-C is used together with the photodetector Newport 818-UV. This photodetector has a spectral range that covers the spectral region within 200 nm and 1100 nm. This spectral range covers all the emission spectrum of white LEDs. Figs. 4.9 and 4.10 show the Newport 1830-C and the Newport 818-UV. In Fig. 4.11 it is

Figure 4.9: Newport optical power meter 1830-C

Figure 4.10: Newport 818-UV photodetector

possible to see the spectral responsitivity and linearity of the photodetector used.

In the optical power-current characterization the Keithley 2612A is used as a DC current generator controlled via GPIB. In order to collect all the light emitted by each led the light emitted is collected by an integrating sphere connected to the photodetector.

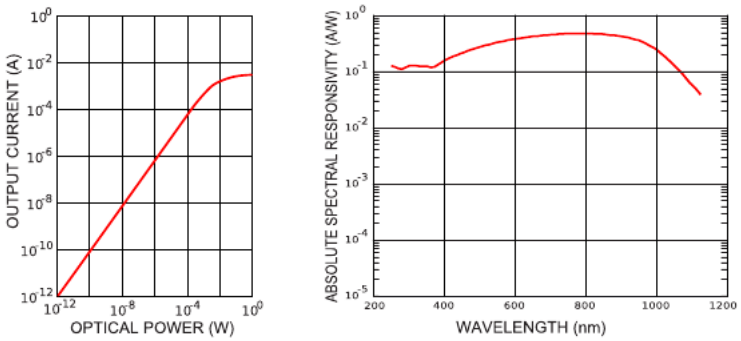

Figure 4.11: Absolute spectral responsivity and linearity of Newport 818-UV photodetector

4.5 Spectral characterization

The spectral characterization is the second optical measurement that has to be performed in order to examine LEDs optical properties.

4.5.1 Theoretical aspects

The aim of spectral characterization of LEDs is to determine the Spectral Power Distribution (SPD) of light emitted from the device. SPD is the starting point to evaluate the quality of light. Light emitted from LEDs that appears white is actually the superposition of blue and yellow light. Changes in the balance of these two colour components lead to different stimulation of human photoreceptor cells thus SPD should not vary with aging of the device.

4.5.2 Instrumentation and measurement setup

The instruments used to perform spectral measurements are Keithley 2612A, an Ocean Optics spectrometer, the USB4000, an Ocean Optics optical fibre, an Ocean Optics integrating sphere and for the eight LED fixtures also the HP 3488A switch/control unit.

As mentioned before the Keithley 2612A System SourceMeter is a high power instrument that can drive the measured device at high current levels,

up to 1 A, and high voltages, 20 V. It is capable to use the 4-wire Kelvin connection and can be controlled via GPIB. This instrument can generate pulses short as 500 μs measuring after about 100 μs since the rising edge start.

The USB4000 is a compact fibre optic spectrometer, it has a 3648-element detector, with shutter and high-speed electronics and is responsive from 200 nm to 1100 nm but the specific range and resolution depend on grating and entrance slit used. Fig. 4.12 shows the Ocean Optics USB4000 spectrometer. Fig. 4.13 shows Ocean Optics USB4000 componenets.

Figure 4.12: Ocean Optics USB4000 spectrometer

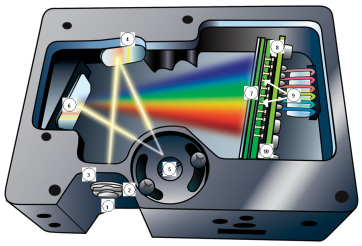

Figure 4.13: Ocean Optics USB4000 components

The main components of the USB4000 are:

- collimating mirror (4): light enters the spectrometer, passes through the SMA connector (1), slit (2), and filter (3), and then reflects off the collimating mirror onto the grating (5)
- grating (5): diffracts light from the collimating mirror and directs the diffracted light onto the focusing mirror (6)

- focusing mirror (6): receives light reflected from the grating and focuses first-order spectra onto the detector plane
- detector (8): collects the light received from the focusing mirror and converts the optical signal to a digital signal; each pixel on the detector response to the wavelength of light that strikes it, creating a digital response

In the spectral measurements the Keithley 2612A is controlled via GPIB and used to polarize the device. The light emitted by each LED is collected by the integrating sphere and sent through the optical fibre to the spectrometer.

The complete measurement system has been calibrated with a known light source to perform absolute SPD measurements.

4.6 Thermal characterization

High temperature at the junction can shorten LEDs lifetime. Junction temperature depends on both, environment temperature and driving current. In particular, electrical power dissipated by the device and optical power of the photons that cannot escape from the device result in the heating of the device. It is possible to determine the junction temperature during operation through indirect measurement by knowing the thermal resistance and the dissipated power. The thermal resistance is measured in K/W and is indicated with Rth. It can be measured in many ways, in our study we employed an electrical measurement.

4.6.1 Electrical estimation of Rth

There is a precise relation between junction temperature and diode voltage at a certain driving current. It is possible therefore to estimate the junction temperature measuring the voltage drop across the LED biased at a known current. This can be done by means of a calibration measurement which consists of a certain number of voltage measurements in response at very short current pulses applied to the device located in a temperature-controlled

oven. The small duty cycle ensures that the junction temperature is equal to the ambient temperature. This calibration measurement establishes the relation between the forward voltage and the junction temperature. Since the duty cycle of the pulsed current is very low, < 0.1 %, the heat generated by the pulsed current can be neglected and the junction temperature can, with very good accuracy, be assumed to be equal to the oven temperature. The same process is repeated for different (pulsed) current levels.

Experimental results reveal that the V_f versus T relation is very close to linear and can be fitted by the equation

$$V_f = A + BT_o \tag{4.3}$$

where T_o is the oven temperature, A and B are fitting parameters. However, this linear behaviour is no longer verified if the junction temperature varies on a wider range. In this case an exponential behaviour can be observed and Eq. 4.3 becomes

$$V_f = V_0 + Aexp - T_o/\tau \tag{4.4}$$

where T_o is the oven temperature, A, V_0 and τ are fitting parameters. In our measurements we decided to fit the data with a first order exponential decay to get a more reliable junction temperature estimation at higher temperatures. Once the calibration measurement has been carried out, a dc forward current is applied to the sample and the dc forward voltage values are measured. Using the calibration measurement, the junction temperatures for different dc currents are given by

$$T_j = \frac{V_f - A}{B} \tag{4.5}$$

for the linear case, and

$$T_j = \tau ln \frac{A}{V_f - V_0} \tag{4.6}$$

if the exponential fitting is used.

At this point the relationship among temperature, diode voltage and dissipated power are known and it is possible to evaluate the temperature of

the LED biased at a determined current. Thus a relation between dissipated power and junction temperature can be found and the thermal resistance is defined as the derivative with respect of power of $T_j(P)$

$$R_{th} = \frac{d}{dP} T_j(P) \tag{4.7}$$

Usually there is a linear relation between junction temperature and dissipated power so that the thermal resistance becomes the slope of the $T_j(P)$ line.

Chapter 5

Stress results

For LEDs worked on in this work manufactures declare a maximum junction temperature of approximately 150 °C, specifically 150 °C for Cree XR-E blue and white, 185 °C for Luxeon K2 and 135 °C for Osram golden dragon plus.

In order to study these LEDs decay mechanisms we decided to perform three different kinds of current and thermal stresses on Cree XR-E blue, Cree XR-E white, Luxeon K2 and Osram golden dragon plus. In two of these stresses we first decided the value of the injected forward current and then adjusted the oven temperature in order to make the LEDs junctions reach during stress approximately 150 °C, the maximum junction temperature declared by producers. In the third stress instead we injected a huge current and kept LEDs at room temperature.

We also performed different kinds of pure thermal stress on Osram golden dragon plus.

5.1 Cree XR-E blue

As far as the optical power decay is concerned Fig. 5.1 shows the normalized optical power decay at 700 mA for the three different stress conditions. It can be seen that all LEDs, stressed at 500 mA, 700 mA and at the huge current of 1.5 A, show very little alterations. LEDs stressed at 500 mA and at 1.5 A show a very small gain during the first 64 hours of stress, then they

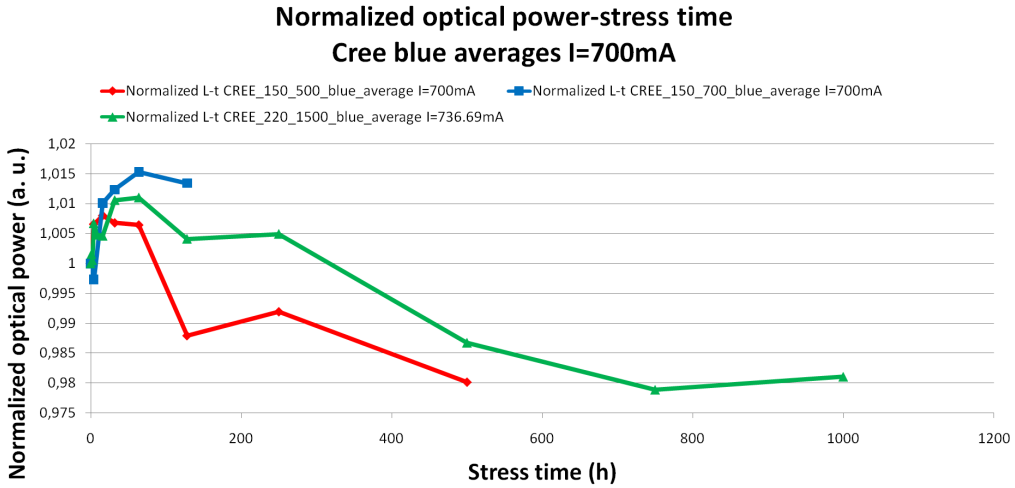

Figure 5.1: Normalized L-t Cree XR-E blue

both gradually decay, showing in fact a decay of only 2 % after 500 hours for LEDs stressed at 500 mA and after 1000 hours for LEDs stressed at 1.5 A. LEDs stressed at 700 mA show instead a little gain which after 128 hours is of about 1.4 %. Fig. 5.2 shows specifically the optical power-current curves for a LED stressed at 500 mA, for one stressed at 700 mA and for one stressed at the much higher current of 1.5 A.

As far as the electrical characteristics are concerned changes in the I-V characteristics have been minimum, as it can be seen for example in Fig. 5.3. The only significant change has been a small increase of the reverse current in some of LEDs stressed at 1.5 A. Fig. 5.4 shows the I-V characteristics of LEDs in both forward and reverse bias.

As far as the spectral measurements are concerned there have not been significant changes as stress went on, not even for LEDs stressed at 1.5 A. Fig. 5.5 shows two spectra obtained polarizing LEDs with a current equal to 700 mA, the first spectrum is of a LED stressed at 500 mA, the second one of a LED stressed at 1.5 A.

As far as the thermal measurements are concerned through transient measurements and electrical maps measurements LEDs thermal resistances have been calculated. Fig. 5.6 shows the thermal resistances found for the three different stress conditions. Through superstransient measurements and

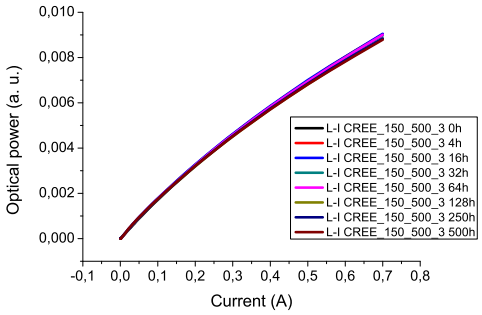

(a) *L-I Cree_150_500_3*

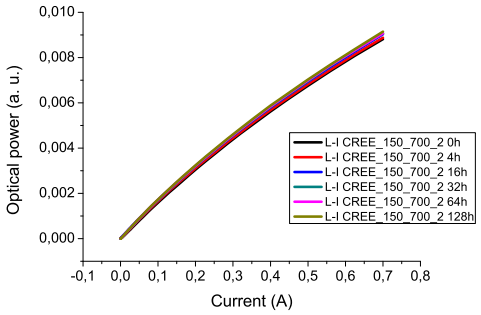

(b) *L-I Cree_150_700_2*

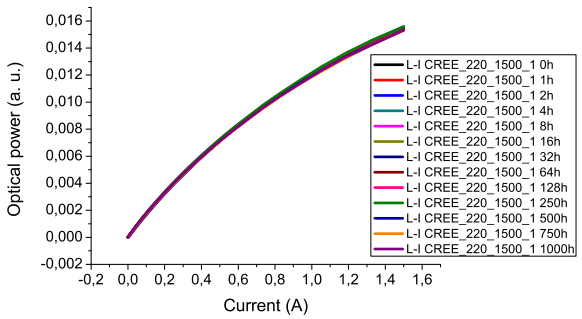

(c) *L-I Cree_220_1500_1*

Figure 5.2: L-I Cree XR-E blue

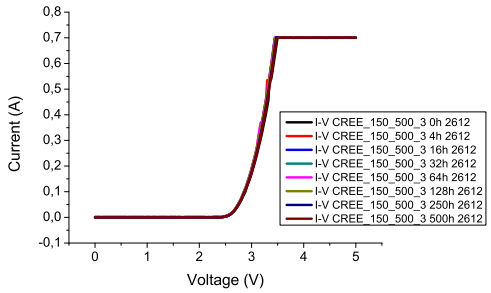

(a) *I-V Cree_150_500_3 2612*

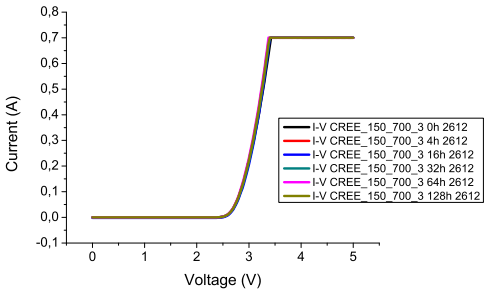

(b) *I-V Cree_150_700_3 2612*

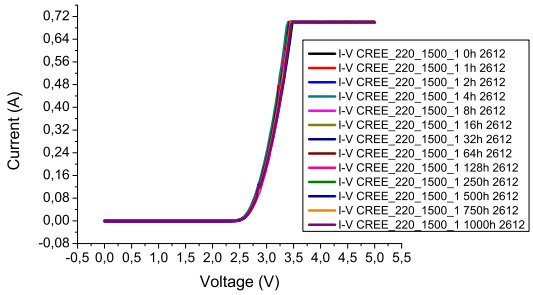

(c) *I-V Cree_220_1500_1 2612*

Figure 5.3: I-V Cree XR-E blue 2612

electrical maps measurements the temperatures at which LEDs would be submitted during stress have been calculated. Fig. 5.7 shows these temperatures for the three stress conditions.

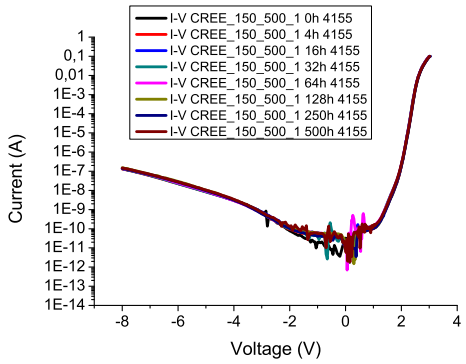

(a) *I-V Cree_150_500_1 4155*

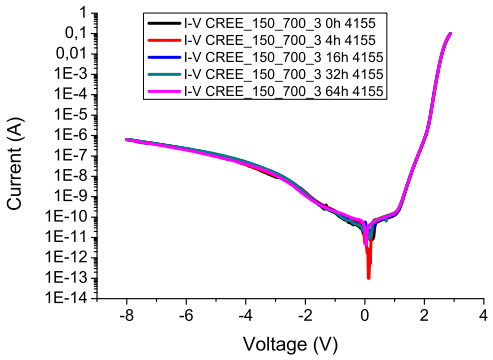

(b) *I-V Cree_150_700_3 4155*

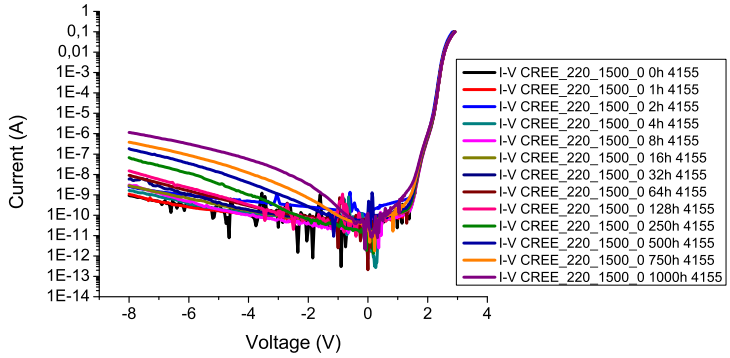

(c) *I-V Cree_220_1500_0 4155*

Figure 5.4: I-V Cree XR-E blue 4155

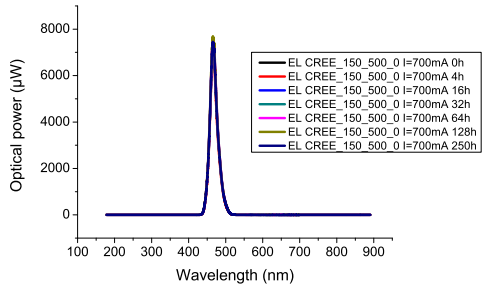

(a) *EL Cree_150_500_0*

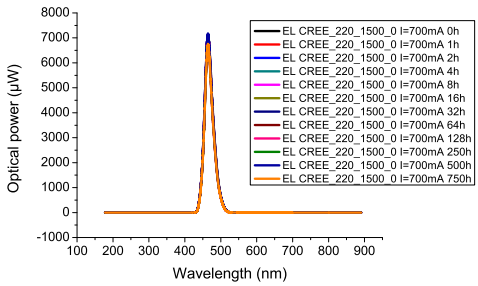

(b) *EL Cree_220_1500_0*

Figure 5.5: EL Cree XR-E blue

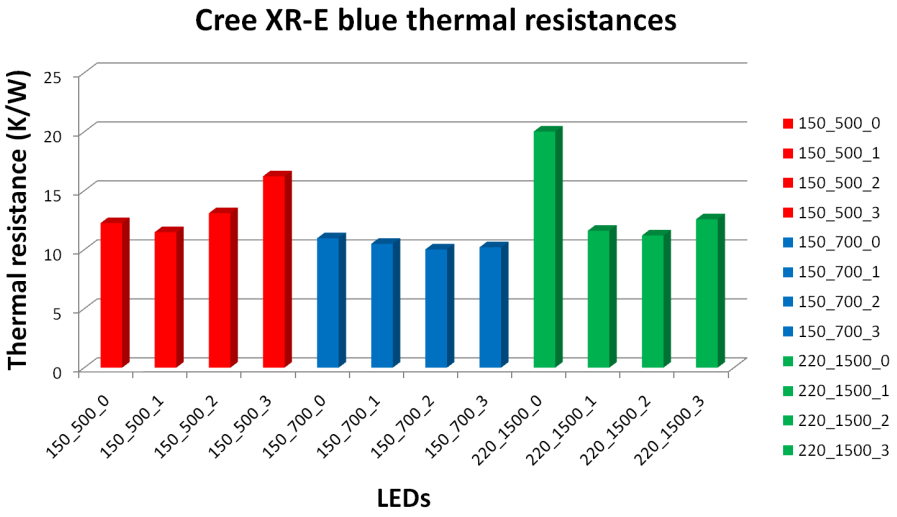

Figure 5.6: Thermal resistances

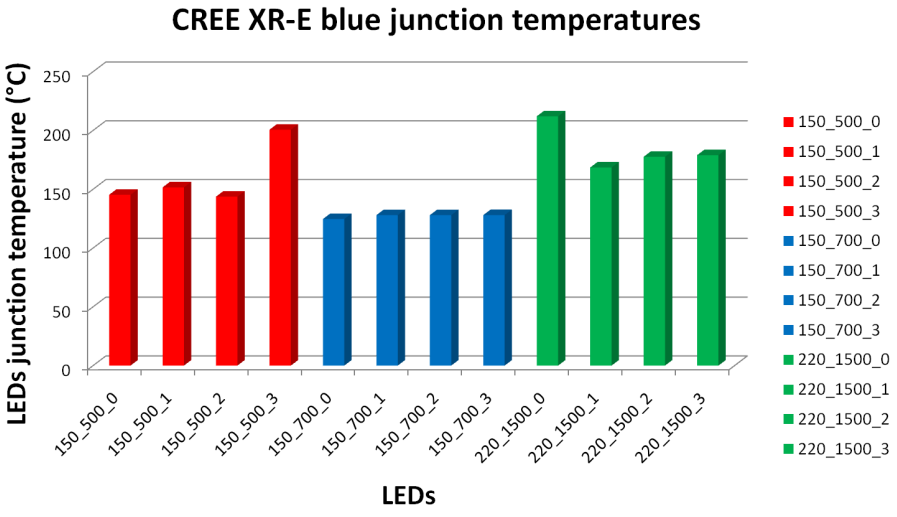

Figure 5.7: LEDs junction temperatures

5.2 Cree XR-E white

As far as the optical power decay is concerned Fig. 5.8 shows the normalized optical power decay at 700 mA for the three different stress conditions. It

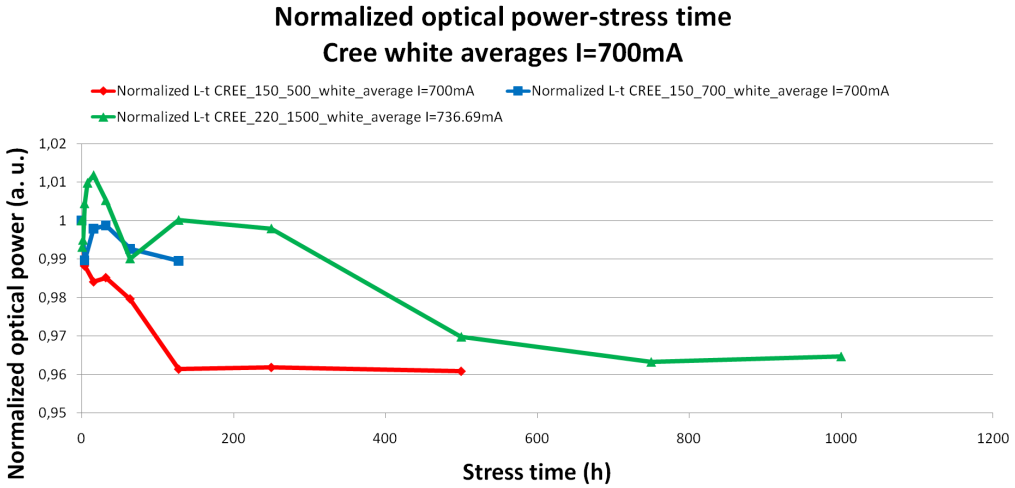

Figure 5.8: Normalized L-t Cree XR-E white

can be seen that for LEDs stressed at 500 mA there has been during the first 128 hours a decay of approximately 4 %. During the following hours instead there has been no decay, in fact at 500 hours the optical power loss is always of approximately 4 %. LEDs stressed at 700 mA did not show significant changes during the first 32 hours, then started to decay and at 128 hours this decay is of about 1 %. For LEDs stressed at 1.5 A the optical power emitted did not change significantly during the first 250 hours of stress, then started going down. At 1000 hours the optical power loss is of approximately 3.5 %. Fig. 5.9 shows the optical power-current curves for those LEDs that degraded more.

It is interesting to compare the optical behaviour of these LEDs with the correspondent behaviour of the Cree blue LEDs. The two types of LEDs have got the same chip so the differences in their degrading can be due only to the phosphors present only on the white LEDs.

As far as the electrical characteristics are concerned both LEDs stressed at 500 mA and at 700 mA do not show particular changes. Figs. 5.10 and

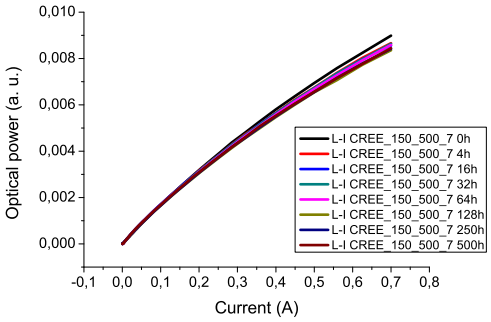

(a) *L-I Cree_ 150_ 500_ 7*

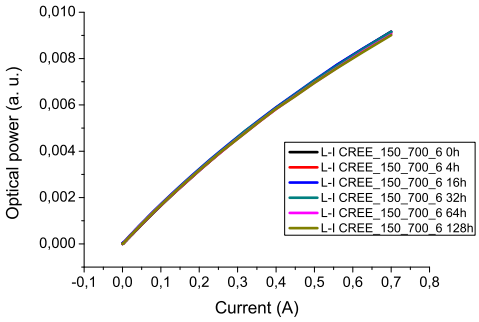

(b) *L-I Cree_ 150_ 700_ 6*

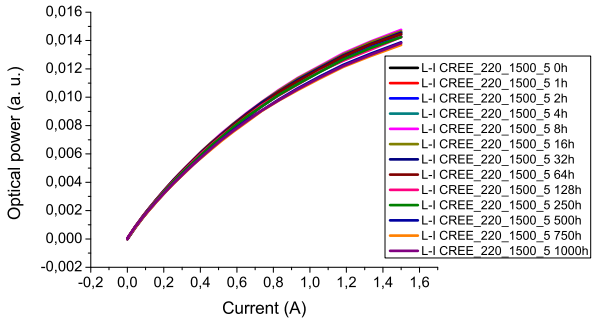

(c) *L-I Cree_ 220_ 1500_ 5*

Figure 5.9: L-I Cree XR-E white

5.11 show the I-V characteristics of some of these LEDs.

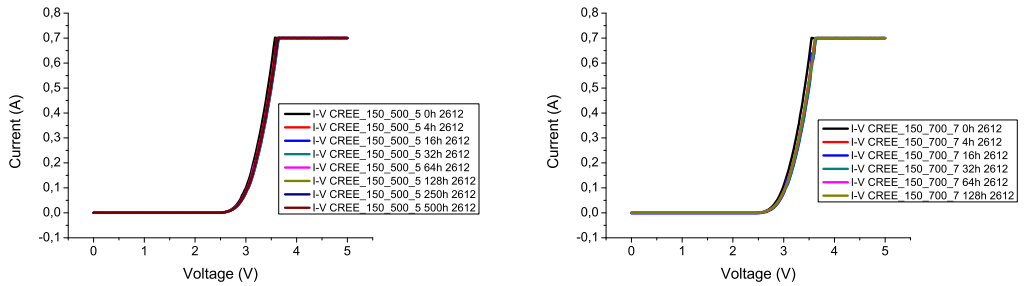

(a) *I-V Cree_150_500_5 2612* **(b)** *I-V Cree_150_700_7 2612*

Figure 5.10: I-V Cree XR-E white 2612

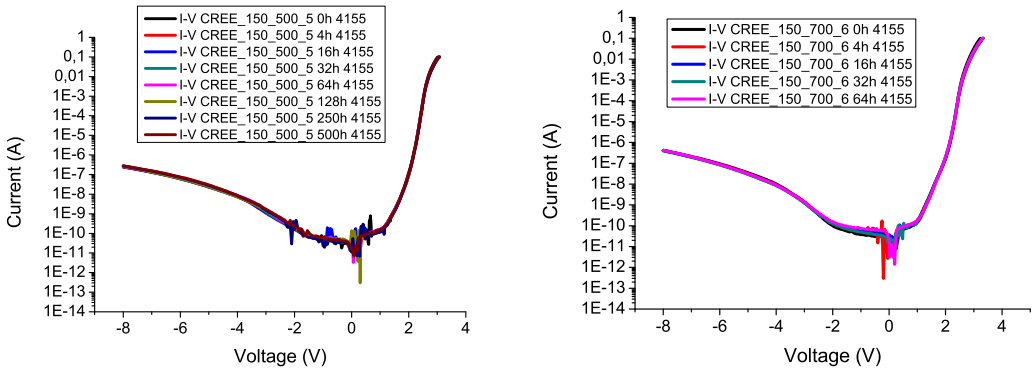

(a) *I-V Cree_150_500_5 4155* **(b)** *I-V Cree_150_700_6 4155*

Figure 5.11: I-V Cree XR-E white 4155

LEDs stressed at 1.5 A show instead a different behaviour. All these LEDs show in fact an increase in their reverse current. Fig. 5.12 shows an example of this increase. Two of these LEDs stressed at 1.5 A showed also a consistent change in their forward I-V characteristics and Fig. 5.13 shows it. Specifically we see that for these two LEDs the I-V characteristic moved consistently to the right. These are the only two LEDs that in the end broke.

As far as the spectral measurements are concerned in all LEDs the blue peak did not show significant changes, the yellow peak instead first increased during the first hours of stress, then started decreasing. This decrease is due to degradation of the phosphors. Fig. 5.14 shows two spectra obtained polarizing LEDs with a current equal to 700 mA, the first spectrum is of

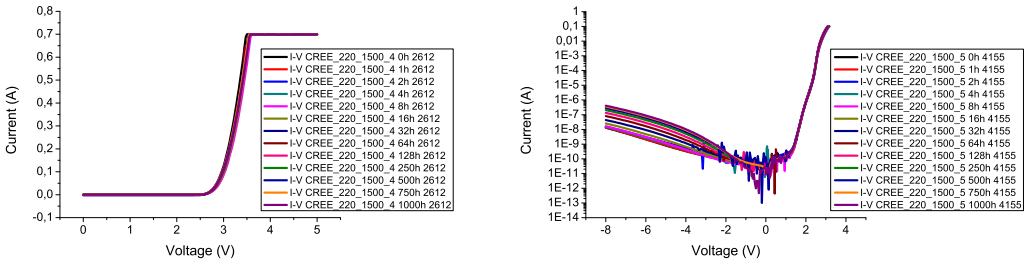

(a) *I-V Cree_220_1500_4 2612* **(b)** *I-V Cree_220_1500_5 4155*

Figure 5.12: I-V Cree XR-E white stressed at 1.5 A 2612 and 4155

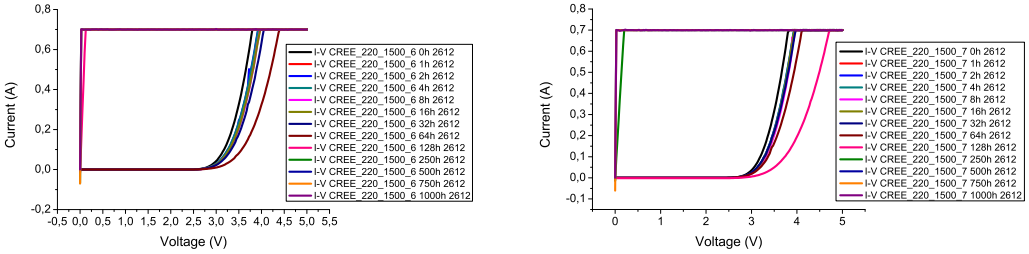

(a) *I-V Cree_220_1500_6 2612* **(b)** *I-V Cree_220_1500_7 2612*

Figure 5.13: I-V Cree XR-E white 2612 that in the end broke

a LED stressed at 500 mA, the second one of a LED stressed at 1.5 A. Fig. 5.15 also shows the normalized spectrum at 0 hours and 750 hours of

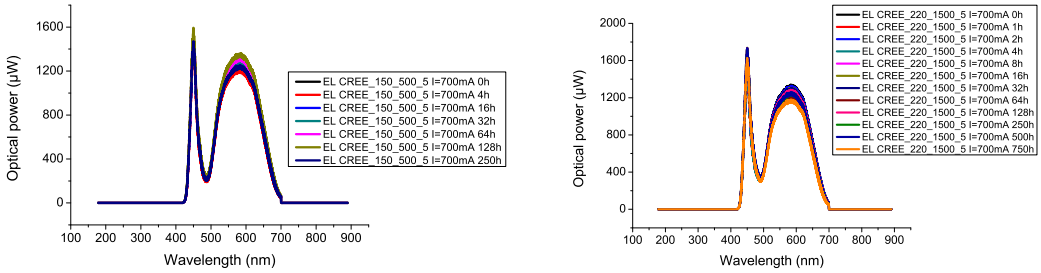

(a) *EL Cree_150_500_5* **(b)** *EL Cree_220_1500_5*

Figure 5.14: EL Cree XR-E white

a LED stressed at 1.5 A, obtained polarizing this LED with a current equal to 700 mA. Once again phosphors degradation can be observed. Phosphors degradation can also be seen in Fig.5.16. This figure is a picture of a LED taken with a microscope. It is visible in the middle of the phosphor coating a dark patch. This patch is a consequence of phosphors degradation.

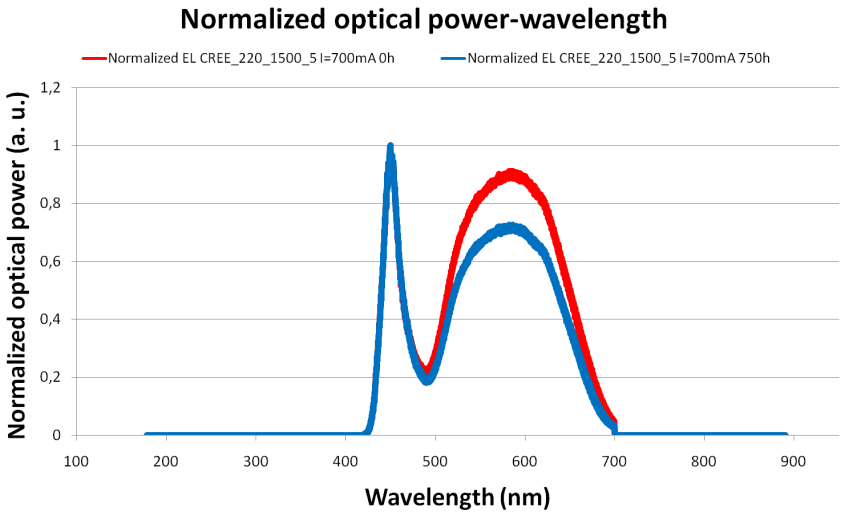

Figure 5.15: Normalized EL CREE_220_1500_5 I=700mA

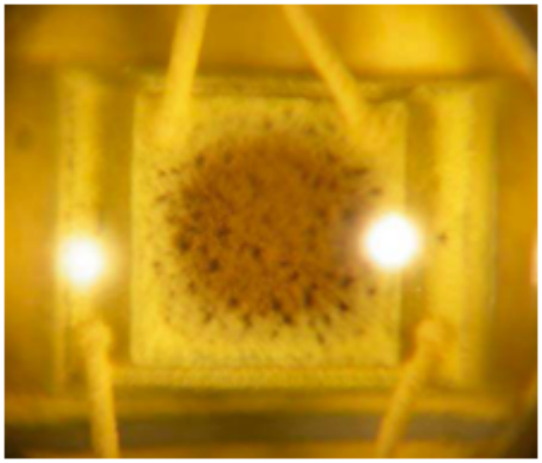

Figure 5.16: Phosphors darkening

As far as the thermal measurements are concerned through transient measurements and electrical maps measurements LEDs thermal resistances have been calculated. Fig. 5.17 shows the thermal resistances found for the three different stress conditions. Through superstransient measurements and

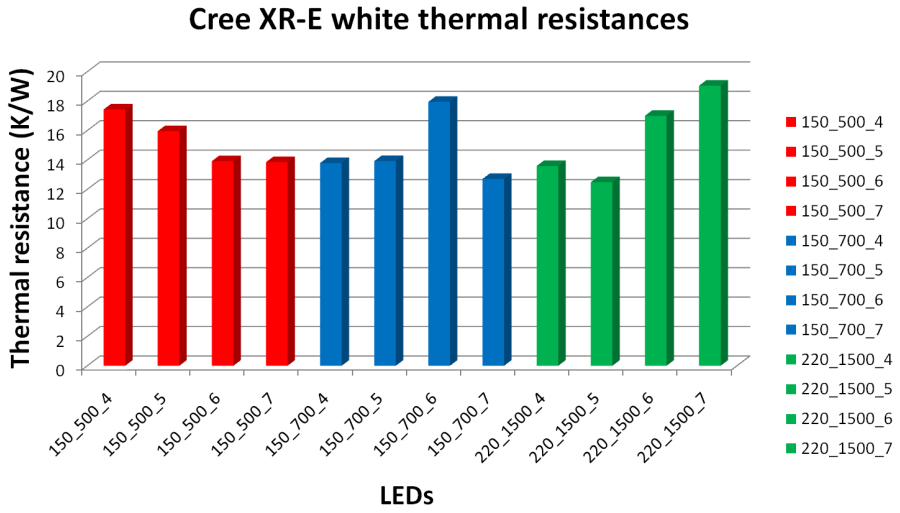

Figure 5.17: Thermal resistances

electrical maps measurements the temperatures at which LEDs would be submitted during stress have been calculated. Fig. 5.18 shows these temperatures for two different stress conditions.

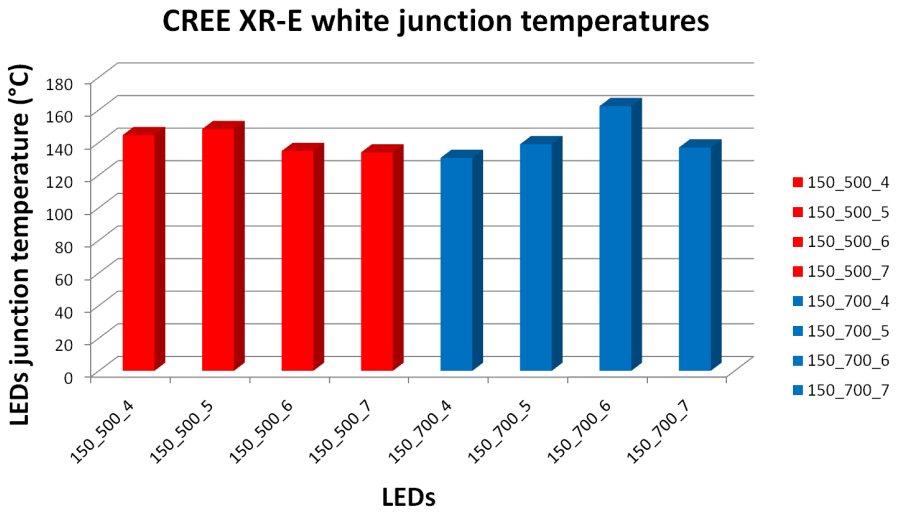

Figure 5.18: LEDs junction temperatures

5.3 Luxeon K2

As far as the optical power decay is concerned Fig. 5.19 shows the normalized optical power decay at 700 mA for the three different stress conditions. LEDs stressed at 500 mA show during the first hours of stress a gain, which reaches 2 % at 32 hours. Then from 64 hours they start degrading. At 500 hours of stress the optical power emitted is approximately 97.5 % of the optical power emitted when devices were new. LEDs stressed at 700 mA did not show either significant gains or losses up to 64 hours. Then they started to decay and at 128 hours the optical power loss is of approximately 1 %. LEDs stressed at 1.5 A show a much stronger loss in light emitted. Their optical power loss is in fact of approximately 30 % at 1000 hours of stress. Fig. 5.20 shows the optical power-current curves for some of these LEDs.

As far as the electrical characteristics are concerned the I-V curves show that all LEDs have an increase in their reverse current, and Fig. 5.21 shows an example of this increase.

As far as the spectral measurements are concerned both the blue peak and the yellow peak first increased during the first hours of stress, then started decreasing. This means that both LEDs chip and phosphors degraded.

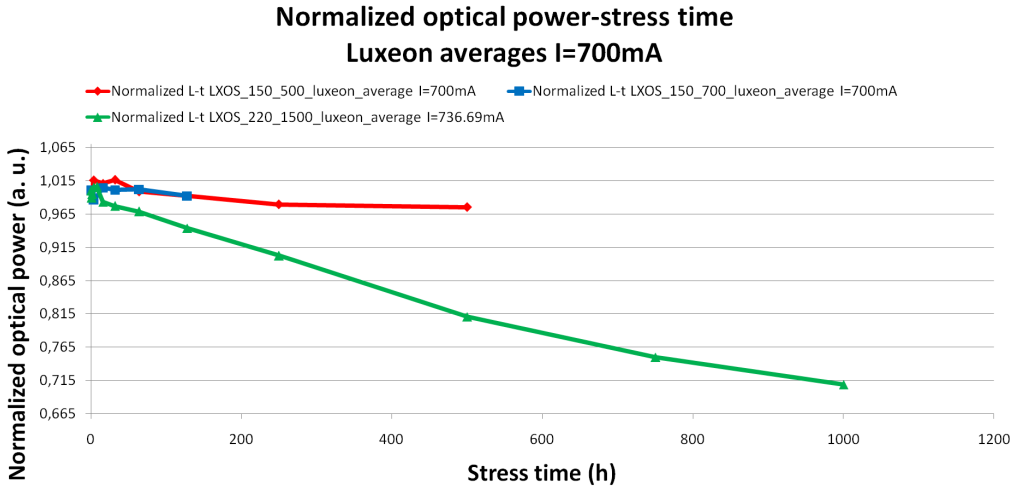

Figure 5.19: Normalized L-t Luxeon K2

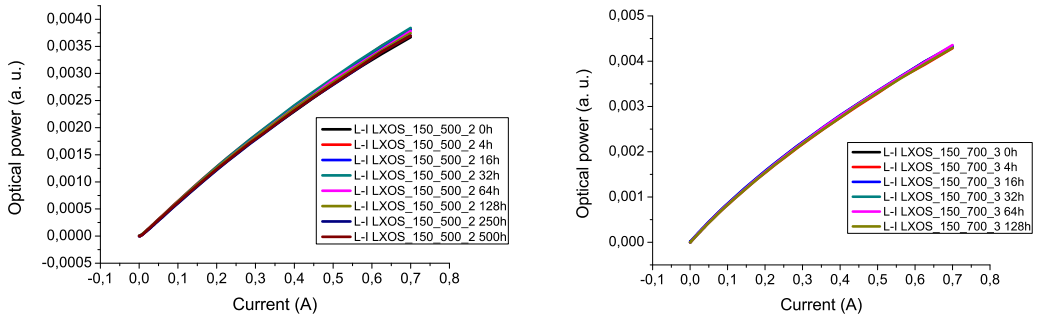

(a) *L-I Lxos_ 150_ 500_ 2* **(b)** *L-I Lxos_ 150_ 700_ 3*

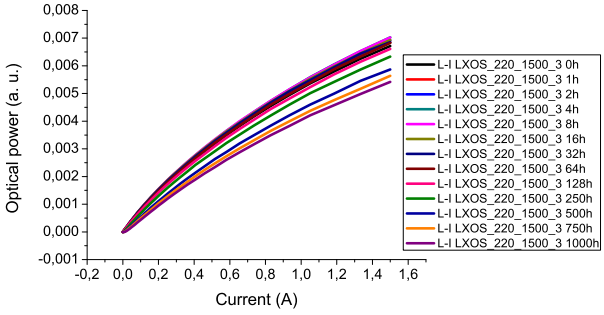

(c) *L-I Lxos_ 220_ 1500_ 3*

Figure 5.20: L-I Luxeon K2

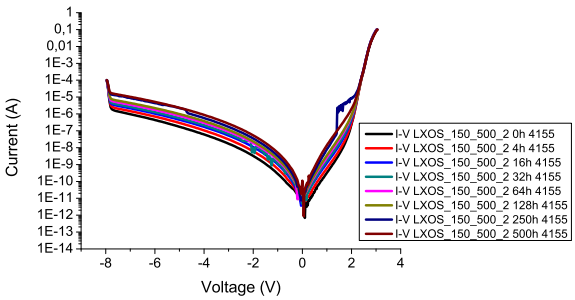

(a) *I-V Lxos_150_500_2 4155*

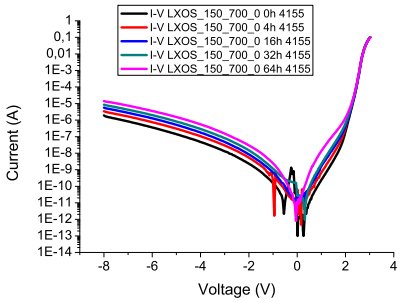

(b) *I-V Lxos_150_700_0 4155*

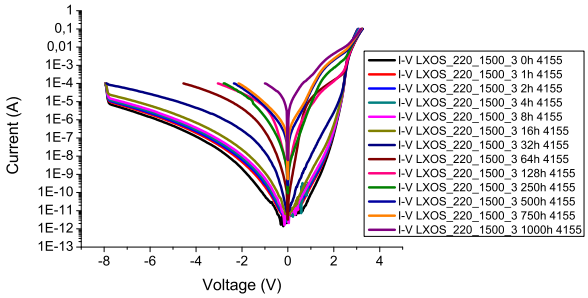

(c) *I-V Lxos_220_1500_3 4155*

Figure 5.21: I-V Luxeon K2 4155

Degradation has been bigger in LEDs stressed at 1.5 A. Fig. 5.22 shows two spectra obtained polarizing LEDs with a current equal to 700 mA, the first spectrum is of a LED stressed at 500 mA, the second one of a LED stressed at 1.5 A.

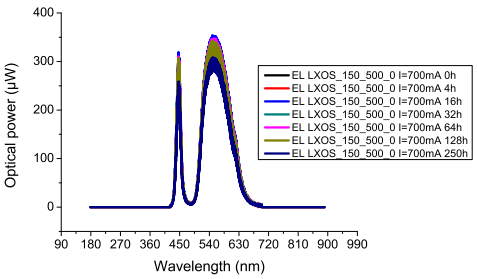

(a) *EL Lxos_150_500_0*

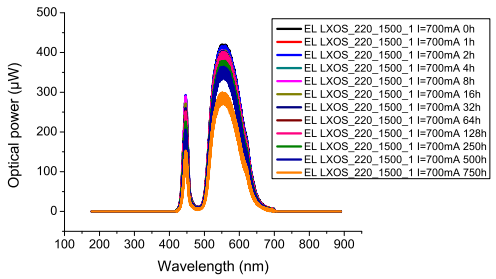

(b) *EL Lxos_220_1500_1*

Figure 5.22: EL Luxeon K2

As far as the thermal measurements are concerned through transient measurements and electrical maps measurements LEDs thermal resistances have been calculated. Fig. 5.23 shows the thermal resistances found for the

three different stress conditions. Through superstransient measurements and

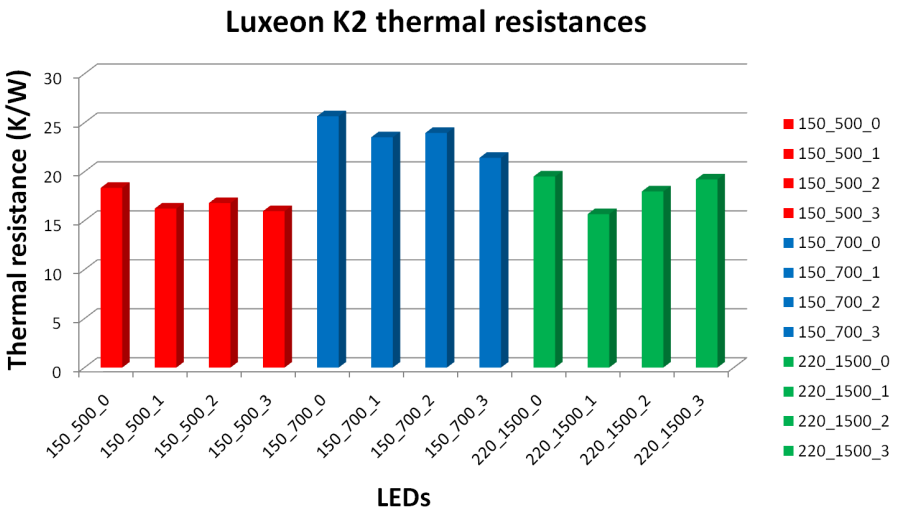

Figure 5.23: Thermal resistances

electrical maps measurements the temperatures at which LEDs would be submitted during stress have been calculated. Fig. 5.24 shows these temperatures for the three stress conditions.

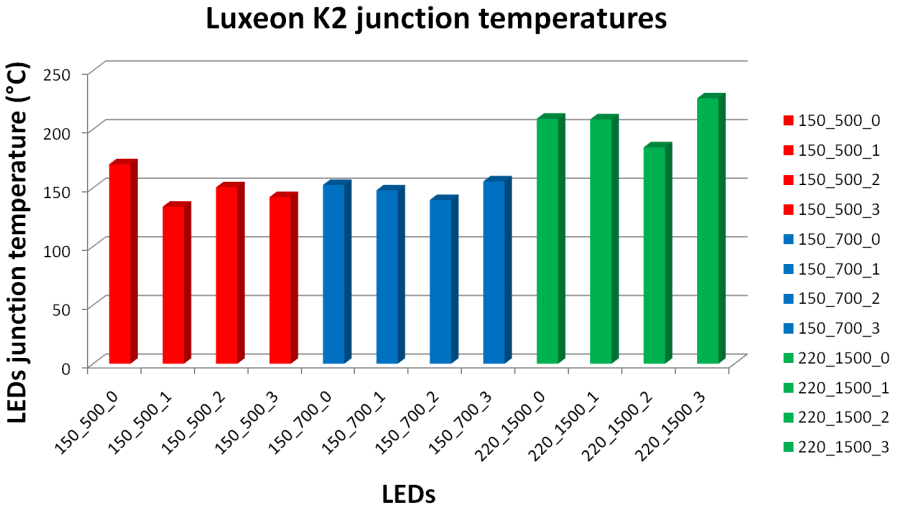

Figure 5.24: LEDs junction temperatures

5.4 Osram golden dragon plus

5.4.1 Current and thermal stress

As far as the optical power decay is concerned Fig. 5.25 shows the normalized optical power decay at 700 mA for the three different stress conditions. All

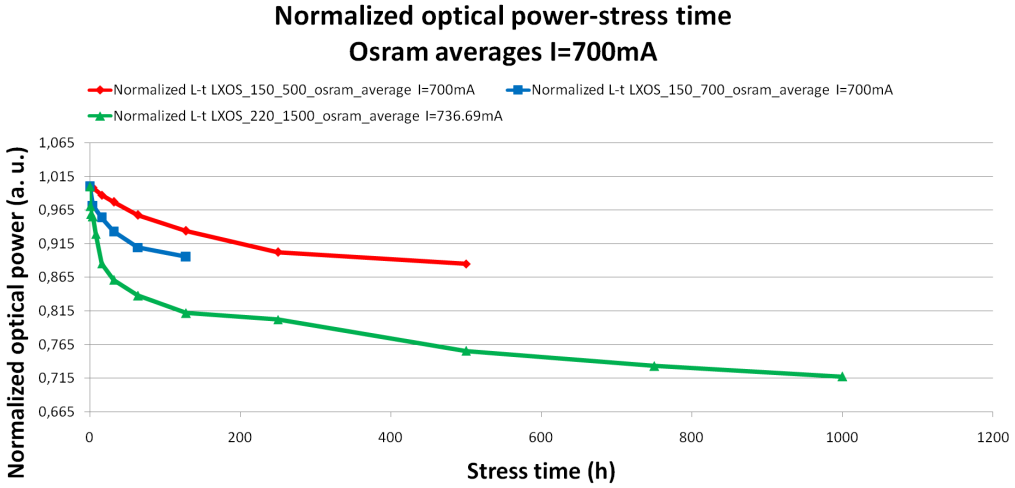

Figure 5.25: Normalized L-t Osram golden dragon plus

LEDs degrade significantly, those stressed at 500 mA after 500 hours emit an optical power which is approximately 88 % of than one emitted when new. LEDs stressed at 700 mA after 128 hours emit an optical power which is roughly 90 % of that one emitted when new. LEDs stressed at 1.5 A after 1000 hours emit an optical power which is approximately 70 % of that one emitted when new. Fig. 5.26 shows some optical power-current curves of these LEDs.

As far as the electrical characteristics are concerned the I-V curves show that all LEDs are electrically very stable. Figs. 5.27 shows the I-V curves of some of these LEDs.

Electrically the only change we can note is an increase of the current flowing through the LEDs when forward biased. Fig. 5.28 shows this increase for some LEDs.

A difference between Osram golden dragon plus LEDs and Cree XR-E

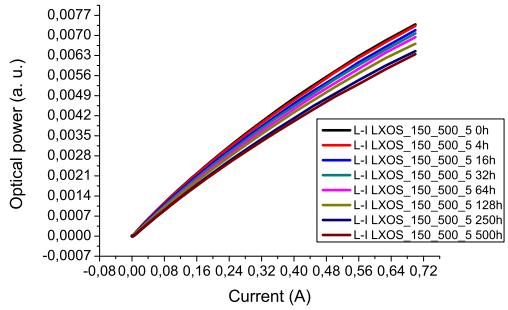

(a) *L-I Lxos_ 150_ 500_ 5*

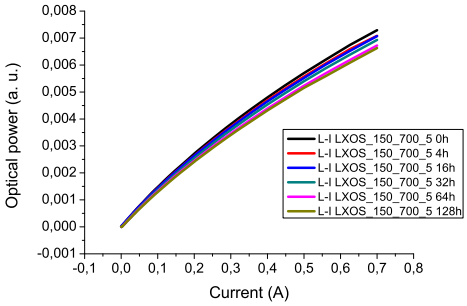

(b) *L-I Lxos_ 150_ 700_ 5*

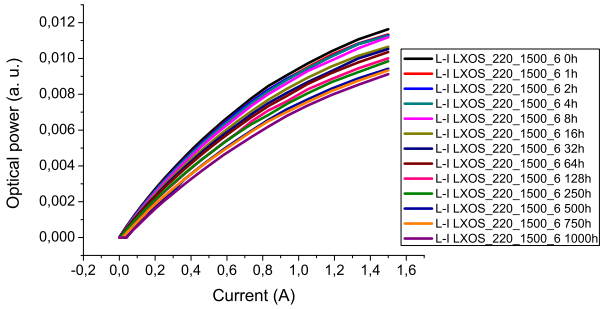

(c) *L-I Lxos_ 220_ 1500_ 6*

Figure 5.26: L-I Osram golden dragon plus

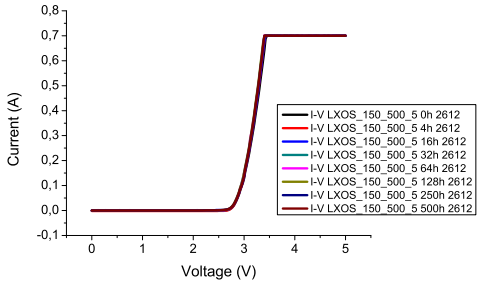

(a) *I-V Lxos_ 150_ 500_ 5 2612*

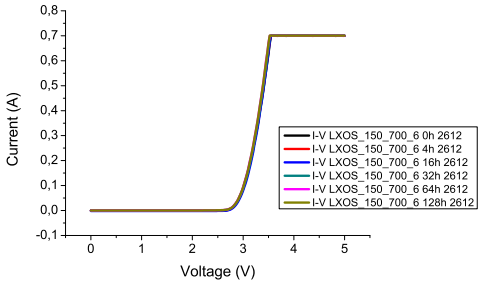

(b) *I-V Lxos_ 150_ 700_ 6 2612*

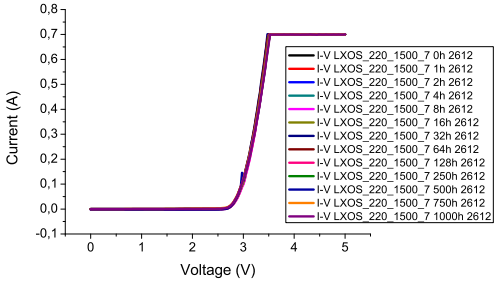

(c) *I-V Lxos_ 220_ 1500_ 7 2612*

Figure 5.27: I-V Osram golden dragon plus 2612

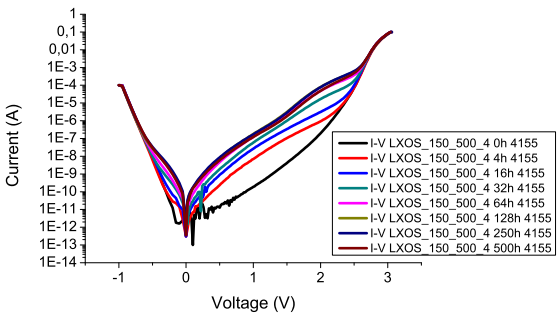

(a) *I-V Lxos_150_500_4 4155*

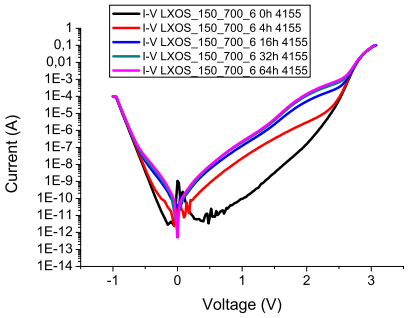

(b) *I-V Lxos_150_700_6 4155*

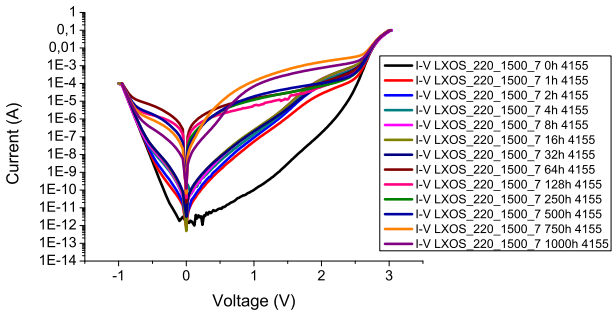

(c) *I-V Lxos_220_1500_7 4155*

Figure 5.28: I-V Osram golden dragon plus 4155

and Luxeon K2 LEDs is that Osram golden dragon plus LEDs are designed not to be reverse biased.

As far as the spectral measurements are concerned both the blue peak and the yellow peak first increased during the first hours of stress, then started decreasing. This means that both LEDs chip and phosphors degraded. Degradation has been much bigger in LEDs stressed at 1.5 A. Fig. 5.29 shows two spectra obtained polarizing LEDs with a current equal to 700 mA, the first spectrum is of a LED stressed at 500 mA, the second one of a LED stressed at 1.5 A.

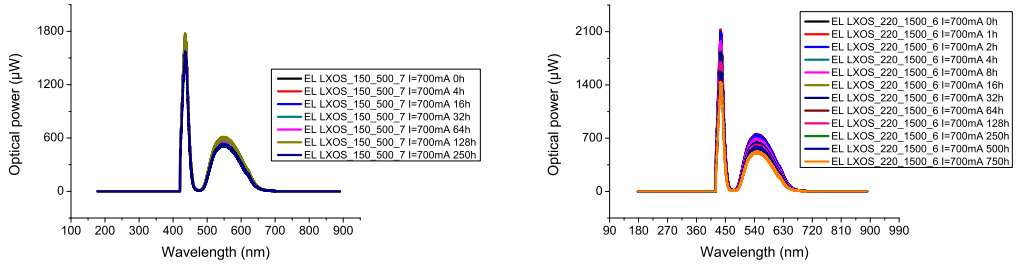

(a) *EL Lxos_150_500_7* **(b)** *EL Lxos_220_1500_6*

Figure 5.29: EL Osram golden dragon plus

As far as the thermal measurements are concerned through transient measurements and electrical maps measurements LEDs thermal resistances have been calculated. Fig. 5.30 shows the thermal resistances found for the three different stress conditions. Through superstransient measurements and electrical maps measurements the temperatures at which LEDs would be submitted during stress have been calculated. Fig. 5.31 shows these temperatures for two different stress conditions.

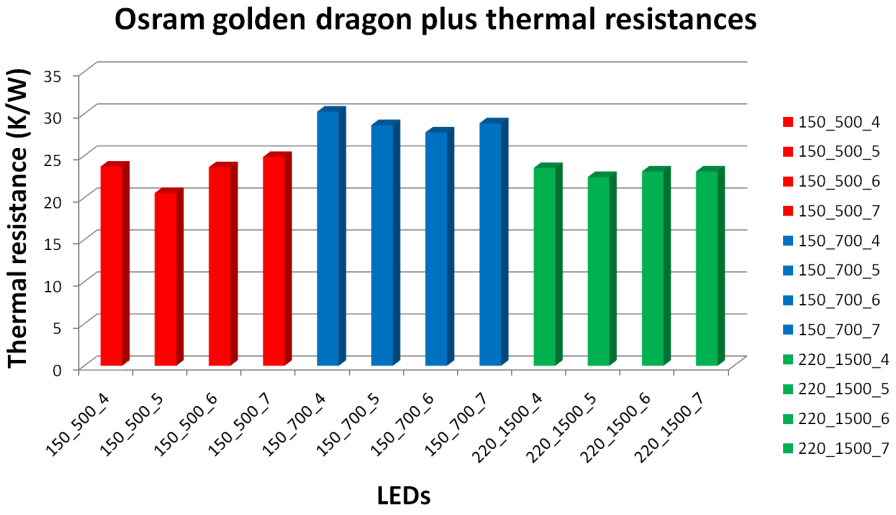

Figure 5.30: Thermal resistances

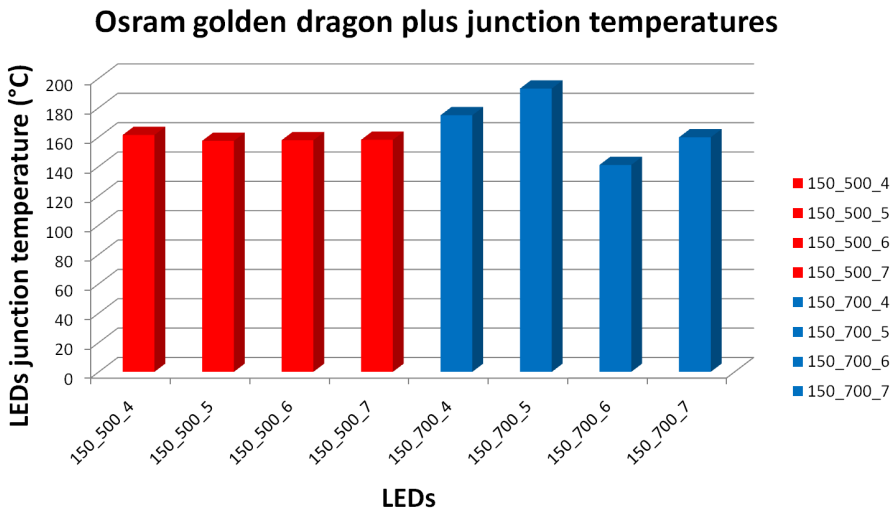

Figure 5.31: LEDs junction temperatures

5.4.2 Pure thermal stress

As far as the optical power emission is concerned Fig. 5.32 shows the normalized optical power emitted at 700 mA for the different stress conditions. It can be seen that LEDs stressed at 130 °C first gain, and at 16 hours this

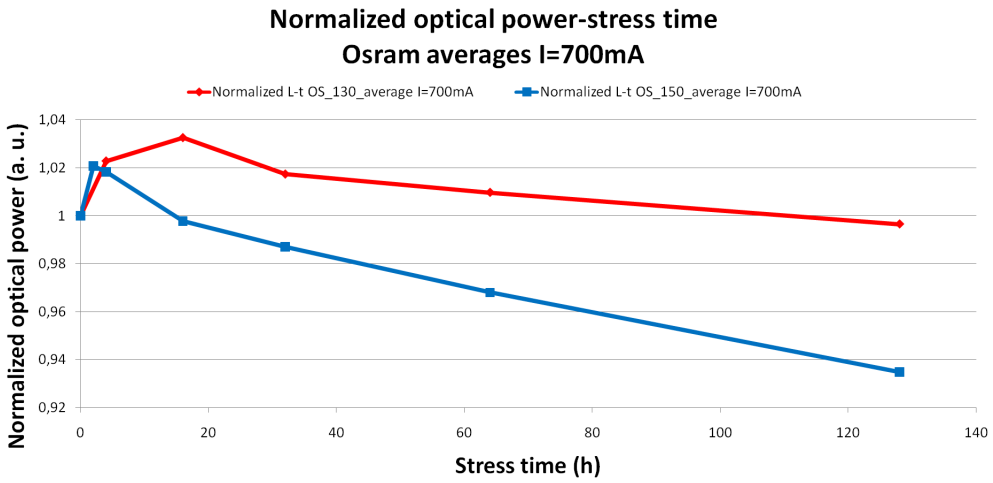

Figure 5.32: Normalized L-t Osram golden dragon plus

gain is approximately of 3 %, after decay and at 128 hours the optical power emitted is roughly 0.5 % less than when LEDs were new. LEDs stressed at 150 °C first gain, and at 4 hours this gain is approximately of 2 %, after decay and at 128 hours the optical power emitted is roughly 93.5 % of that one emitted when new. Fig. 5.33 shows the optical power-current curves for a LED stressed at 130 °C and a LED stressed at 150 °C.

As far as the electrical characteristics are concerned none of these LEDs show significant changes. Figs. 5.34 and 5.35 show the I-V caharacteristics for a LED stressed at 130 °C and for a LED stressed at 150 °C.

It can be observed in particular that there is no increase in forward current, which instead is present in the same LEDs stressed with both current and temperature.

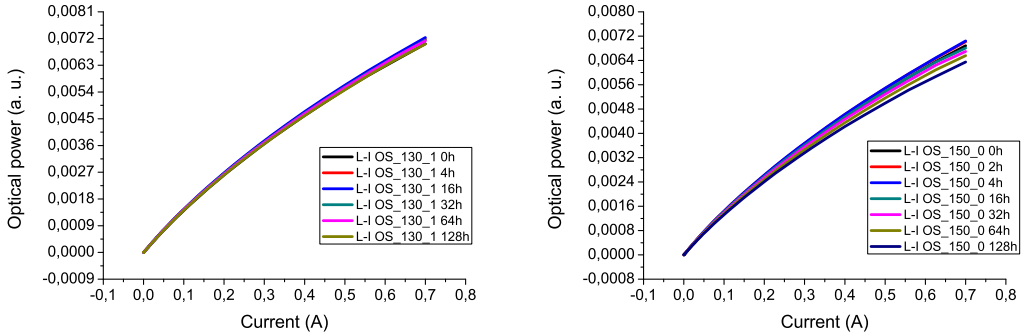

(a) *L-I Os_ 130_ 1* **(b)** *L-I Os_ 150_ 0*

Figure 5.33: L-I Osram golden dragon plus submitted to pure thermal stress

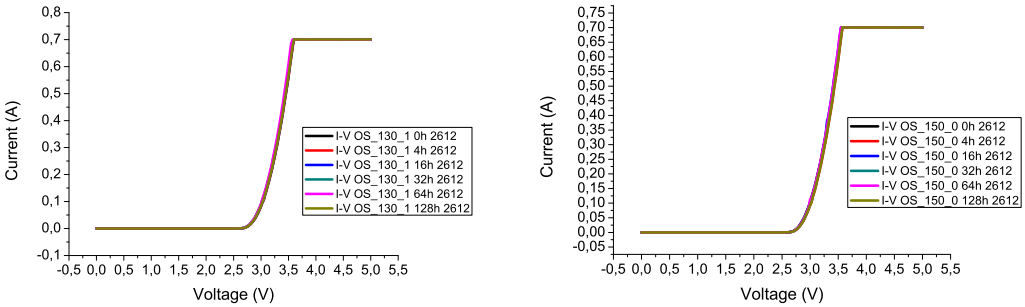

(a) *I-V Os_ 130_ 1 2612* **(b)** *I-V Os_ 150_ 0 2612*

Figure 5.34: I-V Osram golden dragon plus submitted to pure thermal stress 2612

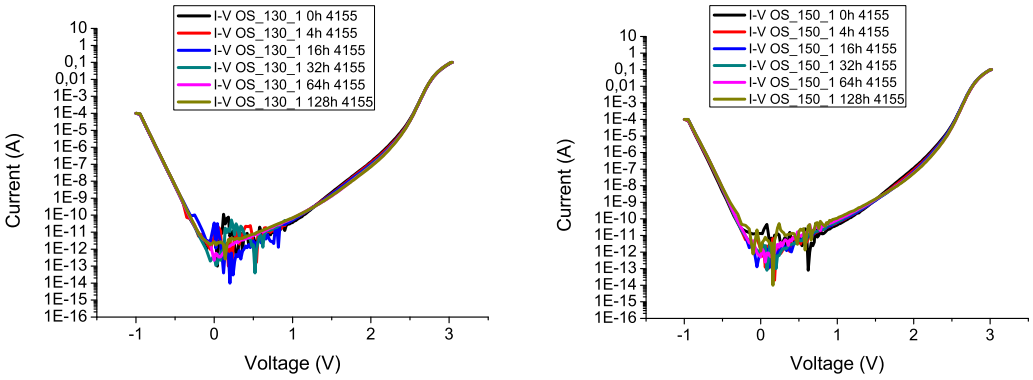

(a) *I-V Os_ 130_ 1 4155* **(b)** *I-V Os_ 150_ 1 4155*

Figure 5.35: I-V Osram golden dragon plus submitted to pure thermal stress 4155

Conclusions

In this thesis work reliability of four different types of commerical LEDs, bought from three different manufactures, have been analyzed. LEDs analyzed are considered by their producers as the future in the lighting field, i.e. the illumination sources that will substitute the actual incandescent and fluorescent lamps. This means that reliability is one of the most important factors for their success in the market.

In order to understand degradation mechanisms these LEDs have been submitted to two types of stresses, current and thermal stress and pure thermal stress, and electrical, optical and thermal measurements have been performed.

Measurements performed have shown different degradation dynamics for the different LEDs studied, both from the electrical and optical point of view.

Cree XR-E blue have demonstrated to be both electrically and optically very stable. The electrical characteristics did not change considerably even after many hundreds of hours of stress, at the same time even the optical power emitted did not go down much, for example LEDs stressed in extreme conditions (junction temperature = 220 °C and current = 1.5 A) have shown after one thousand hours of stress an emitted power decay of approximately only 2 %.

Cree XR-E white have the same chip of the Cree XR-E blue but have a phoshor coating which makes the emitted light of a white colour. Cree XR-E white have demonstrated to be both electrically and optically quite stable, but less than the Cree XR-E blue. For example LEDs stressed in extreme conditions (junction temperature = 220 °C and current = 1.5 A) have shown after one thousand hours of stress an emitted power decay of approximately

4 %. This means that the greater degrade of these white LEDs is due not to a degrade of the LED chip but to a degrade of the phoshors used to convert the blue light emitted by the chip in white light.

Luxeon K2 have demonstrated to be electrically generally quite stable, but optically to behave differently in response to the different stress conditions. When stressed at the limit conditions gave by the LEDs technical papers they showed an optical power decay of only few percents, when stressed in extreme conditions (junction temperature = 220 °C and current = 1.5 A) they showed instead an optical power decay of appoximately 30 % after one thousand hours of stress.

Osram Golden Dragon Plus have demonstrated to be electrically very stable, but optically to degrade consistently at all different stress conditions. For example LEDs subjected to extreme stress conditions (junction temperature = 220 °C and current = 1.5 A) showed an optical power decay of approximately 30 % after one thousand hours of stress, LEDs submitted to normal stress conditions showed instead an optical power decay of approximately 10 %.

However all analyzed LEDs have never showed catastrophic degrades, but only gradual degrades, even the Osram Golden Dragon Plus which are the devices that degraded more.

At the end of this work it can be stated that the analyzed LEDs show quite good reliabilities, even if some more research has to be done.

However it can be concluded that in a near future, LEDs could really substitute incandescent and fluorescent lamps and become the illumination sources of the future.

Bibliography

[1] E. Fred Schubert, *Light-Emitting Diodes*, 2nd Edition, Cambridge University Press, 2006.

[2] Richard S. Muller, Theodore I. Kamins, *Device Electronics for Integrated Circuits*, Third Edition, John Wiley & Sons, 2003.

[3] S. O. Kasap, *Optoelectronics and Photonics: Principles and Practices*, Prentice-Hall, 2001

[4] Simon M. Sze, *Semiconductor Devices: Physics and Technology*, 2nd Edition, John Wiley & Sons, 2002.

[5] Simon M. Sze, Kwok K. Ng, *Physics of Semiconductor Devices*, 3rd Edition, John Wiley & Sons, November 2006.

[6] E. Fred Schubert, *Physical Foundations of Solid-State Devices*, 2009

[7] E. Fred Schubert, *Doping in III-V Semiconductors* Cambridge University Press, 1993.

[8] S. O. Kasap, *Principles of Electronic Materials and Devices*, Third Edition, McGraw-Hill, 2006

[9] A. Zukauskas, M. S. Shur, R. Gaska, *Introduction to Solid-State Lighting*, John Wiley and Sons, 2002.

[10] L. Yang, J. Hu, M. W. Shin, *Degradation of high power LEDs at dynamic working conditions*, Solid-State Electronics 53 (2009).

[11] J. Hu, L. Yang, M. W. Shin, *Electrical, optical and thermal degradation of high power GaN/InGaN light-emitting diodes*, Journal of Physics D: Applied Physics 41 (2008).

[12] M. Meneghini, A. Tazzoli, G. Mura, G. Meneghesso, E. Zanoni, *A review on the physical mechanisms that limit the reliability of GaN-based LEDs*, IEEE Transactions on Electron Devices, Vol. 57, No. 1, January 2010.

[13] S. Ishizaki, H. Kimura, M. Sugimoto, *Lifetime estimation of high power white LEDs*, J. Light and Vis. Env. Vol. 31, No. 1, 2007.

[14] A. Laubsch, M. Sabathil, J. Baur, M. Peter, B. Hahn, *High power and high efficiency InGaN based light emitters*, IEEE Transactions on Electron Devices, 2010.

[15] M. Meneghini, L.-R. Trevisanello, G. Meneghesso, E. Zanoni, *A Review on the Reliability of GaN-based LEDs*, IEEE Transactions on Device and Materials Reliability, Vol. 8, No. 2, June 2008.

[16] Ins Lima Azevedo, M. Granger Morgan, Fritz Morgan, *The Transition to Solid-State Lighting* Proceedings of the IEEE, Vol. 97, No. 3, March 2009.

[17] Zongyuan Liu, Sheng Liu, Kai Wang, Xiaobing Luo, *Status and prospects for phosphor-based white LED packaging*, Front. Optoelectron. China 2009.

[18] Y. Xi, E. F. Schubert, *Junction-temperature measurement in GaN ultraviolet light-emitting diodes using diode forward voltage method* Applied Physics Letters, Vol. 85, No. 12, Sept. 2004.

[19] Q. Fareed, R. Gaska, J. Mickevicius, G. Tamulaitis, M. S. Shur and M. A. Khan, *Migration Enhanced Metalorganic Chemical Vapor Deposition of AlN/GaN/InN based heterostructures.*

[20] F. Rossi et al., *Influence of short-term low current dc aging on the electrical and optical properties of InGaN blue light-emitting diodes*, Journal of Applied Physics, vol. 99, pp. 3104-+, Mar. 2006.

[21] A. Y. Polyakov, N. B. Smirnov, A. V. G. J. Kim, B. Luo, R. Mehandru, F. Ren, K. P. Lee, S. J. Peartona, A. V. Osinsky and P. E. Norris, *Enhanced tunneling in GaN/InGaN multi-quantum-well heterojunction diodes after short-term injection annealing*, Journal of applied physics, vol. 91, 8, pp. 5203-5207, 2002.

[22] G. Meneghesso, S. Levada, E. Zanoni, S. Podda, G. Mura, M. Vanzi, A. Cavallini, A. Castaldini, S. Du and I. Eliashevich, *Failure Modes and Mechanisms of DC-Aged GaN LEDs*, Physica Status Solidi Applied Research, vol. 194, pp. 389-392, Dec. 2002.

[23] J. Lin, Y. Su, S. Chang, W. Lan, K. Huang, W. Chen, Y. Cheng and W. Lin, *GaN-based light-emitting diodes prepared on vicinal sapphire substrates*, IET Optoelectron., vol. 1, no. 1, pp. 22-26, 2007.

[24] A. Uddin, A. Weia and T. Andersson, *Study of degradation mechanism of blue light emitting diodes*, Thin Solid Films, vol. 483, pp. 378,381, 2005.

[25] L. Hirsch and A. S. Barri'ere, *Electrical characterization of InGaN/GaN light emitting diodes grown by molecular beam epitaxy*, Journal of Applied Physics, vol. 94, pp. 5014-5020, Oct. 2003.

[26] O. Pursiainen, N. Linder, A. Jaeger, R. Oberschmid and K. Streubel, *Identification of aging mechanisms in the optical and electrical characteristics of light-emitting diodes*, Applied Physics Letters, vol. 79, pp. 2895-+, Oct. 2001.

[27] J.-H. Yum, S.-S. Kim and Y.-E. Sung, $Y_3Al_5O_{12}:Ce_{0.05}$ *phosphor coatings on a flexible substrate for use in white light-emitting diodes*, 2004.

[28] X. Cao, P. Sandvik, S. LeBoeuf and S. Arthur, *Defect generation in In-GaN/GaN light-emitting diodes under forward and reverse electrical stresses*, Microel. Reliab., vol. 43, pp. 1987-1991, 2003.

[29] S. A. Kukushkin et al., *Substrates for epitaxy of gallium nitride: new materials and techniques*, 2007.

[30] B. Schineller et al., *Vertical-HVPE as a Production Method for Free-Standing GaN-Substrates*, 2007.

[31] Nasser N. Morgan et al., *Evaluation of GaN growth improvement techniques*, 2002.

[32] R. S. Qhalid Fareed et al., *High quality InN/GaN heterostructures grown by migration enhanced metalorganic chemical vapor deposition*, 2004.

[33] Takafumi Yao, Soon-Ku Hong, *Oxide and Nitride Semiconductors: Processing, Properties, and Applications*, Springer, 2009.

[34] H. P. Maruska, J. J. Tietjen, Appl. Phys. Lett. 15, 327 (1969).

[35] S. Nakamura, N. Iwasa, M. Senoh and T. Mukai, Jap. J. Appl. Phys. 31 1258 (1992).

[36] R. Quay, *Gallium Nitride Electronics*, Springer, 2008.

[37] S. Nakamura et al., Appl. Phys. Lett., 58 (1991). 1991 American Institute of Physics.

[38] B. A. Haskell, T. J. Baker, M. B. McLaurin, F. Wu, P. T. Fini, S. P. DenBaars, J. S. Speck, S. Nakamura, Appl. Phys. Lett. 86, 111917 (2005).

[39] B. A. Haskell, F. Wu, M. D. Craven, S. Matsuda, P. T. Fini, T. Fujii, K. Fujito, S. P. DenBaars, J. S. Speck, S. Nakamura, Appl. Phys. Lett. 83, 644 (2003).

[40] Meneghesso G., Levada S. and Zanoni E. et al., *Reliability of visible GaN LEDs in plastic package*, Microelectronics Reliability, Vol. 43, pp.1737-1742, (2003).

[41] Hwang N., Naidu P. S. R. and Trigg A., *Failure analysis of plastic packaged optocoupler light emitting diodes*, Electronics packaging technology, 5th conference, pp. 346-349, (2003).

[42] Mura G., Cassanelli, and Fantini, F. et al. *Sulfur-contamination of high power white LED*, Microelectronics Reliability, Vol. 48, pp.1208-1211, (2008).

[43] Longzao Zhou, Bing An, Yiping Wu, Shunhong Liu, *Analysis of delamination and darkening in high power LED packaging*, Physical and Failure Analysis of Integrated Circuits, pp. 656-660, 2009.

[44] S. M. Myers, S. H. Seager, A. F. Wright, and B. L. Vaandrager, *Electron-beam dissociation of the MgH complex in p-type GaN*, J. Appl. Phys., vol. 92, no. 11, pp. 66306635, (2002).

[45] M. Miyachi, T. Tanaka, Y. Kimura, and H. Ota, *The activation of Mg in GaN by annealing with minority-carrier injection*, Appl. Phys. Lett., vol. 72, no. 9, pp. 1101-1104, (1998).

[46] M. Meneghini, L. Trevisanello, C. Sanna, G. Mura, M. Vanzi, G. Meneghesso and E. Zanoni, *High temperature electro-optical degradation of InGaN/GaN HBLEDs*, Microelectronics Reliability, Volume 47, Issues 9-11, September-November 2007, Pages 1625-1629.

[47] Trevisanello L., Meneghini M., Mura G., Vanzi M., Pavesi M., Meneghesso G., Zanoni E. *Accelerated Life Test of High Brightness Light Emitting Diodes*, Device and Materials Reliability, Volume 8, Issues 2, June 2008, Pages 304-311.

Ringraziamenti

A conclusione di questo cammino è giunto il momento dei ringraziamenti.

Il ringraziamento più importante va sicuramente ai miei genitori che mi hanno sempre incoraggiato e supportato in tutto. Se adesso sono qui a scrivere i ringraziamenti per la mia tesi... il merito è soprattutto loro.

Ringrazio poi tutte le persone conosciute durante questo percorso universitario e durante il periodo di tesi.

Un sentito ringraziamento va ai miei relatori, che mi hanno consigliato e guidato durante tutto il periodo della tesi, ai dottorandi, sempre disponibli a rispondere alle mie domande, e a tutti i compagni di laboratorio, un gran gruppo di lavoro, ma anche un gran gruppo di divertimento.

Infine un ringraziamento va a tutti coloro che hanno fatto o fanno parte della mia vita, in un modo o nell'altro tutti mi hanno insegnato qualche cosa.

Grazie a tutti!

Paolo